UNIVERSITÀ DEGLI STUDI FIRENZE

European Laboratory for Non-Linear Spectroscopy

International Doctorate in Atomic and Molecular Photonics

SSD BIO/11 - XXXIII PhD cycle

Mapping of spectrally-tuned neuronal responses to visual stimuli in zebrafish – two-photon imaging and optical perturbation

Doctoral Candidate

Dr.ssa Chiara Fornetto

Supervisor: Prof. Francesco Vanzi

Coordinator: Prof. Francesco Saverio Cataliotti

External referees:

Prof. Tom Baden, School of Life Sciences, University of Sussex

Prof. Emre Yaksi, Kavli Institute for Systems Neuroscience

Years 2017/2020

Table of Contents

List of Figures

SUMMARY

Most animal species strongly depend on their sense of vision. The ability to perceive and discriminate chromatic signals is very useful for object detection and identification in the natural environment. Animals with a larval stage are generally characterized by a huge investment of energy in the rapid development of a complex retina associated with downstream visual circuits, which will improve the larva's chances of survival with sensorial cues fundamental for both predator escape and prey capture. Indeed, the environmental distribution of radiance, covering a wide range of wavelengths, may be used to construct a visual map guiding several behaviors, based on different world representations mapped with the different wavelengths. Identifying the complex networks in charge of processing visual information in the brain and deciphering their computational activity in response to specific visual stimuli, thus, represents a fundamental task in understanding sensorimotor transduction, which is at the basis of many behaviours. The transparent larva of zebrafish represents an ideal model for imaging neurons and their activity throughout the whole central nervous system (CNS) of the animal, enabling the study of the neuronal circuit correlates of behaviors. The visually-guided behavioral repertoire of larvae (e.g. optomotor and optokinetic responses, phototaxis and prey capture) becomes quite rich just after few days of development. In this context, color vision, based on a spatially anisotropic tetrachromatic retina, provides a crucial evolutionary aspect of world representation, driving some fundamental larval behaviors. Color information is integrated and processed at various levels in the retina (where specialized cells are involved in encoding spectral signals deriving from different part of the visual landscape) before conveying this information to the brain, which is the object of study of this thesis. To investigate the processing of chromatic information in the zebrafish larval brain, we mapped, with cellular resolution, spectrally-responsive neurons in the larva encephalon and spinal cord. We employed the genetically-encoded calcium indicator H2B-GCaMP6s and two-photon microscopy to image neuronal activity in zebrafish larvae at two different stages of

development (3 and 5 days post fertilization, dpf) while performing visual stimulation with spectrally-distinct stimuli at wavelengths matching the absorption peaks of the four zebrafish retina cone types. We implemented segmentation and regression analysis to identify neurons selectively responding to one or multiple stimuli and we registered them onto a reference brain for precise anatomical localization. These measurements revealed the presence of a high number of wavelength-selective neurons not only in the brain areas directly involved in processing visual information (for example the optic tectum and the other retinorecipient areas), but also in all other regions of the CNS down to the spinal cord. The zebrafish larva is a very simple model yet representative of vertebrate CNS organization, so we expect the paradigm of spectral information propagating through non-visual areas to be relevant in all vertebrates. Comparison across larvae at two different stages of development highlighted different spectral patterns of activity with responses strongly dominated by UV stimuli in 5 dpf larvae and red stimuli in 3 dpf larvae. The latter showed a negligible level of integration between multiple stimuli and no wavelength-selective neurons in the spinal cord. The spectral tuning of responses and anatomical maps of neurons involved in color-driven behaviors indicate the complexity of the circuits involved and open the way to their detailed investigation. Perturbative optical approaches, based on laser ablation and optogenetics techniques, allow dissecting neuronal circuits underlying visually-evoked responses. As part of this work, I setup novel methods for GCaMP-based temporary and selective perturbation of neurons and for optical highlighting of their intricate neurite structure. These methods were tested with the inactivation of tectal neurons responding to specific spectral stimuli, followed by a mapping of their projections into the tectal neuropil. This approach, in combination with the pan-neuronal expression of the genetically-encoded Ca^{2+} indicator GCaMP6s, allowed us to induce a temporary loss of function to the visual stimuli specifically localized to the irradiated cell, without affecting the surrounding neurons. Therefore, the method developed in this thesis can be applied to the study of local connectivity and networks in the CNS.

Understanding the workings of the vertebrate brain is one of the main challenges of modern science. In this context, the development of novel approaches at the interface between physics and biology drives constant improvements in our capability of studying neuronal activity at large scale and dissecting connectivity patterns to form complex and dynamic networks. The goal of measuring neuronal activity in real time and in an entire vertebrate brain represents a formidable task and finds in the transparent zebrafish larva the best model for implementing many innovative technologies. In this thesis, two-photon microscopy allowed to investigate the distribution of spectral information across the whole brain and spinal cord, providing novel insights in this field and laying the ground for future investigations based on perturbative approaches.

1. INTRODUCTION

1.1 Zebrafish: a model system for circuit neuroscience

The brain is an extremely complex system, not only for the number and different types of neurons that constitute it, but especially for their connections to form dynamic networks through synapses. Understanding the mechanisms of information processing in the brain (and their alterations in neurological disorders) requires mapping the neuronal circuits activated in response to different stimuli. This is a daunting task, since it requires imaging large volumes with enough spatial and temporal resolution to map cellular networks and their activity often spanning the whole brain. A technique commonly used to identify the populations of neurons involved in a specific task is functional Magnetic Resonance Imaging (fMRI). However, the low spatial (1 mm) and temporal (1 s) resolution of this technique does not allow mapping circuitries at the cellular level, so that, in order to monitor neuronal activity (with ms dynamics) at single cell resolution (in the micrometric range), other techniques are needed. Among these, optical techniques are prevalent due to their numerous advantages. In particular, confocal, light-sheet and two-photon microscopy, in combination with Genetically Encoded Calcium Indicators, allow monitoring neuronal activity at the single cell level (see paragraphs 1.6.3). Even in this case, however, fully mapping circuits in the whole brain of an animal is often hindered by the opacity of the tissue. For this reason, in recent years, zebrafish has become an important model in neuroscience (as well as in other fields of biological research). The transparent larva of zebrafish represents an ideal model for imaging neurons and their activity throughout the whole central nervous system (CNS), enabling the study of the neuronal circuit correlates of behaviors. Zebrafish (*Danio rerio*) is a small freshwater teleost fish native of South-Est Asia belonging to the cyprinid family (Figure 1). Given its small size, rapid development (precursors of the internal organs appear by 36 hours post fertilization, hpf), and the short generation time (generally 3-4 months), it is easy to

manipulate and to raise in the laboratory. Moreover, the optical transparency of embryos and larvae, and the small size of the brain (~300 µm thick, 400 µm wide and 800 µm long) which maintains the basic vertebrate brain organization (although at a lower-level complexity), make the entire larval nervous system optically accessible, allowing brain-wide monitoring of neuronal activity [1-6]. The relatively simple larval CNS, constituted by about 100000 neurons at 4 days post fertilization (dpf) [7] is yet capable of a wide array of visually-guided behaviors (i.e. optomotor and optokinetic response, phototaxis and prey capture; [8-11]). Together, these characteristics made zebrafish larvae prominent models for the study of the neuronal basis underlying these behaviors both at synaptic, cellular and circuit levels. The dependence of larvae on vision is associated to a rapid development of their visual system and to the presence of a spatially and functionally anisotropic retina characterized by four spectrally-distinct cone types allowing these organisms to perceive and discriminate chromatic signals ranging from UV to red. Zebrafish retinal circuits, in fact, are specialized in processing chromatic signals (among other features) in relation to their behavioral requirements based on the asymmetric distribution of the spectral content in their natural visual environment. As a consequence, light of different wavelengths and its fluctuations in their natural habitat affect some fundamental larval behaviors (for example prey capture) resulting in an integration of visual inputs from the retina to the brain regions specialized in encoding associated motor events. Thus, the complex interplay between light, neuronal networks and behaviors can be "easily" investigated in these organisms, whose characteristics allow to overcome all limitations that emerge working on other vertebrates (i.e. tissue opacity and large size and complexity of the brain). This has enabled employing advanced calcium imaging techniques, electrophysiological recordings and optogenetics measurements to record neuronal activity *in vivo*, in the whole brain and at single-cell resolution, during visual stimulation or while tracking visually-evoked behaviors.

Figure 1. Adult zebrafish (long-fin variety).

1.2 Zebrafish visual system: structure and function

Zebrafish retina is a specialized part of the CNS capable of detecting and processing visual inputs from the outside world to then convey them to the brain. It is a multilayered structure, similar to that of the other vertebrates [12], characterized by five highly specialized neuron types (photoreceptors, horizontal, bipolar, amacrine and ganglion cells) and one glial type (Müller glia cells) arranged into three nuclear and two synaptic (or plexiform) layers. In the outer nuclear layer (ONL) cones and rods photoreceptors (PRs) are located, whose axons release glutamate as neurotransmitter and form synaptic contacts with horizontal and bipolar cell dendrites in the outer plexiform layer (OPL). Horizontal cells (HCs) are second-order inhibitory cells and contact PRs and bipolar cells (BCs) laterally, thus providing them with inhibitory feedback and feedforward signals. The inner nuclear layer (INL) contains the somata of BCs, HCs and amacrine cells (ACs) and also the cell bodies of the glia cells. The synaptic terminals of BCs, in turn, contact retinal ganglion cell (RGC) dendrites and AC terminals in correspondence of the inner plexiform layer (IPL). ACs connect horizontally and, at the same time, also across the IPL to provide inhibitory feedback and feedforward signals to BC and RGC terminals. RGC bodies and displaced amacrine cells (dACs) are located in the ganglion cell layer (GCL). The ganglion cell axons form the optic nerve

through which the synaptic inputs, integrated across their dendrites, are sent to the brain (Figure 2) [13-15]. Eye morphogenesis in zebrafish begins at 12 hpf and subsequent structural changes appear at 24 hpf when also the retina stratification from the inner to the outer layer starts developing. At 32 hpf GCs and ACs development begins, while formation of PRs starts at 50 hpf. The last cell type to form are BCs at 60 hpf and the complete retina stratification with the different retinal cell types and synaptic contacts appear functional at 60-70 hpf [16-19]. At around 70-74 hpf the first connections between retina and optic tectum start appearing and tectal neurons begin to display mature responses at around 78 hpf. In the vertebrate retina, included zebrafish, sensory inputs follow a vertical pathway starting from PRs to BCs and finally to RGCs which, in turn, relay visual information to the brain. In the zebrafish larva, this vertical pathway becomes functional at 70-74 hpf and it is necessary in establishing contacts with the optic tectum [17]. All these three cell types use glutamate as neurotransmitter. However, this vertical flow of information can be modified through lateral inhibition induced by HCs in the distal retina and by ACs in the proximal retina [20, 21].

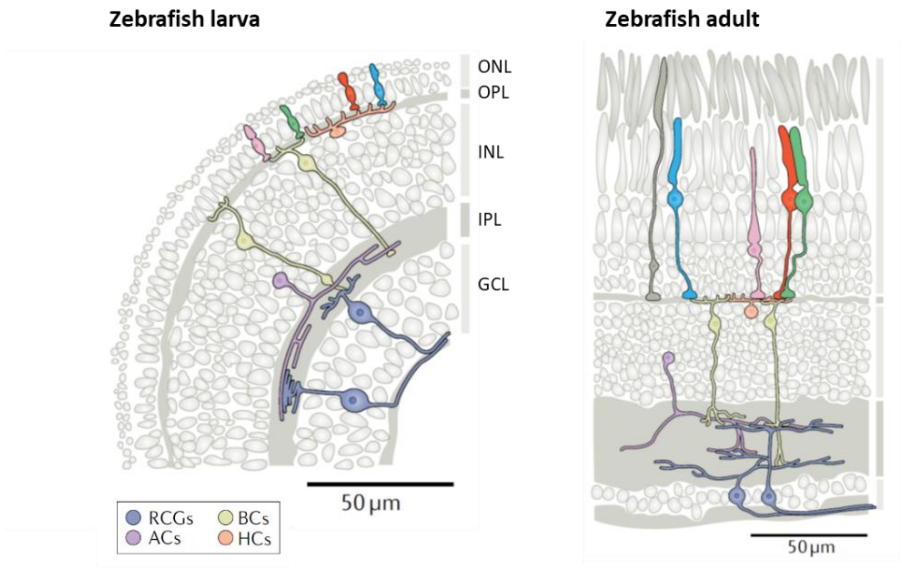

Figure 2. Retina organization and composition in larval and adult zebrafish.

The figure shows the five characteristic layers (demarcated alongside the image) of the retina highlighting the different cell types (see legend) and connections. Abbreviations: ONL, outer nuclear layer; OPL, outer plexiform layer; INL, inner nuclear layer; IPL, inner plexiform layer; GCL, ganglion cell layer; RGCs, retinal ganglion cells; ACs, amacrine cells; BCs, bipolar cells; HCs, horizontal cells; Photoreceptors (cones and rods) are highlighted in its individual colors in correspondence of the ONL. Note that in the zebrafish larva retina there are no functional rods. (Figure modified from Baden et al., 2020).

1.2.1 Retina cell types

PRs. Zebrafish retina is characterized by one rod photoreceptor type and four morphologically and spectrally distinct cone types both in larvae and in adults, with differences in their spatial organization [18, 22-24]. Given the presence of a tetrachromatic retina with cone pigments absorption peaks centered at 362 nm (UV cones), 415 nm (G cones), 480 nm (B cones) and 570 nm (R cones), zebrafish is capable of detecting and responding to light wavelengths ranging from UV to red [23-27]. In adult zebrafish, retina cones and rods are arranged into a highly-organized row mosaic scheme

with red and green double cones alternated with blue and UV single cones in a pattern 2:2:1:1. In this way, the red cone is always next to the blue one, and the green cone is always next to the UV one (Figure 3) [14, 22-24]. Rods insert into this highly organized mosaic, with four rods forming a square around each UV cone [28].

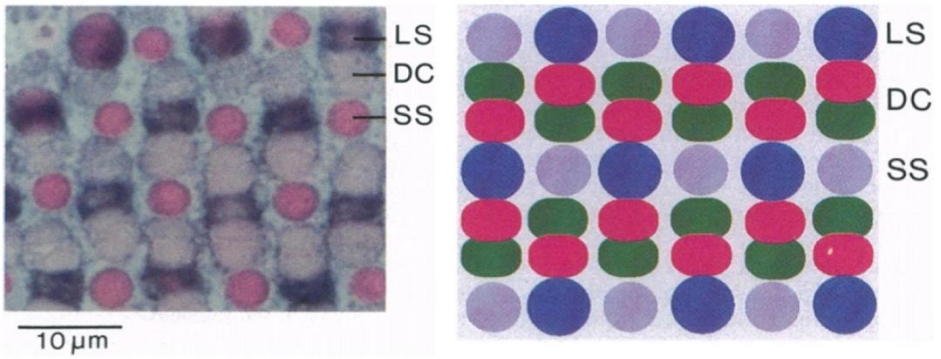

Figure 3. Adult zebrafish cone mosaic pattern.

In adult zebrafish photoreceptors are organized in a row mosaic pattern with red and green double cones (DC) between blue long single cones (LS) and UV short single cones (SS). In this pattern, the red cones are always next to the blue ones, whereas the green cones are next to the UV ones following the scheme shown in the figure. Figure from Meier et al., 2018.

In contrast to the adult stage, in larval zebrafish there is no cone mosaic arrangement, but the distribution of the different cone types vary across the larval retina, giving rise to a spatial anisotropy with functional implications (more in details in paragraph 1.3) [29]. Moreover, rods are not functional until 15 dpf [30]. Indeed, in early stages of development, zebrafish vision is mostly photopic, with scotopic vision kicking in only at about two weeks of development when the transition from larval to adult mosaic pattern begins developing [13, 24, 31, 32].

BCs. In the outer retina the first processing of chromatic signal from different PRs occurs with BCs receiving inputs from different rods and cone types [14]. These signals are modified by HCs, which establish feedback and feedforward connections with specific combination of PRs

and BCs, thus originating mono- and multiphasic spectral responses (see below). In adult zebrafish, there are 17 morphologically distinct BC types whose classification in ON- and OFF- type depends on the different response to light and type of glutamate receptors they express (the ON-type express metabotropic glutamate receptors, while the OFF-type AMPA/kainate ionotropic receptors) and also on the stratification of their axons across the IPL [21, 33-36]. The IPL is subdivided into two halves, the *sublamina a*, which is the outer half near ACs, and the *sublamina b*, the inner half near GCs. More in detail, BCs axon terminals in the *sublamina a* mediate OFF-type responses, thus hyperpolarizing in response to light, while processes in the *sublamina b* mediate ON-type responses, resulting in a depolarized response to light. BCs form presynaptic connection patterns with specific PRs (both cone-only and mixed-rod-cone connections; [14, 36]). Two-photon calcium imaging recordings in zebrafish larvae BCs axon terminals revealed that BCs can be classified in chromatic (selective to a specific wavelength), achromatic (responding to all wavelengths) and opponent (responding in an opposite manner to two different wavelengths; [29]). Zimmermann et al. [29] found UV chromatic ON-BCs in the IPL in the dorsal-frontal area of the larva visual field (corresponding, in the retina, to the temporo-ventral "strike zone (SZ)"), achromatic ON and OFF BC types, both excited or inhibited by all wavelengths tested, and color-opponent BCs. The latter are of two typologies: color-opponent BCs excited by red and inhibited by green, blue and UV; and opponent BCs excited by blue and UV and inhibited by red and green [14, 29].

HCs. HCs are second-order inhibitory neurons (GABAergic interneurons) and receive information from cones and rods synapses called pedicles. HCs are involved in early processing of color signals in the outer retina and are responsible for generating contrast enhancement, color-opponency and centre-surround receptive fields in cones and BCs, allowing to improve performance in the detection of spectral contrast and edges. Rods and cones convey information to HCs and BCs through specialized presynaptic structures called ribbons existing in their axon terminals. Cone terminals contain multiple ribbon synapses while rods have only a single ribbon

synapse. These presynaptic structures modulate a fast and sustained glutamate release resulting in HCs depolarization [14, 20, 37, 38]. HCs, in turn, feed back negatively onto the photoreceptors pedicle with which they directly interact (feedback connections) and pedicles of other cones (feedforward connections), thus mediating opponency in wavelength and space (lateral inhibition) [39]. Zebrafish retina is characterized by four types of HCs, three cone-contacting HCs (H1, H2 and H3 types) and one rod HC (RHC or H4 type) with different spectral and morphological characteristics [34, 40-42]. H1 cells contact R, G and B cones but not UV ones, H2 cells contact G, B and U cones but not R ones, H3 cells contact U and B cones only, and rod HC interact with rods. With these observations, Connaughton & Nelson [40] found that, in zebrafish larva, H1, H2 and H3 cells can be subdivided into six physiological cell subtypes. They pointed out six spectral classes of HCs with different types of spectral responses: two classes of luminosity HCs with a monophasic response named L-type (L1 and L2) hyperpolarized at all wavelengths, and four chromatic HCs named C-type, both hyper- and de-polarized depending on the stimulus wavelength. H1 cells identified by Li et al. [41] correspond to L1 and L2 subtype. The first are equally hyperpolarized by R and G cones, in addition to a "hidden opponency" from B cones, and are classified as R-/G-/(b+); the latter are hyperpolarized mainly by R cones and to a lesser extent by G cones (R-/g-). C-type horizontal cells are classified in biphasic, blue-triphasic, UV-triphasic and UV-tetraphasic. H2 cells correspond to C-type biphasic cells which receive depolarizing inputs from the R cones and hyperpolarizing inputs from G and B cones, denoted as R+/G-/B-. H3 cells are, in turn, of different types and correspond to C-type blue-triphasic, C-type UV-triphasic and C-type UV-tetraphasic cells. Blue-triphasic cells (r-/G+/B-/(u+)) hyperpolarize to red and yellow, depolarize to green, hyperpolarize to blue and hyperpolarize only for UV stimuli; UV-triphasic cells (r-/G+/U-) are hyperpolarized by red, depolarized by green and strongly hyperpolarized by UV stimuli; UV-tetraphasic HCs are denoted as r-/G+/B-/u+ thus receiving hyperpolarizing inputs from R and B cones and sign inverting inputs from the H2 cells and the other H3 cells via the UV cones terminals [14, 40, 41].

ACs. ACs are third-order inhibitory neurons and are the most heterogeneous class of retinal neurons, for their physiology, pharmacology and morphology. In a 5 dpf larva retina 28 different types of ACs have been identified and classified in ON-, OFF- or ON-OFF types depending on the response to light which evokes sustained or transient responses and on the stratification of their dendrites in the IPL sublaminae [14, 43, 44]. Indeed, by a morphological point of view, stratification of AC dendrites in *sublamina a* indicates they are ON-type, while stratification in *subilamina b* classifies them as OFF-type. From a physiological point of view, it has been found that transient ON-OFF AC types receive inputs mainly from red cones and to a lesser extent from green and blue ones, while sustained-ON and OFF ACs receive mixed signals both by red and green cones, thus resulting in a mid-spectral sensitivity (these cells sum signals received by red and green cones; [14, 43]). As for BCs, also some ACs are color-opponent, named as C-type, whose dendrites ramify in *sublamina b* so that they can be classified as ON-type. In adult retina it is possible to distinguish biphasic and triphasic ACs (the same classification found in HCs). Some biphasic ACs are red-green opponent receiving depolarizing input from red stimulation and hyperpolarizing inputs from green, blue and UV stimulation; while others are blue-yellow opponent, which depolarize to short wavelengths and hyperpolarize to long wavelengths. Some triphasic ACs depolarize to UV and green, and hyperpolarize to blue stimulation [14, 43]. ACs can be also divided into two main groups, the small-field type and the wide-field type. The first transfers information vertically across the IPL and modulates visual information processing locally, while the wide-field type conveys information laterally and shape visual signaling at a lager spatial scale. In mammals, small-field ACs use glycine as neurotransmitter, while the wide-field ones are GABAergic [45].

RGCs. RGCs receive, integrate and encode information about several parameters of the visual scene (i.e. color, motion direction, object size) from BCs and ACs. They then relay this information to specific retinorecipient areas in the brain which, in turn, influence different types of behaviors [14, 46, 47]. A complete connectivity map between the different zebrafish RGCs types and their target brain visual areas has been provided

by Robles et al. [46]. Fifty morphologically distinct RGCs types have been found in larval retina. Recordings in zebrafish larvae RGCs somata and dendrites pointed out different spectral responses and distributions of these cells across the eye, probably to satisfy the larva's behavioral demands in the natural environment (see below) [29, 48]. Larval zebrafish RGCs respond to light of different wavelengths with either transient or sustained ON-, OFF-, ON-OFF responses [35]. Stable light responses are evident at 4 dpf and color-opponent and non-opponent ones at 5-6 dpf. At this stage of development, robust spectral responses to UV and red have been recorded [14, 49, 50] and also direction-selective and orientation-selective RGCs have been observed [51-53].

1.2.2 Brain retinorecipient areas

At the larval stage, RGCs project mainly to the optic tectum (OT), that is the most dorsal part of the mesencephalon and the principal retinorecipient area in the zebrafish brain [19]. Beyond the OT, other retinorecipient areas have been identified and subdivided into nine nuclei known as arborization fields (AF1-9, Figure 4) [19]. Connections between RGCs axons to one or multiple AFs provide to the brain a representation of the visual field. Clearly, different types of connections are involved in the execution of specific behaviors. It has been demonstrated that AF7 participates to prey-capture responses [46, 54], while AF9 to the detection of the optic flow [55, 56].

Optic tectum. The OT, also known as AF10, is the largest retinorecipient area in Teleosts and it is homologous to the mammalian superior colliculus (Figure 4). Zebrafish OT is divided into seven distinct laminae in the following order, from the most superficial to the deepest layer: stratum opticum (SO), which is divided into two sublaminae; stratum fibrosum et griseum superficiale (SFGS) including its six sublaminae; stratum griseum centrale (SGC); stratum album centrale (SAC) and stratum periventriculare (SPV) [46, 57]. Most RGCs (97%) send their axons to the tectum generating retinotopically biased visual maps throughout the brain: nasal, temporal, dorsal and ventral RGCs axons project to posterior, anterior,

ventral and dorsal tectal neuropil, respectively [46]. Beyond the visual inputs, the tectum receives other sensorial information, generating and integrating different sensory maps. In zebrafish, each tectal lamina receives projections from several RGC types, thus establishing the functional specializations of this structure capable of processing different visual features (i.e. colors, luminance and contrast, visual motion direction, object size). Several studies, based on the use of genetically-encoded calcium indicators (see paragraph 1.6.3), allowed to dissect the connectivity patterns among these structures and monitor tectal neurons activity in response to a wide array of visual (among other sensorial) inputs [47, 51, 58, 59].

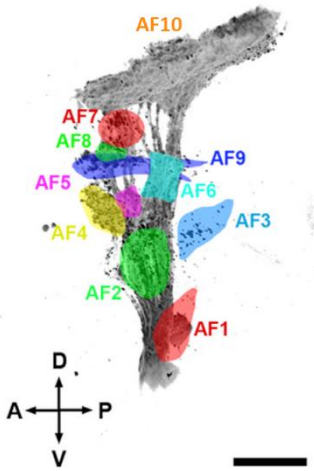

Figure 4. Schematic lateral view of optic tract and arborization fields.

Arborization fields formed by RGCs axon projections are termed AF1-9 in the panel and highlighted with distinct colors. AF10 indicates the optic tectum. Scale bar: 50 µm. Abbreviations: A, anterior; P, posterior; D, dorsal; V, ventral. Figure modified from Robles et al., 2014.

1.3 Environmental light spectral distribution and retina anisotropy

For animals inhabiting shallow freshwaters, such as zebrafish, the visual world and how it appears and it is processed by their visual system is very peculiar and depends on specific neural retinal circuits specialized in processing different parts of the visual field (and so light of different

wavelengths) in order to satisfy the different behavioral requirements. Along the water column, mid-wavelength light (green) dominates underwater horizon leading to a separation between the lower visual field of the ground which is dominated by long-wavelengths (red), and the upper visual field where short-wavelengths are predominant [29]. The short-wavelengths light dominating the upper visual field is scattered by the underside of the water surface giving rise to the Snell's window that is a featureless representation of the sky directly above the animal and it is an achromatic region (Figure 5) [15, 29]. Due to this spatial stratification of wavelengths, larval tetrachromatic retina is functionally and spatially anisotropic. Zimmermann et al. [29] mapped the distribution of cones and rods across the larval retinal surface pointing out a predominance of all photoreceptors, mainly R-, G-, B- cones at the horizon, and R-cones type in the lower visual field, thus indicating that there is a huge investment in chromatic circuits in this part of the eye. Conversely, the little color information in the upper visual field led to the development of achromatic circuits, probably specialized in detecting achromatic silhouettes along the water column. Interestingly, a large amount of UV-cones has been found in correspondence of the area temporalis (or "strike zone", 30° above the forward-facing horizon of the larva) which has been demonstrated to be involved in prey detection (Figure 5) [29, 60]. Indeed, zebrafish larvae are attracted by microorganisms (i.e. paramecia) inhabiting the upper water column which appear UV-bright when illuminated by the sun [29]. This behavior is also justified by the distribution and morphology of these cone types, which are broadly stratified and show an enlarged outer segment to increase the absorption surface for UV-photons detection [60]. Thus, the high anisotropy of the larval visual system leads to a different color-coding in the different parts of the eye. In this regard, different RGCs dendrites and somata play an important role in encoding visual information such as color, speed and shape [48]. A subset of RCGs in the strike zone shows an UV-ON response, thus corroborating UV-bright prey capture requirement [60], while other RGC types located in different retinal layers and parts of the eye exhibit different forms of color opponency, mostly a blue-OFF response. Thus, RGCs encode specific chromatic signals which are then

relayed, with a specific and regionalized code, to the brain regions receiving RGCs connections (for example the optic tectum and other RAs) [48].

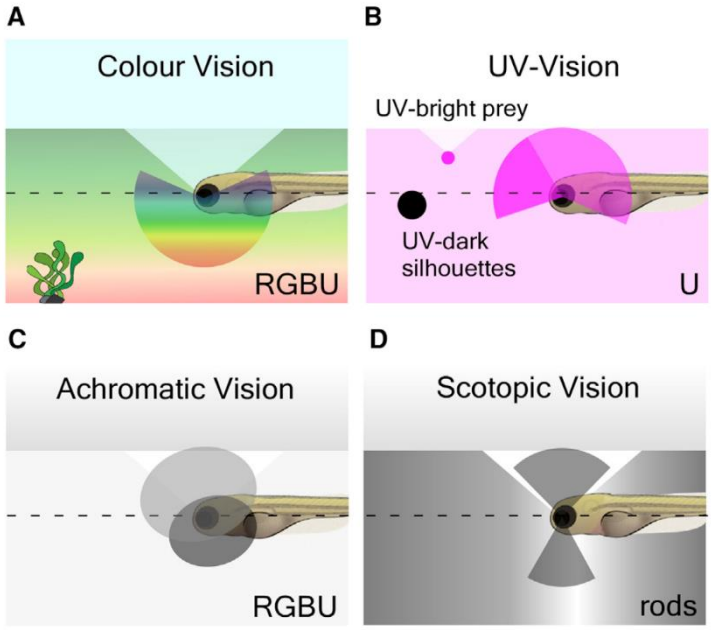

Figure 5. Chromatic organization of zebrafsih larva eye.

(A) Distribution of circuits responsible for color vision dominated by R, G, B and U cones are generally biased to the horizon and the lower visual field to match the chromatic content of zebrafish natural environment. **(B)** UV-circuits are abundant in the upper and frontal visual field, presumably used for prey capture of UV-bright paramecia and for the detection of UV-dark silhouettes (potential predators) against a UV-bright background. **(C)** Achromatic circuits are present throughout the eye and are classified into ON circuits in the upper-frontal visual field (light grey shape) and OFF circuits in the lower-outward-facing visual field (dark grey shape). **(D)** Rod circuits, responsible for scotopic vision, are used to map the sky and the ground respectively above and beneath the animal. Each panel shows the Snell's window highlighted by the triangle above the larva and the dashed line indicates the horizon. Figure from Zimmermann et al., 2018.

1.4 Functional organization of the larva visual system

RGCs are the link between eye and brain, projecting to ten arborization fields (AFs) in the diencephalon (AF1-6) and mesencephalon (AF7-10), where populations of neurons responsive to specific visual stimuli have been identified [46, 61]. Neuronal circuit schemes in which the retinal information, relayed to the tectum and here integrated vastly with other visual and nonvisual stimuli, is transmitted to the downstream CNS districts up to the spinal cord for further processing and to elicit a response have recently been investigated. It is known that a sensorimotor transformation, that is how a sensory input generates a motor output, is the result of a complex network between different neuron types distributed across multiple brain regions acting to generate a behavior. The main pathway originates in the nucleus of the medial longitudinal fasciculus (nucMLF) which directly elicits a motor command by the activation of motor neurons or via spinal interneurons (Figure 6) [61]. However, specialized subset of neurons localized in different brain areas are involved in the elaboration of visual stimuli encoding specific visually-related behaviors (i.e. swim speed and duration, turn amplitude, eye position) [3, 4, 56, 62-65]. In particular, forward motion is elicited by the nucMLF, while turning by ventromedial spinal projection neurons (vSPNs). Mauthner cells mediate escape swims and the left-right oscillatory activity in the hindbrain oscillator (HBO) is responsible for gaze direction and turning during swimming (Figure 6) [66]. Naumann et al. [3] describe the neural circuitry underlying the OMR and point out the role of distinct neurons organized in the rostro-caudal direction to allow propagation of the landscape motion information and consequent generation of a motor response. In this regard, color vision is an important sensory cue associated with specific behaviors both in zebrafish larvae and adults.

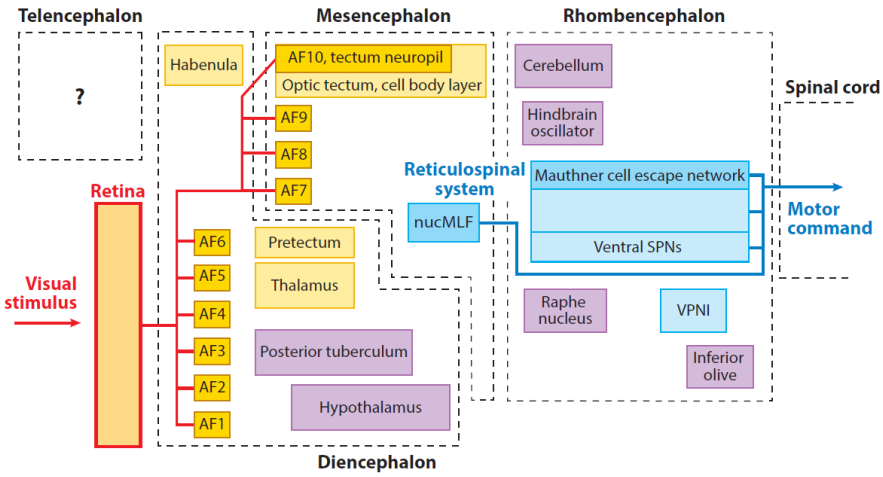

Figure 6. Schematic organization of zebrafish larva CNS.

The scheme shows the functional and anatomical organization of the zebrafish larva visual system and its connections in the brain. The first level of integration of visual stimuli occurs in the retina, which, through Retinal Ganglion Cells, projects directly or indirectly to the main mesencephalic and diencephalic areas (arborization fields, AFs, and other brain areas displayed in yellow) where visual inputs are further processed. Other diencephalic and rhombencephalic regions (highlighted in purple) are active in response to visual stimuli, probably changing the parameters of visuomotor transformations (i.e. cerebellum, hindbrain oscillator, inferior olive). The regions highlighted in blue, belonging to the reticulospinal system, participate in encoding motor outputs (e.g. swim speed, duration, turn amplitude). Abbreviations: AF, arborization fields; nucMLF: nucleus of the medial longitudinal fasciculus; SPNs, spinal projection neurons; VPNI, velocity-to-position neural integrator. Figure from Bollmann, 2019.

1.5 Visually-driven behaviors

Zebrafish larvae exhibit a broad visually-guided behavioral repertoire in response to the stimuli they are expected to encounter in their natural environment (for example luminance and contrast, object color and size, visual motion direction). This repertoire is evolutionarily well engrained in the morphological and functional organization of their visual system (Figure 6). Among the stimuli evoking strong responses there are whole-

field stimuli such as moving gratings and changes in luminance gradients eliciting responses across the retina, and local stimuli including flashes and moving spots affecting more restricted regions of the retina. Responses to whole-field motion include optomotor (OMR) and optokinetic responses (OKR).

OMR is an orienting swimming behavior in the direction of the optic flow. In this way the larva maintains its position in relation to the landscape motion. In the laboratory, it is evoked by grating patterns moving under the larva. In this way, the larva stabilizes its position following the direction of the moving pattern (Figure 7). **OKR** is a compensatory eye movement in response to whole-field motion to stabilize the image of the surrounding on the retina (Figure 8) [8, 9]. These behaviors allow the animal to perceive all translational and rotational directions of motion from both eyes and their underlying circuitries share components in the pretectum. Indeed, direction-selective RGCs (DSRGCs) convey information about visual motion direction to specific AFs, which, in turn, project to the pretectal area. Specific subpulations of pretectal neurons integrate directional signals from both eyes sending this information to the downstream pre-motor areas in the mesencephalon and rhombencephalon responsible of eliciting compensatory tail and eye movements, respectively [3, 4, 56, 63]. Color vision is strongly associated with these behaviors. It has been reported that long-wavelengths dominate optomotor circuits demonstrating that zebrafish larvae are red-green motion colorblind [67, 68], while short wavelengths affect phototaxis and prey capture [60, 68].

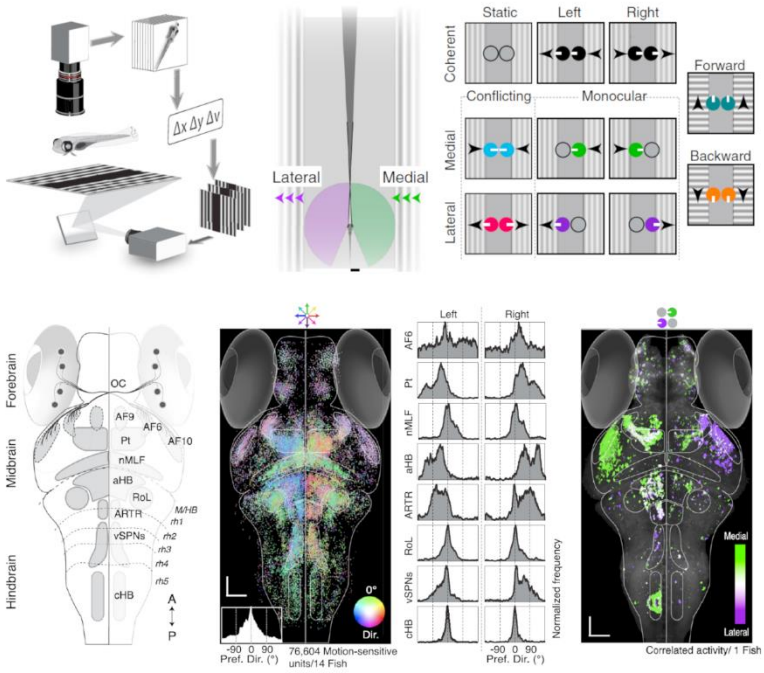

Figure 7. Whole-brain activity maps underlying optomotor response.

OMR is usually elicited in the laboratory by presenting under the fish striped patterns with different directions of motions covering both the monocular and binocular larva visual field. In addition to behavioral measurements, two-photon calcium imaging recordings are performed to correlate neuronal activity and behavior. The panel shows two-photon imaging of the whole larva brain during visual stimulation with moving gratings projected under the fish. As a result, a functional and anatomical map of neuron clusters responding to specific direction-selective stimuli have been obtained across the different larval brain regions. Figure from Naumann et al., 2016.

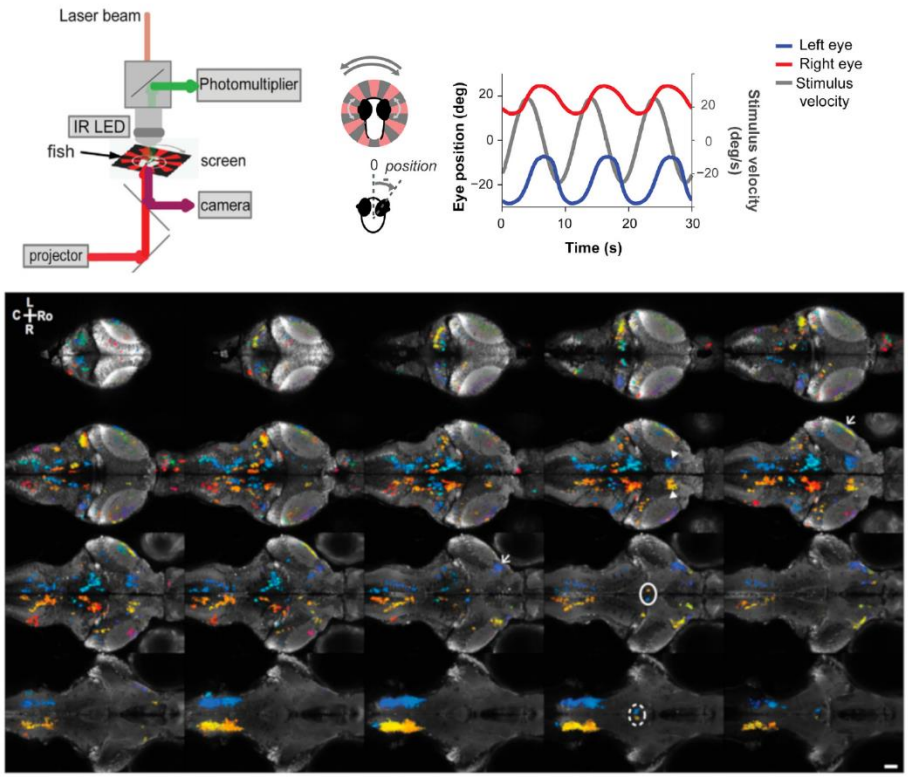

Figure 8. Whole-brain two-photon imaging during optokinetic response.

OKR is measured by presenting radial striped patterns rotating both in counterclockwise and clockwise direction. The sample is placed under the microscope with eye and tail free while measuring neuronal activity in response to visual stimuli. The panel shows neuronal responses triggered by optokinetic stimulus mapped in the whole larva brain highlighting the responsive neuronal clusters. Figure from Portugues et al., 2014.

Phototaxis is a light-induced behavior consisting in the detection of spatial illumination gradients resulting in a movement from dark toward brighter regions (positive phototaxis) [69]. This is a light-preference behavior based on the detection of environmental luminance variation from both eyes followed by a motor event. It can be elicited by presenting a bright spot in an open arena or projecting a dark/light split field under the larva [69]. Phototaxis assays have shown that larvae, when faced with a binary choice

between two colors, display a clear chromatic preference, with an especially strong UV avoidance [27]. Neuronal circuits underlying phototaxis are still under investigation, with some clusters of neurons participating to this behavior located in the hindbrain (the hindbrain oscillator). Recent studies demonstrated that RGCs send information about ambient luminance changes to the habenula that, in turn, relays this information to the hindbrain [62, 65, 70]. In addition to whole-field motion, zebrafish larvae also respond to small moving objects with different swim patterns. These behaviors (i.e. prey capture, looming-evoked escape responses, avoidance of large moving object), in opposition to the ones mentioned above, affect some restricted regions of the retina.

Prey capture appears at around 5 dpf, when zebrafish larvae become able to capture small ciliates such as paramecia. To perform this behavior, the larvae converge the eyes towards the prey and keep them in this position until the capture swim motor event ends. This strike movement is characterized by a stereotyped tail movement termed J-turn (Figure 9) [71, 72].

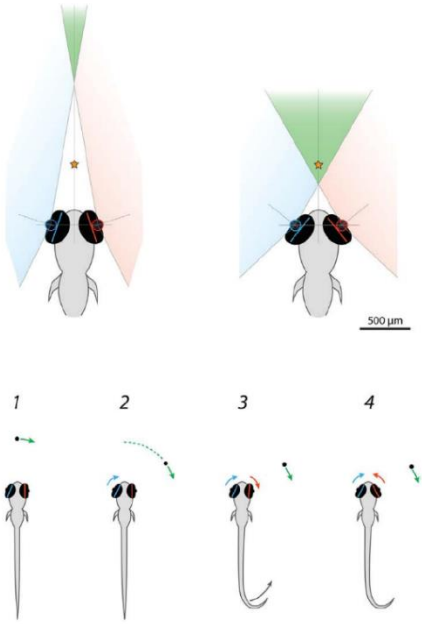

Figure 9. Prey-capture scheme.

The panel shows the sequence of events that characterize zebrafish prey-capture behavior simulated by presenting a small moving spot resembling a paramecium. When the prey appears in the binocular larva visual field, both eyes start following it and the stereotyped tail movement (J-turn) can be observed. Finally, both eyes converge towards the pray, maintaining this position until the capture maneuver ends. Figure from Bianco et al., 2011.

Neuronal circuits underlying prey capture involve RGCs specialized in detecting size tuning whose axons project to the superficial tectum neuropil and AF7 which, in turn, establish connection with the spinal projection neurons in the nunMLF midbrain, which is responsible for eliciting the capture event [47, 54, 71, 73, 74]. Thus, the mesencephalon plays an important role in object-size dependent behaviors [47].
Another escape-inducing behavior is the **looming response**. It is usually triggered by an incoming threat for the larva, simulated in laboratory experiments by an expanding dark disc (on a white background) projected into the larva visual field (Figure 10) [75]. Escape responses to looming stimuli termed C-bend involve the deeper layer of the tectal neuropil through a direct retino-tectal pathway, which could eventually involve the Mauthner-cells system [75, 76].

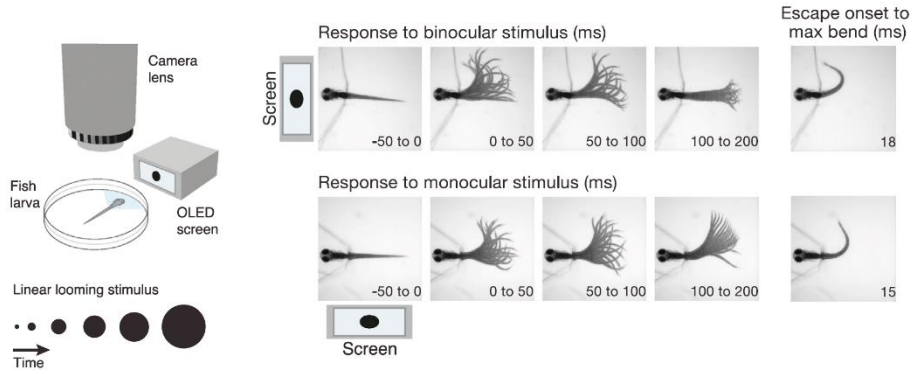

Figure 10. Looming-evoked escape response.

Looming stimulus consists of an expanding dark spot presented to the larva with a precise time sequence. In response to this stimulus, the larvae exhibit a stereotyped C-bend tail movement which can be tracked by embedding the samples in agarose maintaining the tail free and presenting the stimulus with a projector positioned in correspondence of the larva binocular field of view. Figure modified from Temizer et al., 2015.

Startle response is an escape behavior elicited by sudden transitions between light and dark and vice versa [69, 77]. The larva responds to this stimulus through a stereotyped escape known as O-bend. This behavior is subject to habituation and is affected by contrast due to variation in light

intensities before and after the flash. However, the neuronal basis underlying this response are still unknown.

1.6 Tools to dissect neuronal circuits and function

Given its structural complexity and the many scales involved in its working, the brain is the only part of the vertebrate body where the comprehensive relationship between structure and function remains still far from being resolved [78]. Indeed, a complete mapping of all neural connections in the brain and the investigation of their role is a goal still hard to reach, also considering the intricate wiring connections among the different neuron types which require methods for their detailed dissection. The first attempts to investigate brain structure-function relationship date back to seventeenth century with macro-level reconstructions based on the knowledge and techniques available at the time [79] which were later overcome by Golgi and Cajal in the nineteenth century, providing reconstructions at meso- and microscale level [80, 81]. In fact, it was at this time that the cell-based structure of the brain was determined with the first observations of the neurons and their morphology and the concept of synapse and neural network was proposed by Cajal. It was in the mid-twentieth century, with the development of the electron microscope, that it became possible to investigate brain connectivity patterns at the nanoscale level enabling to resolve single synapses and eventually starting to provide 3D reconstructions of neuronal circuits though on very small sample scales [82-85]. In this regard, the zebrafish larva represents the most suitable model for deciphering neuronal connectivity underlying its wide behavioral repertoire, also considering that most of limitations suffered by other models to achieve this task have been overcome in the larva. Indeed, the optical transparency, together with the small size of the brain and a relatively low number of neurons, enables to analyze activity and connectivity of all neurons in the whole brain of the living larva. This has been made possible thanks to neurons labelling with fluorescent probes or genetically-encoded fluorescent calcium indicators (among other

transgenic approaches) combined with *in vivo* high-resolution imaging techniques to record neuronal activity of labeled neurons in response to multiple stimuli and/or conditions. Any of the approaches aiming at deciphering the workings of an ensemble of neural circuits requires both the complete structural mapping of the network involved (at cellular resolution, Figure 11) and the functional measurement of activity in response to a given stimulus. Among the morphological mapping strategies, the use of Brainbow imaging to multi-label neurons with different fluorescent proteins provided examples of how to use colors as a guide to map neurons and their projections [86-88]. Another approach stems from the use of electron microscopy for 3D reconstruction, which provides a full morphological reconstruction of axons, dendrites and synapses that form neuronal circuits, enabling precise investigation of neuronal morphology [82-84, 89].

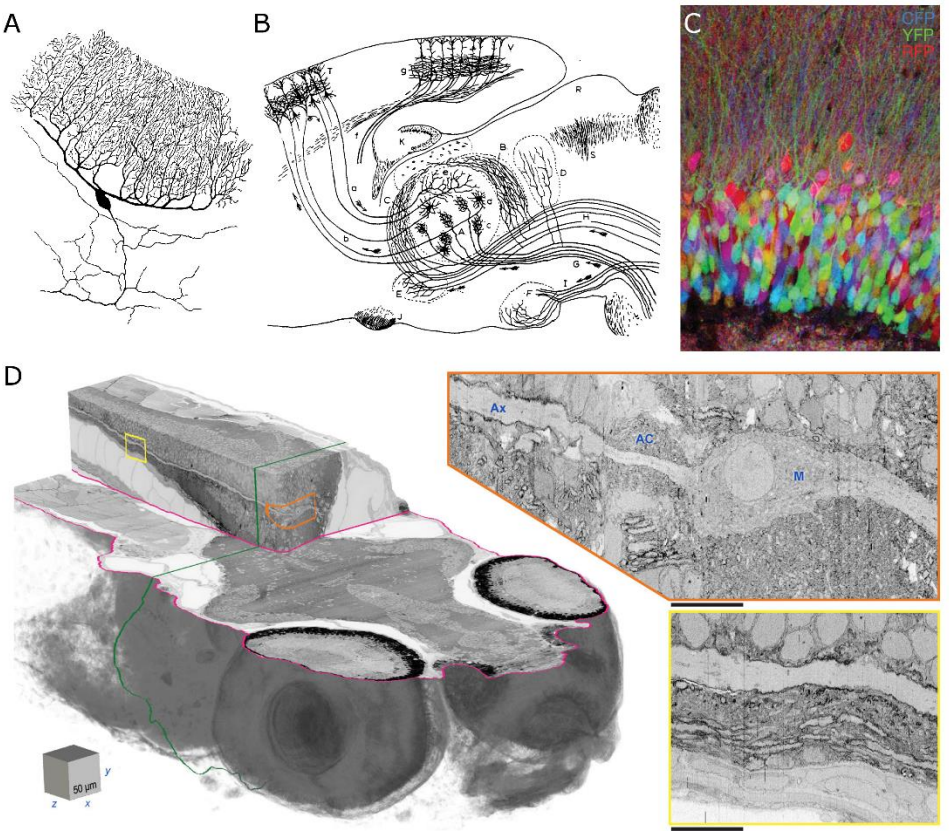

Figure 11. Historical milestones in circuit mapping.

(A) Purkinje cell from the cerebellum drawn by Golgi and reported in his Nobel Lecture. **(B)** Schematic of circuits in the thalamus drawn by Cajal. Figure from Cajal Nobel Lecture. **(C)** Brainbow expression in mouse Dentate gyrus. Figure from Livet et al., 2017. **(D)** Zebrafish larval brain targeted for serial-section electron microscopy. The insets on the right show a Mauthner cell reconstruction with the axon cap and axon (top inset) and the posterior Mauthner axon extension. Figure from Hildebrand et al., 2017.

To combine network morphology and function, in recent years, perturbative approaches such as light-activated ion channels, photo-inducible probes and laser ablation, started being used in zebrafish research for dissecting circuit function and for establishing causal relationship between neuronal activity patterns and behavior. Below, I will focus on the tools and techniques I used in my project.

1.6.1 Fluorescence

Fluorescence is the property of some molecules to absorb photons at a specific wavelength and to subsequently re-emit them (after a chain of photophysical events) at a longer wavelength. This phenomenon occurs in molecules having a characteristic electronic structure (i.e. fluorophores, fluorescent probes, dyes) well illustrated by the Jablonski diagram shown in Figure 12. These molecules possess electronic orbitals structures depending on the total electron energy and the symmetry of the spin state: a lower energy orbital, named ground state (S_0 in Figure 12), and higher energy orbitals (excited states S_1 and S_2 in Figure 12). Each of these electronic states is further divided into a manifold of rotational and vibrational levels with slightly different energies. At room temperature almost all the molecules are in the S_0 state, which is generally characterized by an electronic singlet with opposite spins electrons. The excitation of a molecule, which consists in the interaction between the electromagnetic radiation and the electrons in the molecule, occurs following absorption of a photon at a specific wavelength having an energy ($h\nu_{abs}$ in Figure 12)

matching the change in energy associated with the electronic transition from S_0 state to one of S_1 or S_2 manifolds of vibrational levels. This event is very fast, occurring within $\sim 10^{-15}$ s. The excited state is also a singlet since photon absorption does not change the electrons spin state. Given the presence of manifold of vibrational levels in the excited states, the molecule does not absorb a single wavelength but can actually absorb a band of wavelengths, so that each fluorophore has a specific absorption spectrum with a maximum absorption peak centered at a precise wavelength. Rapidly after the electron transition to the excited state, internal conversion occurs, consisting in the dissipation of vibrational energy in a non-radiative way (loss of energy without light emission) and resulting in the vibrational relaxation of the excited state electron to the lowest vibrational energy level of the fist excited state S_1. This phenomenon takes place within 10^{-14} to 10^{-12} s after excitation [90]. An important consequence of this rapid internal conversion is that all subsequent relaxation pathways proceed from the lowest vibrational level of the excited state S_1. After the internal conversion, the excited fluorophore decays from the lowest vibrational level of S_1 to one of S_0 vibrational levels. This event takes $\sim 10^{-9}$ s and can be associated with the emission of a photon ($h\nu_{em}$ in Figure 12) in a radiative process known as fluorescence. Also in this case, the presence of closely spaced vibrational levels in the ground state leads to the emission of photons with a wide range of energies (different wavelengths). Indeed, the fluorescence spectrum is the result of emission intensity over a band of wavelengths (emission spectrum) rather than a sharp line. As a result of non-radiative relaxation occurring before fluorescence emission, the emitted photon always has lower energy than the absorbed one and the emission spectrum is shifted towards longer wavelengths compared to the absorption spectrum. This is termed Stokes shift by the name of the scientist who discovered and described for the first time this phenomenon. This shift is measured as the difference in wavelength between the maximum peak in the excitation and emission spectra and it is peculiar to each fluorophore. However, electron decay to the ground state can occur through alternative non-radiative processes which happen with lower probability than fluorescence (the relative probability of radiative versus

non-radiative decay determines the fluorophore efficiency also termed quantum yield). One of these consists in the dissipation of the excited state energy as heat in a non-radiative process termed quenching. Another somewhat infrequent event is the intersystem crossing, which occurs when molecules in the S_1 state undergo spin conversion followed by the transition to first triplet state T_1 characterized by unpaired electrons (i.e. electrons with the same spin). The electron returns back to the S_0 state from T_1 state yields to the emission of a photon through a process termed phosphorescence, whose emission spectrum is shifted to longer wavelengths than the fluorescence one. The phosphorescence lifetime is longer than fluorescence and it occurs within 10^{-3} to 10^3 s. Molecules in the triplet state are highly reactive and the transition to the ground state can also occur through the interaction with the biological sample and/or the environment, leading to the production of reactive oxygen species (ROS) [91]. ROS are responsible for fluorophores degradation causing photobleaching (loss of fluorescence by photoinduced chemical degradation) and sample photodamage. Molecular oxygen is involved in this event reacting with the excited fluorophore in two different ways. First, a fluorophore in the triplet excited state can transfer energy to molecular oxygen with the resultant formation of the energetically excited singlet oxygen ($^1O_2$). Second, the electron transfer from the triplet state T_1 to the S_0 ground state can involve molecular oxygen causing the formation of a superoxide radical (O_2^-) (Figure 12) [91]. Both $^1O_2$ and O_2^- belong to the ROS family. Photobleaching is typical of most fluorophores. In fact, after the repetition of excitation and emission cycle several hundreds or thousands of times, the fluorophores fall into a non-fluorescent dark state due to photobleaching.

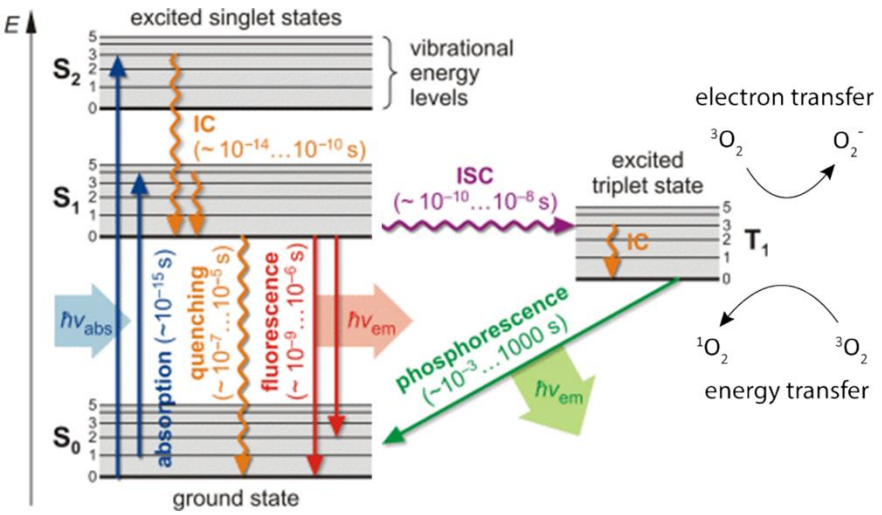

Figure 12. Jablonski diagram.

The diagram illustrates the singlet ground state (S_0), the first (S_1) and second (S_2) excited states. The thicker lines represent the electronic energy levels, while the thinner ones the vibrational energy states (rotational energy states are not shown). The colored arrows highlight transitions between the different states: transitions associated with absorption are indicated by the blue arrows (from S_0 to S_1 or S_2 state), whereas transitions associated with emission are highlighted in red. Emission is the result of the electronic transition from the lower S_1 energy state to the S_0 ground state. The wavy arrows indicate internal conversion (IC) or non-radiative relaxation processes (quenching). Transition from S_1 state to the first triplet state (T_1) is termed intersystem crossing (ISC). Electron transition from T_1 to S_0 state results in the emission of photons through phosphorescence. The panel also shows photobleaching event occurring as a consequence of oxygen electron transfer from T_1 to S_0 state or energy transfer leading to the formation of reactive oxygen species (ROS).

1.6.2 Green Fluorescent Protein

The Green fluorescent protein (GFP) was discovered and isolated by Shimomura and colleagues in 1961 from the Pacific jellyfish *Aequorea victoria*, together with the chemiluminescent protein aequorin (Figure 13) [92]. This discovery came from the observation that: “a protein giving solutions that look slightly greenish in sunlight through only yellowish under tungsten lights, and exhibiting a very bright, greenish fluorescence

in the ultraviolet of a Mineralite, has also been isolated from squeezates" [92].

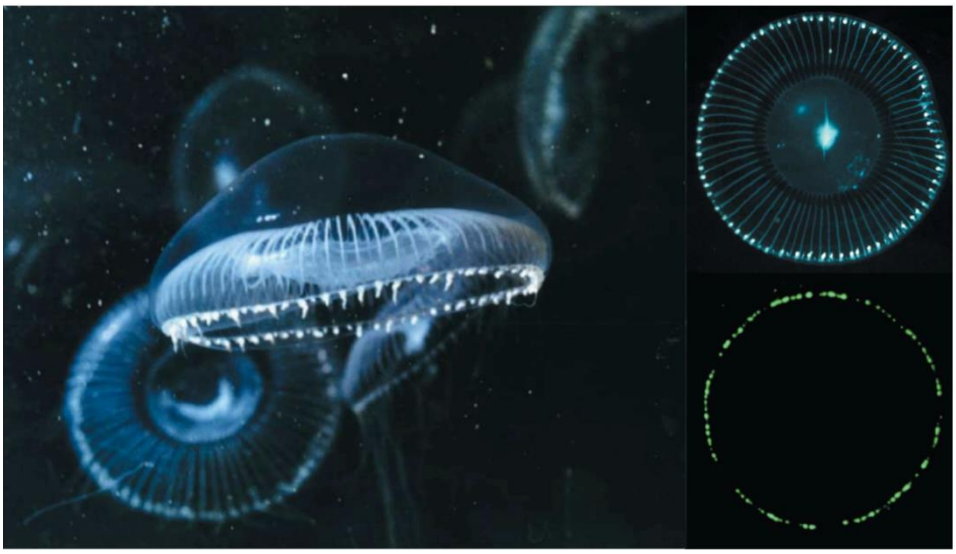

Figure 13. Aequorea victoria.

The jellyfish *A. victoria* (left panel) and its light organs located at the ring-edge of the umbrella in daylight at sea (top right) and in the dark (bottom right) where green fluorescence emitted by the GFP is visible. Figure adapted from Shimomura, 2005.

The emission spectrum of GFP peaks at 508 nm, the same peak of the green bioluminescence produced by living Aequorea tissue. Moreover, pure Aequorine chemiluminescence peaks at 470 nm as one of the GFP fluorescence excitation peaks [93, 94]. Subsequently, GFP was purified and crystallized, and its absorbtion spectrum and fluorescence quantum yield were measured [95]. Still in that year the FRET energy transfer mechanism from aequorin to GFP was confirmed. GFP crystal structure was first solved in 1996 independently by Yang et al. and Ormö et al. [93, 96]. The native GFP is a 238 amino acid protein (27 kDa) whose structure consists of a regular β-barrel with 11 strands (2.4x4.2 nm) threaded by an α-helix running up the axis of the cylinder [93, 94]. Moreover, small sections of α-helix also form caps on the ends of the cylinders. This structure, with a single α-helix inside a uniform β-barrel, represented at the time a new protein fold, which was named β-can [93]. The fluorophore is located inside the cylinder in correspondence to the α-helix central segment, a

highly protected position in order to avoid interaction and/or reaction with the surrounding environment (Figure 14). Already in 1979 Shimomura proteolyzed the denatured GFP and demonstrated that the chromophore is a 4-(p-hydroxybenzylidene)imidazolidin-5-one originated from an autocatalytic reaction of intramolecular cyclization involving the tripeptide Ser65-Tyr66-Gly67 [97]. In more details, GFP at first folds into a nearly native conformation and then a cyclization between Ser65 and Gly67 occurs, followed by dehydration and the intermediate imidazolinone formation. Finally, the Tyr66 side chain undergoes dehydrogenation by O_2 to put its aromatic group into conjugation with the intermediate, resulting in fluorophore maturation to its fluorescent form [94, 98-100]. This is an autocatalytic reaction and no cofactors or enzymes are required. GFP is very resistant to denaturation and in its native form it exhibits a main excitation peak centered at 395 nm and a minor peak (three times lower in amplitude) at 475 nm, whereas the emission peaks are at 508 and 503 nm, respectively (Figure 14) [93, 94]. Tyr66 is the amino acidic residue essential for the two GFP absorption peaks. Indeed, in its protonated or neutral form it is responsible for the UV absorption peak (395 nm), whereas the deprotonated or anionic form for the 475 absorption peak [93]. Due to protonation/deprotonation of the chromophore, GFP spectral properties are influenced by pH: an increase of pH promotes chromophore deprotonation making it more sensitive to 475 nm excitation; in contrast, lower pH values induce chromophore protonation promoting absorption at 395 nm [99, 101, 102]. During most cycles of light absorption/emission, the proton transfer eventually reverses. However, occasionally the proton does not return to the chromophore, so the neutral chromophore is photoisomerized to the anionic form. Thus, upon intense UV illumination, the 395 nm absorbance and excitation peak of the neutral form gradually declines leading to an increase of the 470 nm peak of the chromophore anionic form [94, 99, 101, 102].

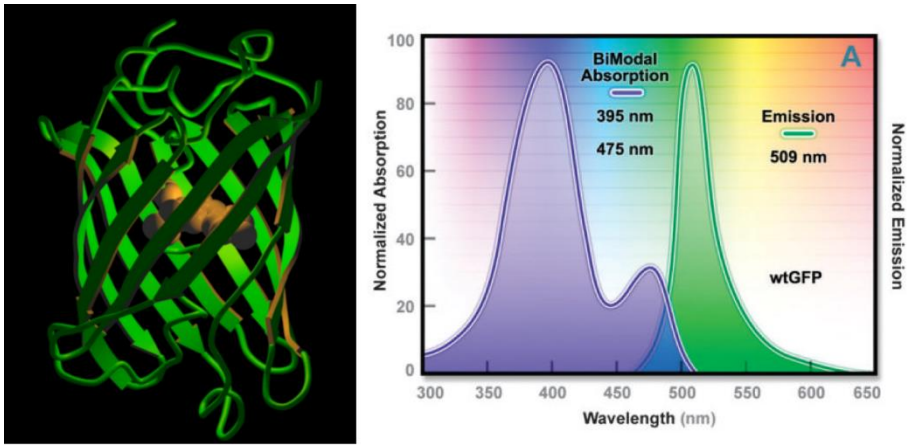

Figure 14. GFP structure and spectral properties.

Left panel: GFP crystal structure showing the 40 Å β-barrel consisting of 11 β strands with the fluorophore Ser65-Tyr66-Gly67 located and protected inside (shown in orange spacefilling). Right panel: wtGFP fluorescence spectrum characterized by two absorption peaks centered at 395 and 475 nm, and the emission one at 508 nm. Right panel adapted from Day and Davidson, 2009.

In 1992 Prasher et al. [103] cloned the GFP cDNA sequence and it was demonstrated that the expression of this gene (under a specific promoter) in other organisms, both eukaryotic (*Caenorhabditis elegans*) and prokaryotic (*Escherichia coli*), induced fluorescence [104, 105]. This was the demonstration that the gene contains all the information necessary for the chromophore post-translational maturation, without need for jellyfish-specific enzymes or cofactors. This discovery was a real breakthrough in biological research, since it showed that GFP could be used for monitoring gene expression and protein localization in practically any living organism. Subsequently, Roger Tsien by applying random chromophore mutagenesis produced a GFP variant named enhanced GFP (EGFP), characterized by a brightness 5-fold higher than wild-type GFP (with selection of absorption in the blue peak so to avoid the need for UV radiation) and an improved folding at 37°C [98]. Tsien also developed GFP spectral variants exhibiting absorption/emission spectra in different wavelength ranges (i.e. blue fluorescent protein, BFP; cyan fluorescent protein, CFP; yellow fluorescent protein, YFP) [98]. Osamu Shimomura, Roger Y. Tsiens and Martin Chalfie received the Nobel Prize in Chemistry in 2008 “for the discovery

and development of green fluorescent protein, GFP", undoubtedly one of the greatest revolutions in the field of biological microscopy.

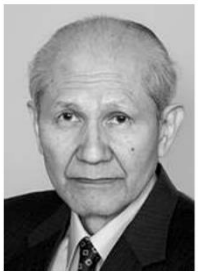
Osamu Shimomura


Martin Chalfie


Roger Y. Tsien

1.6.3 Genetically-Encoded Ca^{2+} Indicators (GECIs)

Calcium is a ubiquitous second messenger, playing an essential role for signal transduction in all cells, including excitable cells, such as neurons. Calcium ions (Ca^{2+}) are indicators of neuronal activity since they enter neurons during action potential (AP) firing and synaptic input, with dynamics that can be evaluated by measuring changes in intracellular [Ca^{2+}] that in resting state is ~100 nM [106, 107]. To monitor variations in intracellular [Ca^{2+}], calcium-sensitive dyes and genetically encoded calcium indicators (GECIs) have been developed [108, 109]. All these molecules feature the capability of binding Ca^{2+} ions reversibly, with high affinity and specificity, associating to calcium binding a variation of fluorescence emission, i.e. acting as fluorescent reporters. GECIs offer an extremely powerful tool in a variety of studies, since they allow calcium measurements without the need of invasive procedures (such as microinjection or other methods needed for organic dyes), and insuring selection of the cellular types in which the reporter is expressed (by construction under the appropriate promoter) [110]. GECIs include sensors based on the aequorin chemiluminescence, FRET-based sensors, or proteins expressing an intrinsic fluorescence such as the GFP. Among the Ca^{2+} indicator proteins, the GCaMP sensors family has found several applications in the last years. GCaMP protein and its variants consist of

circularly permuted GFP (cpGFP), the calcium-binding protein calmodulin (CaM) and the CaM-interacting peptide M13 [111, 112]. Circular permutation of GFP gave rise to variants in which the amino and carboxy terminals of the protein are positioned differently than in the native sequence. In detail, the original N- and C-termini are linked via a short linker peptide sequence, leading to the formation of a theoretical protein with a circular structure (lacking terminals) that can be cut in any position so that new N- and C-termini will be generated (Figure 15) [111]. It has been observed that the introduction of new termini into regular secondary structures may be tolerated in some regions of the protein, allowing folding to a biologically active conformation [113]. This approach allowed the insertion of other peptides (for example CaM and M13 in GCaMP indicators) in positions providing a significant improvement in the indicator sensitivity to [Ca^{2+}] variations and/or its dynamics. CaM has four Ca^{2+} binding sites and following the increase of [Ca^{2+}] it binds the ion and changes its conformation resulting in high affinity for the M13 peptide and CaM-M13 binding. In the first GFP-based Ca^{2+}-sensors, CaM and M13 were fused to the natural GFP C- and N-termini, leading to the formation of a sensor with a low Ca^{2+}-sensitivity, since the CaM-M13 complex formation/dissociation did not result in a substantial change of the β-barrel conformation and, therefore, did not affect significantly fluorescence levels. The use of cpGFP and the insertion of CaM and M13 in proximity of the chromophore (in correspondence of the new N- and C-termini in position 144 and 145, respectively) induced calcium-dependent conformational changes (including modulation access of solvent leading to deprotonation of the chromophore) causing an increased brightness with calcium binding (clearly exciting the chromophore at the appropriate 475 nm λ_{ex}) [107]. In absence of Ca^{2+}, a low fluorescence intensity is observed, since the chromophore is in its protonated form resulting in a reduced λ_{ex} absorption. Thus, GCaMP follows the GFP absorption and emission spectra (488 and 512 nm, respectively) and its green fluorescence intensity increases in presence of Ca^{2+}. The first GCaMP indicators suffered from low sensitivity and slow kinetics. In order to improve sensitivity, extensive mutagenesis at the interface between cpGFP and CaM has been performed,

giving rise to a wide array of GCaMP variants with different sensitivities and kinetics (i.e. GCaMP5G, GCaMP6s, GCaMP6m, GCaMP6f, for slow, medium and fast, respectively) [114]. Comparison between GCaMP5G and GCaMP6 sensors shows that the latter have similar baseline brightness and 1.1- to 1.6-fold increase in dynamic range. Ultrasensitive GCaMP6 sensors vary in kinetics, with the more sensitive ones having slower kinetics. GCaMP6s sensor is characterized by relatively slow kinetics (as suggested by its name), measured, for a single AP, with a 180 ms τ_{ON} and 550 ms τ_{OFF} (measured in mouse cortex *in vivo*, see Table 1) [114].

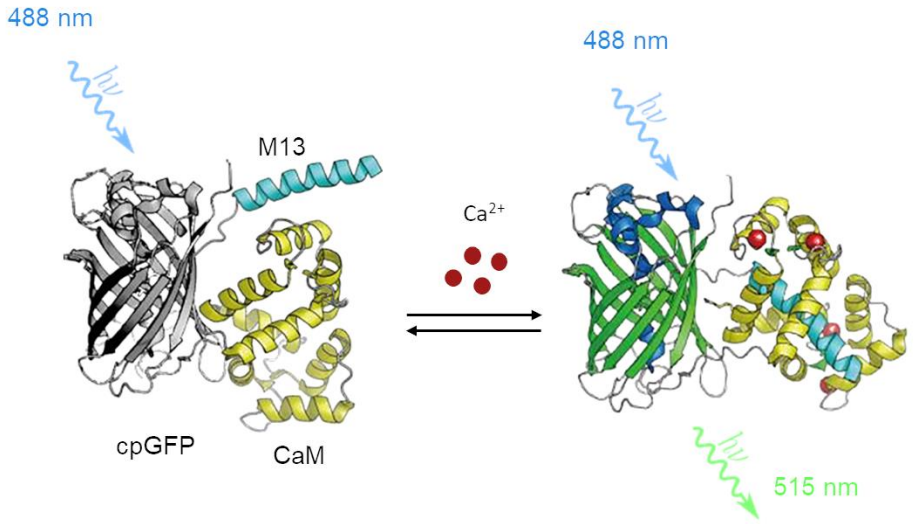

Figure 15. GCaMP structure.

GCaMP crystal structure and its constituents: circularly permuted GFP (cpGFP), calmodulin (CaM) and myosin light chain kinase M13 peptide. Illuminated by blue light (488 nm) and in presence of low [Ca^{2+}], GCaMP emits low fluorescence. Increase of [Ca^{2+}] followed by the Ca^{2+}-binding to the CaM domain induces a conformational change resulting in chromophore deprotonation and a brighter green fluorescence emission. Such process is reversible.

Moreover, calcium-saturated GCaMP6s is 27% brighter than EGFP [114]. Compared to GCaMP5G, GCaMP6f shows two-fold faster rise time and

1.7-fold faster decay time. Although it is the fastest genetically-encoded Ca^{2+} indicator, it is not capable of revealing single action potentials [114].

Sensor	$\Delta F/F_0$, 1 AP	Decay $\tau_{1/2}$ 1 AP (ms)	Rise τ_{peak} 1AP (ms)
GCaMP5K	3.6±1.9 %	268±20	60±20
GCaMP6s	23±3.2 %	550±52	179±23
GCaMP6m	13±0.9 %	270±23	80±7
GCaMP6f	19±2.8 %	142±11	45±4

Table 1. GCaMP sensors dynamics.

The table shows the kinetic features of some ultrasensitive genetically-encoded Ca^{2+} sensors. Data from Chen et al., 2013.

GCaMP indicators thus represent an ideal tool to image neurons as well as synapsis dynamics *in vivo* with cellular resolution. Moreover, given the presence of GFP in their structure, these sensors are characterized by a large two-photon cross-section (indicated as σ_{2P} for two-photon absorption, see next paragraph) making them suitable for high-resolution *in vivo* two-photon calcium imaging. The expression of GCaMP6 indicators at a pan-neuronal level in animal models, such as zebrafish, allows monitoring neuronal activity in the whole brain of the animal with cellular resolution.

1.6.4 Two-photon excitation

Two-photon excitation theory was described, for the first time, by Maria Göppert-Mayer in her doctoral dissertation at the beginning of the development of quantum mechanics [115]. She hypothesized that two or more photons of lesser energy together can cause a molecular excitation normally produced by the absorption of a single photon of higher energy. This process is named multiphoton or two-photon excitation (TPE) [116]. Two-photon microscopy [117] follows the above described theoretical prediction: two photons characterized each by half the energy necessary for an electronic transition interact with a molecule leading to its excitation in a manner equivalent to the absorption of a single photon with energy matching directly the transition energy. This event occurs if the two

photons interact with the molecule nearly simultaneously (i.e. within ~10^{-16} s), resulting in a quadratic dependence of the probability of excitation on the light intensity. For this reason, multiphoton processes, such as TPE, are often termed 'nonlinear' since the probability with which this event occurs does not depend linearly on the light intensity, differently from conventional one-photon excitation [116]. If the excited molecule is fluorescent, regardless of the pathway of excitation (one or two-photon absorption), the fluorophore returns to the ground state emitting a single photon of fluorescence with an emission spectrum akin to that obtained by one-photon excitation. Multiphoton absorption efficiency depends on physical properties of the molecule (i.e. two-photon cross-section (σ_{2p}), that is a conceptual molecular "surface" available for the collision of impinging photons, thus representing a quantitative measure of the probability of two-photon absorption) and on the spatial and temporal distribution of the excitation light [116, 118, 119].

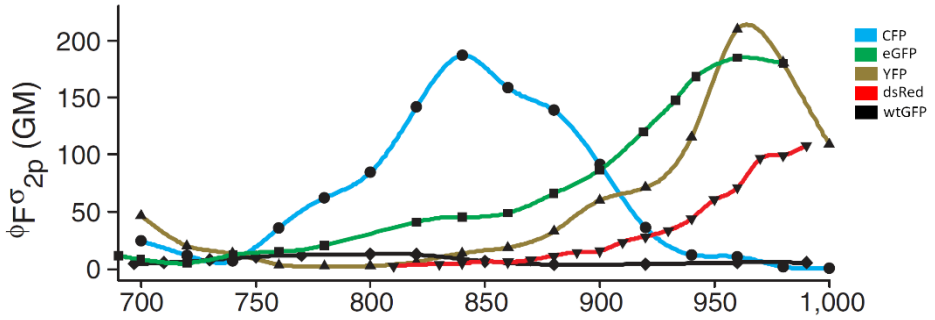

Figure 16. Two-photon action cross-sections.

Two-photon action spectra of five fluorescent proteins: cyan fluorescent protein (CFP, cyan trace), enhanced GFP (eGFP, green trace), yellow fluorescent protein (YFP, yellow trace), Discosoma Red (dsRed, red trace), wild-type GFP (wtGFP, black trace). Figure modified from Zipfel et al., 2003.

Since TPE occurs with extremely small probabilities, a high intensity is required to induce detectable two-photon excitation fluorescence. The intensity (I) is the number of photons passing through a unit area per unit time (photons·cm^{-2}·s^{-1}), while power is energy per second (1W = 1 J·s^{-1}).

Since the intensity depends on the area, it is greater at the focal plane (due to the focusing of the laser beam by a high numerical aperture microscope objective), whereas the total power is the same everywhere along the beam. Conversely, away from the focal plane TPE probability rapidly decreases and no detectable fluorescence is emitted. To achieve high temporal photon density and thus to further increase the probability that two photons will simultaneously interact with a molecule, a mode-locked pulsed laser is employed. The most common pulsed laser adopted in two-photon fluorescence microscopy (TPFM) is the titanium sapphire (Ti:S) laser. It produces ~80 million high peak power (from 0.5 to 1.5 W) pulses per second, each one with ~100 femtosecond duration, at a repetition rate of ~80 MHz [116, 118]. Ti:S laser is a tunable laser with a large spectral range emitting pulses in the near-IR wavelength range (~700 to 1100 nm). Since pulsed lasers emit ultrashort pulses of high peak intensity rather than a continuous wave, this contributes to keep in the sample the average power relatively low thus avoiding sample overheating and limiting cytotoxicity.

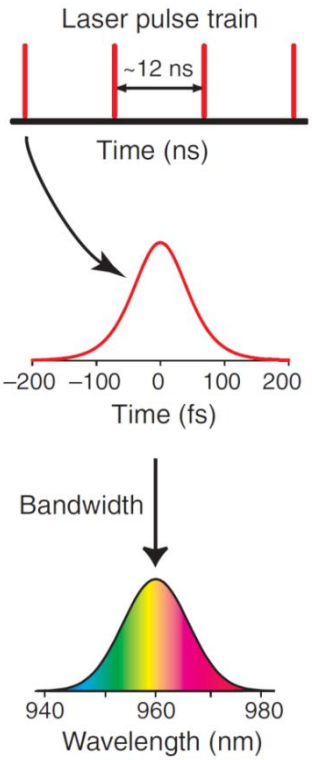

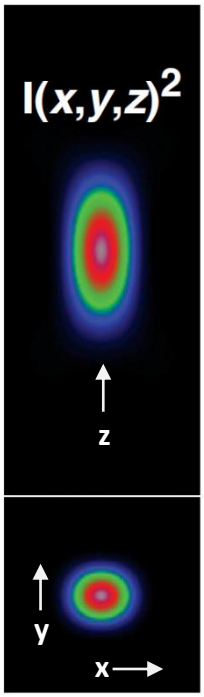

Spatial photon density is maximized in the sample by using a high numerical aperture (NA) objective, which focuses the laser beam to a focal spot (typically about 0.17 µm lateral radius and 0.45 µm axial radius, Figure 17) thus restricting the photons absorption (and so the sample excitation) to a very small volume (0.1 fL) in the focal plane (Figure 18).

Figure 17. Schematic Ti:S laser pulse and two-photon point spread function.

Left panel: pulse train (12 ns apart each other) from a Ti:S mode-locked laser at 80 MHz. The panel shows the 100 fs duration of each pulse and the corresponding bandwidth. Right panel: axial (top) and lateral (bottom) view of the two-photon illumination point spread function ($IPSF^2$). By approximating the $IPSF^2$ as a three-dimensional Gaussian volume, the focal spot assumes the following dimensions: 0.451 µm of axial radius (z) and 0.175 µm of lateral radius (xy). Figure modified from Zipfel et al., 2003.

Consequently, the photon density in out-of-focus planes drops off dramatically, resulting ina drastic reduction of photobleaching (permanent loss of fluorescence due to photon-induced chemical damage) and photodamagecompared to confocal microscopy. Another important advantage of two-photon excitation regards tissue penetration. In fact, one-photon excitation beam intensity dramatically decreases from the surface to the depth of a scattering tissue. This problem is much reduced with multiphoton microscopy, since the IR light used for excitation is scattered less efficiently by the tissue, allowing deeper imaging (several hundred microns depth up to one millimeter) [118, 120], minimizing the degradation of the excitation beam and keeping a high excitation efficiency (Figure 18) [118]. Zebrafish larvae, due to their optical transparency, allow deep volumetric imaging overcoming all limitations related to scattering tissues. Since two-photon microscopy excites a single spot, imaging requires raster scanning of the sample, which is obtained by moving the focal spot along the x-y-z axes, allowing 3D resolution and optical sectioning of the sample without the need of a spatial filter (i.e. the confocal pinhole) and eliminating image degradation due to scattering. Indeed, fluorescence emission in scattering tissues produces both ballistic (i.e. a photon not affected by scattering phenomena thus following its original direction of propagation) and non-ballistic (i.e. a photon whose direction of propagation is deviated because of scattering) photons. In confocal microscopy, the pinhole rejects non-ballistic photons resulting in a drop of fluorescence signal. Conversely, in multiphoton microscopy fluorescence is exclusively excited in the objective focal volume and so all photons emitted and collected derive from the excitation plane, resulting in intrinsic optical

sectioning. (Figure 18). For this reason, the use of the pinhole is not necessary, but rather a high NA objective is employed, collecting all fluorescence photons regardless of their ballistic or non-ballistic trajectories. Another advantage is that generally the two-photon absorption spectrum is larger than one-photon absorption one, thus allowing excitation of different fluorophores with the same laser avoiding chromatic aberrations and facilitating multicolor imaging [116].

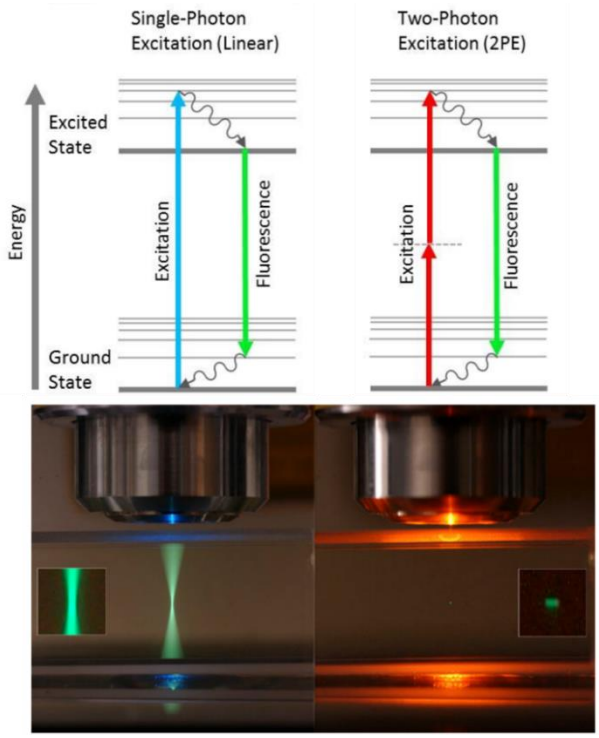

Figure 18. One- vs. two-photon excitation.

Upper panels: Jablonski diagram showing linear (left) and nonlinear (right) fluorescence excitation and emission. In one-photon excitation, the absorption of a short wavelength photon with high energy promotes the transition of the molecule to the excited state which then decays to one of the vibrational levels of the ground state resulting in a long wavelength fluorescence photon emission. In two-photon excitation, two photons having half of the energy (and, thus, double the wavelength compared to the single photon) induce the same excitation in the molecule, leading to the emission of a fluorescence photon. 488 nm cw laser (bottom left) and 960 nm pulsed laser (bottom right) focused into a quartz cuvette containing a dilute solution of fluorescein. In single-photon microscopy the excitation of out-of-focus planes generates an entire cone of fluorescence light (left) since single-photon absorption occurs within the entire focused beam. In contrast, two-photon absorption is restricted to the objective focal volume thus restricting the excitation to a small focal spot (right) avoiding multiphoton absorption away from the focus. Figure adapted from S. Ruzin and H. Aaron, UC Beckeley.

1.6.5 Laser ablation

Two-photon absorption can be also employed in targeted laser ablation experiments. Nonlinear absorption of femtosecond IR pulses focused through a high numerical aperture objective to a specific target can lead to a localized damage in living organism cells or tissues [121, 122]. Since the laser is focused into a small focal volume, this increases the probability of simultaneous multiphoton absorption resulting, at sufficiently high power, in a plasma formation (an ionized gas) in the focal volume [123]. Plasma formation is achieved following two steps: at first, molecule-bound electrons are released from their molecular orbitals and interact with the electric field of the laser pulse. The free electrons cause an impact ionization cascade in which an electron absorbs photons while colliding with molecules [123, 124]. These absorption events repeat until the free electrons achieve sufficiently high kinetic energy to ionize another molecule by impact ionization. As a consequence, micron-size plasma bubbles appear [123, 124]. The end of the laser pulse is followed by recombination of the free electrons with the ionized molecules at the focus (dynamics of 10^{-15} s), resulting in a strong increase of pressure within the excitation volume and leading to cavitation bubble formation and damage of the ablated region. Thus, the bubble is associated to the ablation site [124]. This technique found several applications in biology including laser-mediated ablation of cellular components (for example axons, micro-vessels), but it is also a powerful tool for the investigation of the neuronal circuits involved in response to specific stimuli and information processing. This was possible by combining laser-ablation methods with labelling of specific neurons, for example by loading specific dyes [125], or by the expression of GFP [55] or genetically-encoded fluorescence Ca^{2+} indicators [3]. The variation of the fluorescence intensity is very useful for monitoring the irradiation procedure in time and to localize the irradiated structure if long-term observations are performed. Moreover, the possibility to vary the position and the intensity of the laser beam with high precision together with laser penetration depth, allows site-specific and controlled irradiation. Several works report the application of this tool in

zebrafish to dissect neuronal circuits correlated with specific visually-driven behaviors. Among these, neuronal circuits responsible for escape behaviors and visually-evoked basic swim patterns emerged by the ablation of specific hindbrain neuron clusters [66, 125], whereas ablation of retino-tectal neurons highlighted their involvement in prey-capture execution [55, 71]. Laser-induced ablation is a destructive approach (restricted to the irradiated targets) and the transparency of larval zebrafish allows to apply this method with high efficiency also selecting as target neurons localized deep in the brain, taking advantage of two-photon absorption characteristics. Moreover, given the small size of the brain and a lower number of neurons, zebrafish is a good candidate to investigate the neuronal connectivity patterns acting to generate specific behaviors and within this context laser-ablation methods find numerous applications.

2. THESIS OBJECTIVES

The capability to discriminate colors is ubiquitous in nature and the visual system, in all species, has evolved to collect spectral information from the natural environment, which are crucial for behaviors and survival. Eye's photoreceptors are tuned to absorb selective wavelengths and their sensitivity is related to the spectral stimuli that the animals encounter in their natural habitat. This led to the diversity of color vision across species (i.e trichromacy and tetrachromacy) characterized by different types of specialized photoreceptors, among other retinal cells whose distribution vary both functionally and spatially. Chromatic signals thus trigger a signaling cascade from photoreceptors to the several retinal layers (where visual information is processed at different levels) and beyond. The importance of vision in zebrafish larvae is demonstrated by the rapid development of their visual system, their anatomical size (both in regards to the eyes themselves and to the brain areas dedicated to processing the signals coming from them), as well as the metabolic cost sustained already at the larval stage for the development and functioning of this system. Indeed, the relative volume of the total larval body is dominated by the eyes (this imbalance disappears in the adults) which contain half of the CNS neurons, resulting in a high dependence on this system to carry out most larval behavioral requirements. The functional and spatial anisotropy of the larval retina is fundamental to match the chromatic asymmetry of their natural environment underlying some spectrally-dependent larval behaviors. The retina anisotropy is determined by the different anatomical distribution of cones and rods photoreceptors across the eye, leading to the construction of a visual representation of the outside world mapped with the different wavelengths encountered along the water column [29]. Color vision has been investigated at various levels in zebrafish both by recordings of activity at cellular and synaptic level in the larval retina [29, 48, 60] and by performing behavioral tests based on measurements of color-driven behavioral choices in adults [126-130] and larvae [27, 68]. However, how spectral information spreads beyond the eye across the CNS

has not yet been investigated and this is the aim of my PhD project. This work investigated and mapped the anatomical distribution and spectral tuning of visually-evoked responses in the brain and part of the spinal cord of zebrafish larvae at two different stages of development (3 and 5 dpf) during visual stimulation with four spectrally-distinct stimuli with wavelengths matching the absorption peaks of the four zebrafish retina cones. We studied how the spectral information flow is conveyed and further processed beyond the first visual synapses (receiving inputs directly from the retina), and how these visual inputs spread across the CNS and the downstream areas involving also regions responsible for encoding motor events (i.e. the hindbrain and the spinal cord). We performed two-photon imaging and recorded neuronal activity *in vivo* in transgenic larvae expressing at the pan-neuronal level the nuclear-localized calcium indicator H2B-GCaMP6s. We pointed out preferred wavelength responses throughout the whole-brain volume of the larva and the spinal cord segments analyzed, providing anatomical and spectral maps with single-cell resolution. For this aim, the use of zebrafish larvae represents a fundamental model in the field of neuroscience, allowing *in vivo* volumetric imaging (due to the optical accessibility of the transparent larva) and single-cell measurements of activity (labelling whole neurons or specific clusters with Ca^{2+} fluorescent indicators) with the possibility to simultaneously apply different types of visual stimuli (among other sensorial stimuli) and monitor neuronal responses in the whole CNS. From the results obtained in this work, the presence of spectrally-distinct neuronal responses whose distribution is extended outside the main retinorecipient areas up to the spinal cord is revealed. The existence of wavelength-selective neurons in brain areas not directly involved in processing visual information (and not receiving retinal axon projections directly) is strongly related to the presence of circuits involved in color-driven behaviors. Moreover, a certain level of integration among multiple spectral stimuli has been demonstrated (as expected, more evidently in larvae at 5 dpf); whereas an inhibitory effect of light, specifically UV radiation, on certain anatomical structures (i.e. the pineal region) has been observed both in 3 and 5 dpf larvae. This work is the first investigation of

spectrally-tuned responses outside the retina, until now not described, providing spectral and anatomical maps of neurons involved in color-driven responses in the larva CNS and spinal cord.

My next goal was to set up laser-irradiation methods to induce a reversible inactivation of selectively irradiated neurons, without collateral damage to nearby neurons. We applied this technique to wavelength-responsive tectal neurons and observed that the perturbation lasted just few minutes, during which the cell stopped responding to spectral stimuli, followed by a recovery of both fluorescence and neuronal activity to initial conditions. Increasing the power of irradiation and taking advantage of GCaMP spectral properties, we also performed experiments to optically highlight the projections of some neurons in tectal neuropil inducing, in this case, an irreversible fluorescence increase. The effect of the irradiation procedure allowed us to reconstruct in 3D the axons projections of the tectal neurons in the neuropil otherwise not resolvable during two-photon scanning imaging. Both temporary and irreversible inactivation represent optimal tools for the study of local connectivity, applicable to the investigation of the networks underlying spectrally-evoked responses we mapped across the CNS.

In conclusion, this work provides single-cell resolution anatomical mapping of the distribution of spectral information across the larval CNS and spinal cord. We investigated the effect of colors beyond the retina and obtained a detailed characterization and anatomical localization of spectral responses to one or multiple spectral stimuli. We then implemented new optical tools to induce temporary loss of function of tectal neurons responding to visual stimuli and optical highlighting methods to trace their projections in the tectal neuropil lending this tool to the study of local connectivity.

3. METHODS

3.1 Zebrafish husbandry

To raise and breed zebrafish in the laboratory we use the aquaria system Z-Hub Mini System (Pentair, Florida, USA, Figure 19). It consists of a shelf with three rows of individual tanks of different volumes (1.5, 3, 10 L) with a maximum density of 3-5 fish/L (the low density is necessary to keep the water clean). Each tank presents an overflow tip on the back side equipped with grids of different diameters to prevent fish escaping and, on the upper side, a lid with a small hole (≤ 1 cm in diameter) to allow feeding and water supply. The system is provided with a pump for water recycle and filtration through biological and mechanical filters. In detail, tap water is carried through a mechanical 50 µm filter and a carbon filter to remove possible contaminants and chloride and then through a reverse osmosis system to desalt the water and reach a conductivity of about 20 µS and a pH of 7.5 and it is collected into a reservoir. Water enters into each tank through a series of outlets connected to a silicon tube (to adjust the water flow rate going inside them) and it is drained on the shelf through the overflow tip from where it is brought back by gravity into the filter system. A first coarse filter consists of a pad that blocks food debris (Figure 19A). Then the water is filtered through biological filters (BF150A, Sweetwater SW X Bio-Media, Pentair, Florida, USA; Figure 19B) which provide a large surface area for aerobic nitrifying bacteria thus degrading ammonium compounds produced by fish metabolism to nitrite and finally nontoxic nitrate. Normally 10% of the water is exchanged daily with fresh water allowing to keep the nitrate at a tolerable level (≤200 mg/L). In addition to biological filters, the system is equipped with mechanical filters: a 50 µm filter and an activated carbon one to remove small debris and particulate, and possible organic contaminants and heavy metals, respectively (Figure 19E,F). The system is also provided with an UV lamp in order to sterilize the water with UV radiation before redistribution to the tanks, thus reducing microbial and algal growth and diseases transmission (Figure 19D), and

with a 300 W heater to ensure the optimal water temperature at around 28°C (Figure 19C). The water quality parameters are constantly controlled since they are important to guarantee fish health and fecundity. Indeed, to maintain pH and conductivity values constant, on the side of the shelf are located two 5L containers with the following solutions: 8 g/L $NaHCO_3$ and 25 g/L Instant Ocean (mix of aquaria salts; Figure 19I). Water parameters are monitored by a control unit which activates peristaltic pumps that pump the solutions into the system if a pH and/or conductivity lowering occurs (pH < 7 and conductivity < 240 µS). To raise zebrafish according to their natural day/night cycle (14/10 h light/dark), LEDs have been installed above each row and controlled by a timer (Figure 19H). This artificial illumination reproduces the sunrise and the sunset with gradual intensity ramps, avoiding a sudden light switching on and off. We set the dawn at 9.00 and the sunset at 23.00. Zebrafish feeding consists of both live and dry food to keep them in good breeding conditions. We use Artemia nauplia, as live food, and dry food flakes of different kinds and grades (based on the fish age and the different nutrition values). Artemia were bought as cysts (Blue line, Macerata, Italy) and, after a chemical procedure of decapsulation to remove their outer shell, the embryos surrounded only by the chorionic membrane were stored in hypersaline (10% NaCl) at 4 °C. For hatching, artemia are placed in salt water (25 g/L NaCl, pH 9.0) at 28°C with constant illumination and aeration for 48h. Given the small size of zebrafish larvae and juvenile fish, they are feed with dry food (the smallest grade; Artemia grains grade 12, Blue line, Macerata, Italy) from 6 to 14 dpf and then the dry food is replaced with the Artemia nauplii freshly hatched, providing a high nutritional supply and encouraging pray capture. Adult zebrafish were maintained for breeding at 28°C on a 14/10 hr light/dark cycle according to standard procedure [131]. Embryos and larvae were raised at 28°C up to 5 days post fertilization (dpf) in 40 ml fish water (150 mg/L Instant Ocean, 6.9 mg/L NaH_2PO_4, 12.5 mg/L Na_2HPO_4, and 1 mg/L methylene blue, pH 7.2) in 9 cm diameter Petri dish.
All experiments were carried in accordance to European and Italian law on animal experimentation (D.L. 4 March 2014, n.26), under authorization n. 407/2015-PR from the Italian Ministry of Health.

Figure 19. Z-Hub Mini System.

System used to raise and breed zebrafish in the laboratory. The figure shows the following components: sump with pad filter **(A)** and compartment for nitrifying bacteria **(B)**; heater and air pump **(C)**; UV sterilizer **(D)**; 50 µm filter **(E)**; carbon filter **(F)**; pH and conductivity sensors **(G)**; illumination **(H)**; 5L containers with pH and conductivity solutions **(I)**.

3.2 Zebrafish larvae preparation

We employed 3 and 5 dpf Tg(elavl3:H2B-GCaMP6s) zebrafish larvae (ZFIN line *fi2Tg* [132]) with pan-neuronal expression of the nuclear-localized calcium indicator GCaMP6s (Figure 21A) [133, 134]. The transgene for GCaMP6s expression was carried in a heterozygote albino *(slc45a2^{b4})* background. Incross of adults allowed selection of larvae positive for GCaMP and homozygote albino for use in the measurements, so to completely avoid the presence of skin pigments. In order to select the larvae positive for the transgene, a fluorescence-based screening was performed. For this aim we used a stereomicroscope (Stemi 508, Carl Zeiss, Oberkochen, Germany) and a 470 nm blue LED (M470L3, Thorlabs, Dachau, Germany) for GCaMP excitation equipped with a specific filter (FF01-469/35, Semrock, Rohnert Park, California, USA). A pair of green filters (FF01-520/35, Semrock, Rohnert Park, California, USA) were mounted into the microscope eyepieces in order to detect GCaMP emission wavelength and at the same time block the excitation one, so that we were able to select only the homozygote albino larvae expressing the GCaMP

indicator in the whole CNS. Regarding the mounting procedure, each larva was transferred into a reaction tube containing low gelling temperature agarose (A9414, Sigma-Aldrich, Saint Louis, Missouri, USA; 1.5% w/v in fish water) at 38°C, and then quickly drawn into a glass capillary tube (O.D. 1.5 mm, I.D. 0.86 mm, length 10 cm, B150-86-10, Sutter Instrument, Novato, California, USA) using a pipette (Figure 20). After gel polymerization, the larva was extruded from the capillary and positioned dorsally (with the dorsal side oriented toward the microscope objective) on a microscope slide (76x26x1 mm, Marienfeld, Lauda-Königshofen, Germany) by appropriate rotation of the extruded agarose cylinder (Figure 20). The cylinder was then covered with a small drop of melted agarose. To minimize movement artifacts, the larva was paralyzed with 4 mM d-tubocurarine (T2379, Sigma-Aldrich, Saint Louis, Missouri, USA) dissolved in fish water (10 min pre-incubation before measurements followed by washing with fish water). Experiments were performed at room temperature.

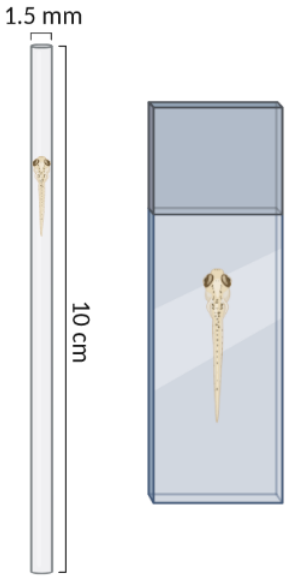

Figure 20. Schematic sample mounting procedure.

The larva is transferred inside the glass capillary cylinder (outside diameter 1.5 mm, length 10 cm) embedded in 1.5% low gelling temperature agarose (left figure). After gel polymerization it is extruded from the tube and positioned on a microscope slide with the dorsal side up embedded in a drop of melted agarose (right figure).

3.3 Two-photon calcium imaging and visual stimulation

Imaging during visual stimulation was performed with two-photon microscope (Bergamo II Series, Thorlabs, Dachau, Germany;) equipped with a Ti-Sa laser (Chameleon Ultra II, Coherent, Santa Clara, California, USA) with 140 fs pulse duration and 80 MHz repetition rate, tuned to 920 nm for GCaMP 2P excitation. The raster scanning was obtained by a couple of galvo-resonant mirrors (LSK-GR12(/M) 12 kHz): a resonant scan mirror (resonance frequency 12 kHz) deflecting the IR laser beam along the X-axis and a galvanometric mirror performing the slower Y-scan, thus enabling a high-speed scan across the larval brain. A 20x/0.95 NA water immersion objective (Olympus, Tokyo, Japan) was mounted on a piezoelectric motor for fine axial adjustments along the z-axis. GCaMP green fluorescence emitted by the sample was detected using PMT (PMT 2100, Thorlabs) and band-pass filtered using a 520/35 nm filter (FF01-520/35, Semrock, Rohnert Park, California, USA). Imaging was performed with a field of view (FOV) of 920x720 μm^2 and a resolution of 0.9 µm/px. A mosaic acquisition was implemented to cover the whole larval encephalon and about one quarter of the spinal cord: this required acquisition of two adjacent FOVs, shifted by about 700 µm along the larva longitudinal axis. To obtain a full 3D acquisition of the CNS volume of interest, z-scans were performed on each of the two FOVs. The range of the z-scan, sampled with 5 µm steps, was adjusted based on the depth of the CNS area to be imaged (270 µm for the encephalon and about 120 µm for the spinal cord). The total scanned area was 1500x720 μm^2 and variable depth as specified above. For visual stimulation, we used four LEDs (M365L2, M420L3, M470L3 and M590L3, Thorlabs, Dachau, Germany) with emission spectra centered on the absorption peaks of zebrafish cones (Figure 21B, C). The LEDs are indicated as L_1, L_2, L_3 and L_4 in Figure 21B. L_2, L_3 and L_4 were equipped, respectively, with band-pass filters FF01-420/10, FF01-469/35 and FF01-600/14 (Semrock, Rohnert Park, California, USA) to restrict the relatively broad spectrum of LED emission to a narrow band for selective cone excitation (corresponding to the

absorption peaks at 362, 415, 480, and 570 nm of UV, S, M, and L cones, respectively) [23, 25-27]. The LED sources were mounted on the stage of the microscope and coupled into one optical path with three dichroic mirrors (FF376-Di01, Semrock, Rohnert Park, California, USA; DMLP425R, and DMLP567R, Thorlabs, Dachau, Germany, respectively DM_1, DM_2 and DM_3 in Figure 21B) so that all stimuli were presented to the larva from the same direction. The intensity of the four LEDs was measured and adjusted at 1 mW/cm^2 (using power meter PM100D, Thorlabs, Dachau, Germany). LED flashes (100 ms duration) were presented to the larva in a sequence of 12 regularly paced stimuli (12.5 s apart from each other, see Figure 21D) and synchronized with the microscope acquisition program (ThorImageLS) using a NI USB-6002 (National Instrument, Austin, Texas, USA) controlled by a custom software written in LabView. Based on the dynamics of the GCaMP6s indicator, we observed that the response of activated neurons typically consisted of a fluorescence spike fully returning to the baseline levels in about 12 s after the stimulus. Therefore, we spaced visual stimuli by 12.5 s from each other. Sampling the four stimuli of interest thus required 50 s for each repetition and we performed a set of three repetitions to ensure a reliable regression analysis (see paragraph 3.5). Each acquisition was controlled by a custom script written in ThorImageLS and performed in "streaming mode" (i.e. at the maximum sampling velocity allowed by our chosen FOV size and resolution), so that each scan of the FOV required 420 ms and the complete set of stimuli and fluorescence imaging on each plane required 176 s (i.e. 418 frames), comprising an initial resting time of 20 s before visual stimulation was performed. Moreover, the ThorImageLS script controlled piezo iterations through the volume of the sample ($\Delta z = 5$ μm) and it depended on an external trigger from the NI USB-6002 for starting each acquisition so to synchronize the phase of visual stimuli with the image acquisition. The CNS 3D acquisition we performed consisted of about 54 planes for the encephalon and 25 for the spinal cord, so that the whole experimental recording required about 3h 40m.

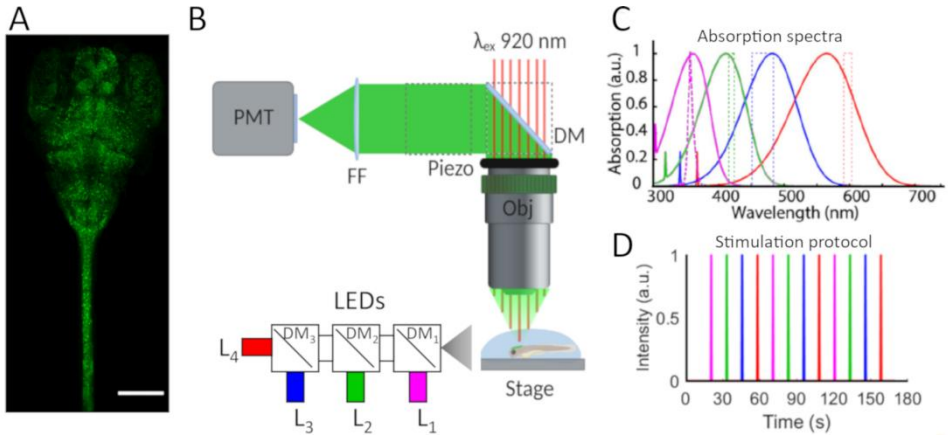

Figure 21. Experimental setup and visual stimulation protocol.

(A) H2B-GCaMP6s fluorescence maximum intensity projection of the CNS of a 5 dpf larva. Scale bar: 200 µm. **(B)** Schematic of two-photon microscope used for imaging zebrafish larva brain combined with visual stimulation. The larva is mounted on the microscope slide with the dorsal side up embedded in agarose. Stimuli are presented dorso-frontally using LEDs with four different wavelengths. Abbreviations: GM: Galvanometric mirror; FF: Fluorescence filter; DM: Dichroic mirrors; Obj: Olympus 20x, 0.95NA, water immersion; L_1, L_2, L_3, L_4 are the LEDs used for visual stimulation. **(C)** Normalized absorption spectra of zebrafish cones (solid lines; modified from Guggiana-Nilo and Engert, 2016) overlapped with the LEDs emission spectra (dashed lines) used for visual stimulation. **(D)** Protocol of visual stimulation.

We did not turn off the PMT during stimulus presentation (and so we did not temporally separate visual stimulation from recording during two-photon scan pattern). Two emission filters in series (FF01-520/35, Semrock, Rohnert Park, California, USA) were placed in the detection pathway resulting in a drastic reduction of stimuli bleed-through. Figure 22 shows residual stimulus detection visible especially for the shorter wavelengths. During analysis the frames acquired during the application of the stimulus were removed. Figure 22 demonstrates total suppression of any possible light artifact from our analysis. The delayed and fairly slow onset of GCaMP6s response insures that the elimination of the frames with the stimuli does not affect at all the detection of neuronal response.

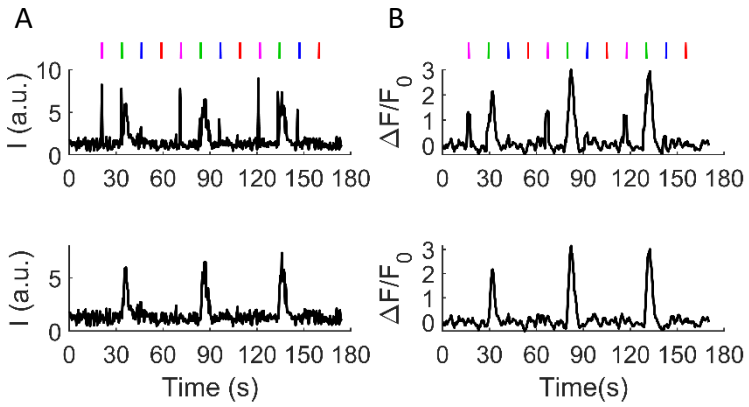

Figure 22. Suppression of light artefacts.

(A) GCaMP time fluorescence raw intensity data measured from PMT in ROI selected for the example without removal of the frames where the stimuli appear (top panel). Stimulus time points are indicated in their respective colors above the trace. The L_1, L_2 and L_3 light flashes are clearly visible as signal spikes in the trace (with decreasing amplitude for increasing wavelengths from L_1 to L_3), due to bleed-through of the LED light in the detection pathway; the L_4 stimulus (red) is not detected, being entirely filtered out by the fluorescence filters placed in front of the PMT. Bottom panel shows the same trace after elimination of the frames with the stimuli. **(B)** Corresponding $\Delta F/F_0$ traces obtained by applying Matlab *msbackadj* and *smooth method* (see paragraph 3.4). The top trace is shown only to display what the effect would be on the $\Delta F/F_0$ traces if stimulus frame were not removed. The bottom trace is an example of the type of data analyzed throughout our work.

3.4 Automatic neuron segmentation and calcium dynamics analysis

For each plane (sampled for 176 s during visual stimulation) a maximum intensity projection (MIP) was produced to obtain the highest contrast for the nuclear-localized calcium indicator (Figure 23A, C). Automatic segmentation was performed on the MIP image with a Matlab routine adapted from Kawashima et al. [135]). This analysis produces a segmentation image that is an overlay of the MIP with the identified neurons highlighted with individual colors (Figure 23B, D). Consistently with the size of each neuron at the magnification of our imaging, segmented

neurons were represented as a cluster of 13 pixels in a pattern 1,3,5,3,1 (Figure 23E).

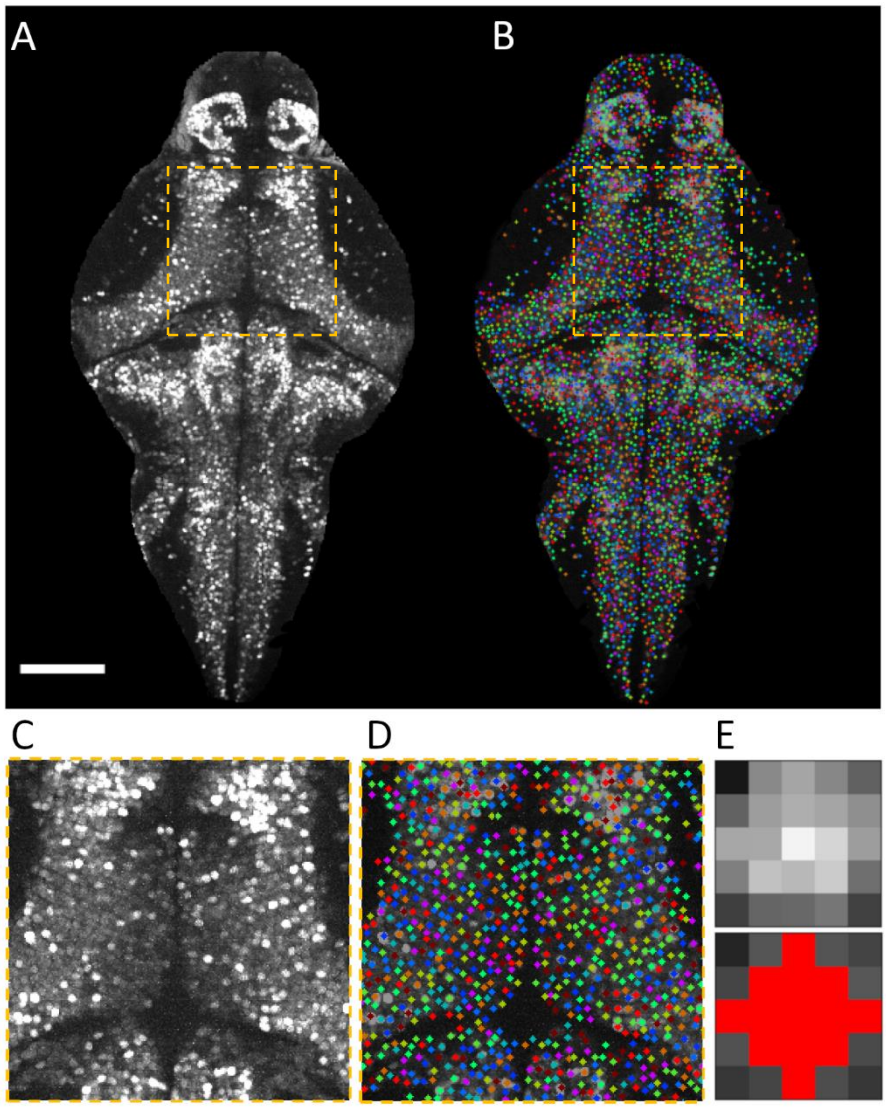

Figure 23. Automatic neuron segmentation.

(A) GCaMP fluorescence MIP of a selected plane of a 5 dpf Tg(elavl3:GCaMP6s-H2B) zebrafish larva viewed dorsally and corresponding segmentation image **(B)** obtained by applying the Matlab script for automatic cell detection adapted from Kawashima et al., 2014. Each identified cell is labeled with an arbitrary color. Scale bar: 100 µm. **(C)** Magnified view of an optic tectum area (highlighted by the orange

dashed square in A) displaying cellular resolution of imaging. **(D)** Enlarged view of B displaying segmented neurons. **(E)** Fluorescence intensity levels of a single neuron represented by a cluster of pixels (top panel) and overlay with the 13-pixels cluster resulting from segmentation analysis (bottom panel).

The fluorescence intensity integrated in the 13-pixel cluster attributed to each cell (F(t), Figure 24A) was processed through the 176 s of recording for each plane to obtain the $\Delta F/F_0$ normalized traces, as follows. A running average (window size 21 s, step size 0.84 s) was calculated on the F(t) trace using Matlab *msbackadj* to obtain a baseline (shown in red in Figure 24A) that was used as a measurement of F_0 in the calculation of $\Delta F/F_0 = (F(t) - F_0)/F_0$.
Each $\Delta F/F_0$ trace was then smoothed by applying Matlab *smooth* function (window size 2.1 s). The resulting trace is shown in Figure 24B.

3.5 Responsive neurons identification

Identification of neurons responding selectively to the visual stimuli was based on linear regression analysis on individual $\Delta F/F_0$ recordings. Analysis was performed using a custom Matlab script written following the method described by Miri et al. [136] to measure the degree of responsiveness of each neuron to each stimulus. The time-dependent sequence of the controlled stimuli (Figure 21D) was convolved with the calcium impulse response function, modeled in our system with an exponential rise time 1.5 s and decay time 2.1 s (Figure 24C); these values were found empirically to best match the typical time course of the observed GCaMP6s fluorescence peaks associated with the visual stimuli. Time separation between adjacent stimuli ensured orthogonality of the four vectors describing the time trajectory of each spectrally-distinct stimulus. These vectors are the columns of the matrix G subsequently used for regression analysis: a four-element vector β was obtained by linear regression $\hat{\beta} = G^T(\Delta F/F_0)$ with each element representing the regression coefficient for each stimulus in the neuron under analysis. From these coefficients, a T-score was calculated as follows:

$$T_i = \frac{\beta_i}{\sqrt{\frac{\varepsilon^2}{n-3}}}$$

With $\hat{\varepsilon} = (\Delta F/F_0) - \hat{G}\,\beta$ (which represents the residuals between regressed and measured data), β_i with i = 1,2,3,4 for L_1, L_2, L_3 and L_4 stimulus respectively, and n = 418 time samples of the recording. Figure 24D shows an example of a $\Delta F/F_0$ trace with the corresponding T-values extracted with this analysis for each stimulus and the resulting fitted trace based on the measured β values, demonstrating the effectiveness of the regression analysis.

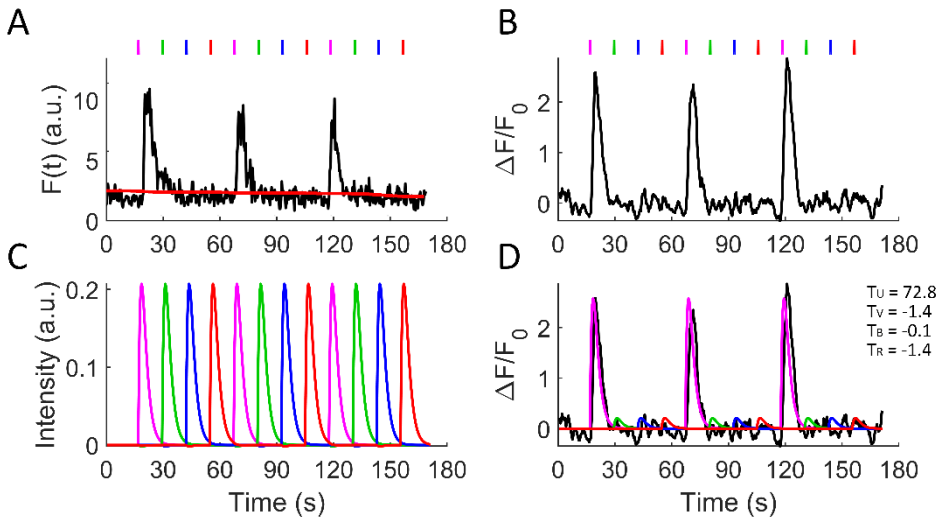

Figure 24. Regression-based identification of responsive neurons.

(A) Fluorescence intensity F(t) measured in the 13-pixel cluster attributed to a cell selected as an example (F_0 is shown with the red line). Stimulus time points are shown at the top. **(B)** $\Delta F/F_0$ trace. **(C)** Visual stimuli normalized regressors obtained by convolution of the time-dependent sequence of stimuli with the calcium impulse response function. Each stimulus type produces a regression vector (shown with its color-code in the panel). **(D)** Fitted regression data (colored trace) and corresponding T values.

Once a set of T values (one for each stimulus wavelength) was attributed to each segmented neuron, we wanted to automatically and reliably select neurons displaying a specific spectrally-selective response. For this purpose, a T threshold (T_{Th}) specific for each stimulus was chosen so that the percentage of false positives (false discovery rate, FDR) would be 1%. To select the T_{Th} value fulfilling this requirement for each stimulus, we compared the normalized T distributions measured for each wavelength in the stimulated experiment with that of a control acquired in the absence of visual stimulation (see results section). Since the regression analysis calculates each T for the different stimuli based on the specific timing of the spectrally-distinct flashes used in the experiment, we submitted the control recording to the same analysis but producing all possible permutations of the T values measured, given that no specific color sequence would be preferable to any other. Thus, the control distribution has been made symmetric in all 4-wavelength dimensions. The presence of a subset of spectrally-distinct responsive neurons outside the false positive neurons derived from the control distribution allows setting a threshold and calculating the corresponding FDR as:

$$FDR(T_{th}) = \int_{T_{th}}^{+\infty} \frac{P_{CTR}(T)\,dT}{P_{EXP}(T)\,dT}$$

We selected T_{Th} values for each stimulus so that FDR = 0.01.

In addition to the T threshold, we implemented a peak analysis in order to select only those neurons responsive above the T threshold whose response is peaked at each stimulus repetition (i.e. 3 peaks for each stimulus). For this analysis we used Matlab *findpeaks* with a minimum prominence of 0.3 and applied it to the $\Delta F/F_0$ traces renormalizing each to its maximum level. As illustrated in detail in result section, peak analysis together with T score analysis provides a very strong selection of stimulated against spontaneous activity.

3.6 Barcode for identification of multiple stimuli responses

For the identification of the neurons responsive to multiple stimuli, a "T barcode" has been implemented. In the text this parameter will be termed

"Tbar". At first, the T threshold specific for each of the four stimuli and peak analysis (see paragraph above) were applied to all data. The Tbar was then calculated for the selected neurons as follow:
$Tbar = 8*L_1 + 4*L_2 + 2*L_3 + 1*L_4$
where L_1, L_2, L_3 and L_4 indicate the responses to the four stimuli, taking value of 1 if the neuron has a T value above the threshold for that stimulus and 0 otherwise.
In this way each responsive neuron takes one of 15 possible values, indicating its unique response to one stimulus or to a specific combination of stimuli.

3.7 Image registration

Two-photon calcium imaging data (Figure 25A) have been registered with a zebrafish reference brain (a 6 dpf Tg(elavl3:GCaMP5G) zebrafish larva, Figure 25B) following the registration procedure described in Randlett et al. [137]. For each sample MIPs z-stacks were produced, oriented and scaled as the template brain (a 276 µm stack sampled with 2 µm z-step) and finally converted to 16-bit nrrd format. The reference brain was oriented dorso-ventrally to match our data thus facilitating the registration procedure. Nonrigid image registration was performed using the software CMTK (Computational Morphometry Toolkit, https://www.nitrc.org/projects/cmtk) and the munger wrapper for CMTK with the following command string: -a -w -r 01 -X52 -C8 -G80 -R3 -A "--accuracy 0.4" -W "--accuracy 1.6" -s “template/templatename_01.nrrd” “images” [137-139].
Where the munger command line options mean:
-a run affine transform
-w run warp transform
-r run reformat on these channel (we work on a single channel so we use 01)
-X [exploration]
-C [coarsest]
-G [grid-spacing]
-R [refine]
-A [options] additional options for affine transformation
-W [options] additional options for warp transformation

-s reference brain
"images" directory containing the image stacks to be registered
Figure 25C shows an example of our data after the registration procedure. Anatomical localization of responsive neurons has been obtained reformatting the cell label z-stacks (mapped throughout the brain volume of each sample and progressively numbered) by applying the transformation parameters obtained from the registration (Figure 25D). The cell label stacks were produced by a script written in Matlab which enumerates, for each plane, all segmented neurons. To apply a progressive numeration across the volumes sampled (about 60 planes with 5 µm z-step) we implemented a custom script written in Matlab and saved the resulting stacks into a 32bit nrrd format file since the total number of neurons identified in the imaging volume exceeds the 16bit number range (i.e. 65536). CMTK reformatx has been performed on 32bit cell label z-stacks (scaled as the template) using the partial volume interpolation options (--pv) with the following command string:
reformatx --pv –o reformattedimage.nrrd --floating [floating image] [template image] [transformation parameters file]
We next localized and quantified the responsive neurons (i.e. neurons responding to one stimulus and to all possible combinations of stimuli, Figure 25D colored dots) across the different brain regions using the available file "MaskDatabase.mat" containing all regional brain mask definitions and outlines [137].

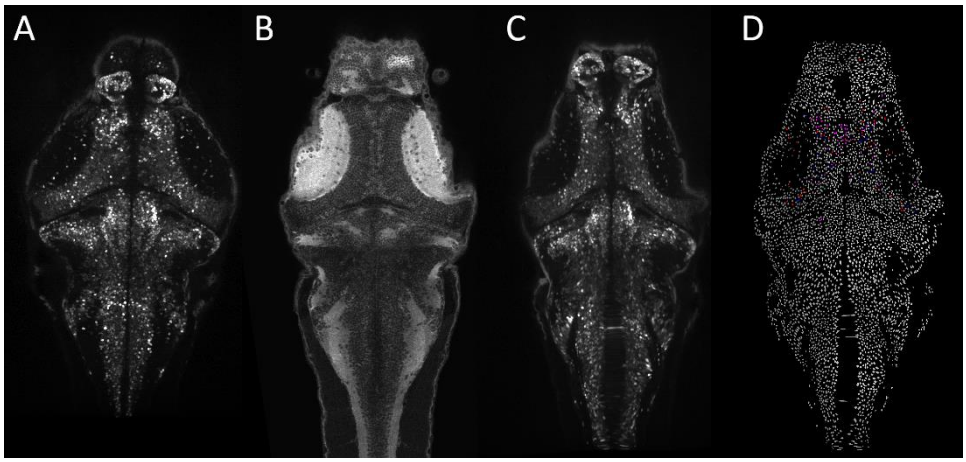

Figure 25. Registration procedure.

(A) H2B-GCaMP maximum intensity projection of a plane recorded in our measurements used as floating image in the registration procedure. **(B)** Reference brain of the same plane

shown in A used as template. **(C)** The same as A after registration onto B. **(D)** Cell label of the same plane shown in C obtained by applying CMTK reformatx using the transformation parameter calculated to obtain C. In the figure are highlighted, with the color-code employed throughout the text (L_1-magenta, L_2-green, L_3-blue, L_4-red), responsive neurons (colored dots) passing threshold and peak analysis selection criterion for each stimulus in the plane shown.

3.8 Selection of stimulus intensity

To verify if spectral responses are affected by the stimulus intensities, we performed some acquisitions by setting each LED to the following intensities: 1 mW/cm^2, 0.5 mW/cm^2, 0.1 mW/cm^2. LEDs voltage was controlled in NI-MAX in order to set the same intensities for the four stimuli. Acquisitions have been performed on 20 planes sampled with 10 µm z-step and, for each plane, the recording has been repeated three consecutive times changing, at each repetition, the LED power. Imaging and visual stimulation have been performed as described above. By analyzing the data, we decided to set the power of each LED at 1 mW/cm^2 since we aimed at performing our measurements in a condition of saturation. Indeed, we compared the T distributions obtained at each power for the different stimuli with the control distribution (Figure 26).

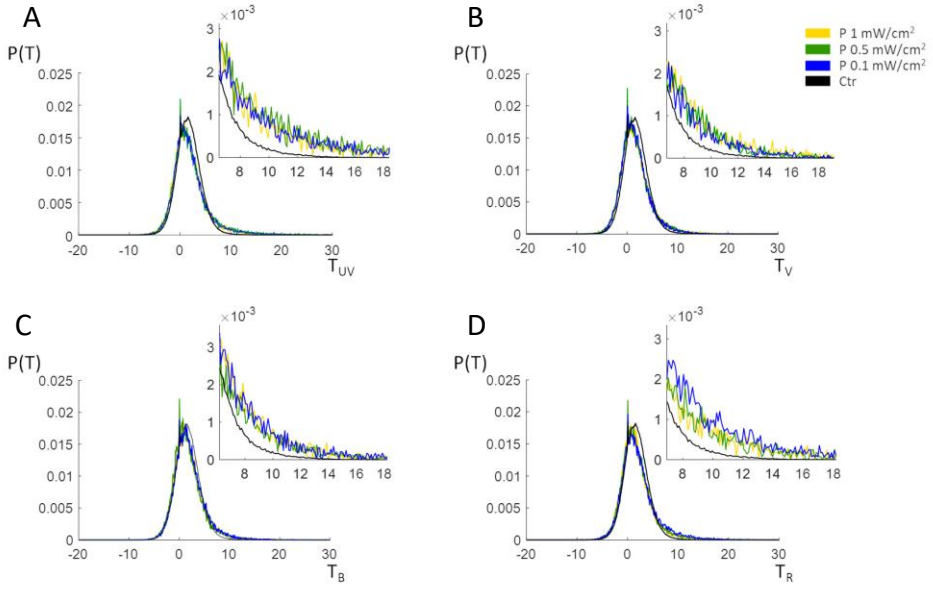

Figure 26. T distributions at different stimulus intensities for stimulated and control larvae at 5 dpf.

Normalized T distributions obtained at three different stimulus intensities (1 mW/cm^2, 0.5 mW/cm^2, 0.1 mW/cm^2, yellow, green and blue traces, respectively; see legend) compared with control (black trace). T distributions are reported for each stimulus (**A**, L_1; **B**, L_2; **C**, L_3; **D**, L_4). The insets on the left are enlarged views of the graphs.

These data show that all responses but the one to L_4 exhibit saturation already at 0.1 mW/cm^2, while L_4 reaches saturation at 0.5-1 mW/cm^2. We, therefore, decided to set stimulus intensity at 1 mW/cm^2 for all LEDs.

3.9 Protocol for testing history-dependence

To assess the spectral identity of the responsive neurons and test for possible history-dependence effects, we recorded neuronal activity by applying two different protocols of visual stimulation: the standard protocol with light flashes in the order L_1, L_2, L_3, L_4 presented in triplicate (Figure 21D); and a shuffled pattern L_3, L_4, L_2, L_1, L_4, L_3, L_1, L_2, L_2, L_3, L_4, L_1. We imaged each plane twice presenting the two protocols of visual stimulation and waiting 120 s between the two consecutive acquisitions. We recorded about ten planes sampled with 20 µm z-step for 176 s during visual stimulation (see paragraph 3.3 for a detailed description of sample mounting procedure, acquisition parameters and LEDs used for visual stimulation). Although the waiting time between the two consecutive acquisition of the same plane is quite short, we observed a slight drift between the two acquired planes (Figure 27A, C show the overlay between the two planes). In order to analyze spectral identity on the same exact cluster of pixels in the sample, we corrected for xy drift by applying image registration procedure between each pair. In details, for each recording (standard and shuffled protocol of visual stimulation) we produced a MIP z-stack which we oriented and scaled following the registration procedure described in the paragraph above. In this case we registered the stack acquired with the standard protocol onto that one acquired with the shuffled pattern (used as template) by using the software CMTK and the munger wrapper for CMTK with the same parameters described above. Figure 27B, D show an overlay of two planes after registration. We then interleaved the

two stacks and, for each recorded pair of planes, we produced a MIP (i.e. a sort of sum between the two planes) allowing us to obtain a unique image with the same position and number of neurons. The resulting MIP was used for the subsequent analysis. At first we applied the segmentation analysis (see paragraph above) to work on single cells. The same Matlab scripts employed for automatic neuron segmentation provided the cell label stacks by applying a progressive neuron numeration across the volumes sampled. On the resulting stacks linear regression analysis has been applied for the identification of the responsive neurons. However, since in the registration procedure we used as template the recordings with the shuffled pattern of stimulation, we proceeded reformatting the cell label stacks using CMTK *reformatx* before analyzing the planes acquired with the standard protocol of stimulation. We employed CMTK *reformatx* using the partial volume interpolation options (--pv) and the inverse transformation (-i) with the following command string:

reformatx --pv –o reformattedimage.nrrd --floating [floating image] [template image] -i [transformation parameters file]

Where transformation parameters file has the parameters obtained by the registration procedure. In this way, it was possible to compare the spectral responses deriving from the two visual stimulation protocols on the same cells to verify neurons spectral identity independently of the order of the stimuli presentation.

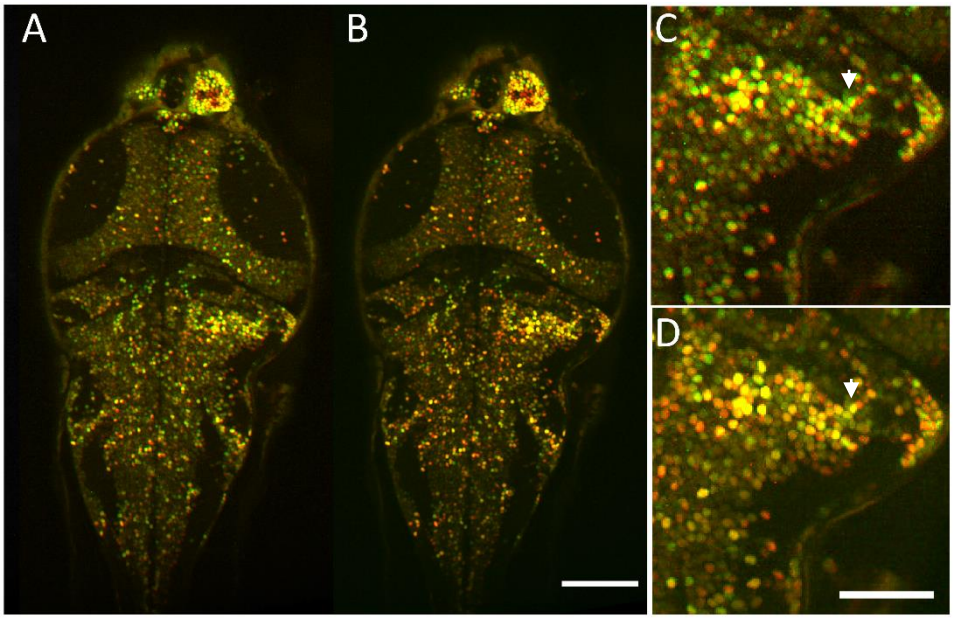

Figure 27. xy drift correction.

(A) GCaMP fluorescence maximum intensity projection of a plane of a 5dpf larva recorded with the standard protocol of visual stimulation (green channel) and the same plane imaged during stimulation with a randomized order of the stimuli (red channel). Overlap between neurons is shown in yellow. **(B)** The same as A after registration of the plane recorded with the standard pattern of visual stimuli (green channel). Scale bar: 100 µm. **(C)** Magnified view of A. The inset highlights a slight shift between the two images as shown by some neurons not perfectly overlapped (one example is indicated by the white arrow) and better visible at the edge of the sample. **(D)** Enlarged view of B. After the registration the two images overlap perfectly and it is possible to appreciate a high degree of overlap between neurons compared to E (the white arrow in the panel shows the same neuron indicated in C after registration). Scale bar: 50 µm.

3.10 Two-photon temporary perturbation and optical highlighting

Imaging was performed with a custom-built two-photon microscope equipped with a tunable Ti:Sa laser (*Chameleon Ultra II*, Coherent, Santa Clara, California, USA, λ_{ex} 920 nm) and a 20x/0.95 NA water immersion objective (Olympus, Tokyo, Japan) mounted on a piezoelectric motor (N-725, Physik Instrumente, Karlsruhe, Germany). The raster scanning was

obtained by a couple of galvanometric mirrors. The same laser used for two-photon imaging has been employed for the temporary perturbation procedure (more details in result section) consisting of a line-scan on a selected neuron membrane (i.e. OT neurons responsive to visual stimuli, and Rohon-Beard (RB) spinal cord neurons) using appropriate irradiation parameters (14 mW/μm^2) yielding to a reversible damage. In these experiments we employed 5 dpf Tg(elavl3:GCaMP6s) zebrafish larvae with pan-neuronal expression of the cytoplasmic-localized calcium indicator GCaMP6s (ZFIN line *fi1Tg* [140]) on homozygote albino background. The mounting procedure has been described above. For visual stimulation we employed a 590 nm red LED (M590L3, Thorlabs, Dachau, Germany) equipped with a band-pass filter (FF01-600/14, Semrock, Rohnert Park, California, USA) for selective L cone excitation mounted directly on the stage of the microscope (M687, Physik Instrumente, Karlsruhe, Germany). The visual stimulus (100 ms red flashes) was presented to the larva frontally in a sequence of five regularly paced flashes (9.36 s apart from each other, Figure 28A). The LED power was measured and adjusted to 1 mW/cm^2. We chose as target for temporary perturbation OT neurons and performed imaging with a FOV of 223x223 μm^2 and a resolution of 0.58 µm/px. Working on the same plane, in order to avoid z-shift or change of position during subsequent acquisitions, a sample repositioning routine has been implemented directly on the acquisition program: a z-stack was acquired with a 20 µm total excursion (0.5 µm z-step) above and below the selected focal plane and a subsequent correlation of z-stack planes with the MIP of the reference plane produced the xyz stage displacements necessary to maximize correlation. Each scan of the FOV required 780 ms. The complete set of stimuli and fluorescence imaging on each plane required 62.4 s (i.e. 80 frames). The acquisition program was controlled by a software written in LabView. We utilized the same software to control visual stimuli and to synchronize them with the imaging acquisition. Regarding spinal cord irradiation, imaging has been performed with a FOV of 225x225 μm^2 and a resolution of 0.44 µm/px. Changing the irradiation parameters (20 mW/μm^2), the same technique and zebrafish transgenic line have also been employed to induce an irreversible activation limited to targeted OT neurons with the attempt to highlight and reconstruct the projection of selected cells in the OT neuropil. Imaging was performed on a selected OT plane with a FOV of 133x133 μm^2 and a

resolution of 0.26 μm/px for 780 ms during visual stimulation with two red flashes (100 ms duration; 9.6 s apart each other), choosing as target for optical highlighting those neurons responsive to both flashes. All the experiments were performed at room temperature.

3.11 Pixel-based linear regression analysis

For the identification of responsive tectal neurons targeted for temporary irradiation, we employed a Matlab script based, with modifications, on the method described by Miri et al. [136]. We performed the same method described above with some modifications. Briefly, using a convolution of the stimulus light pulses with the GCaMP calcium impulse response function (modelled, in our system, with an exponential rise with rise time of 1.5 s and an exponential decay with decay time of 2.1 s), we obtained a regressor (G; Figure 28B) for the calculation of the regression coefficient β and the relative T-score values (as described above). However, in this case, due to the employment of the cytoplasmic-localized calcium indicator, we did not work directly on single cells (since we did not apply the segmentation analysis used for the nuclear-localized calcium indicator) and the analysis was carried at pixel level, yielding a T-map that assigned to each pixel a specific T value, as shown in Figure 28C. The false color map (with the scale shown in Figure 28C) thus quantifies the level of responsiveness to the visual stimuli (based on the T-score values), highlighting some neurons and process in the neuropil.

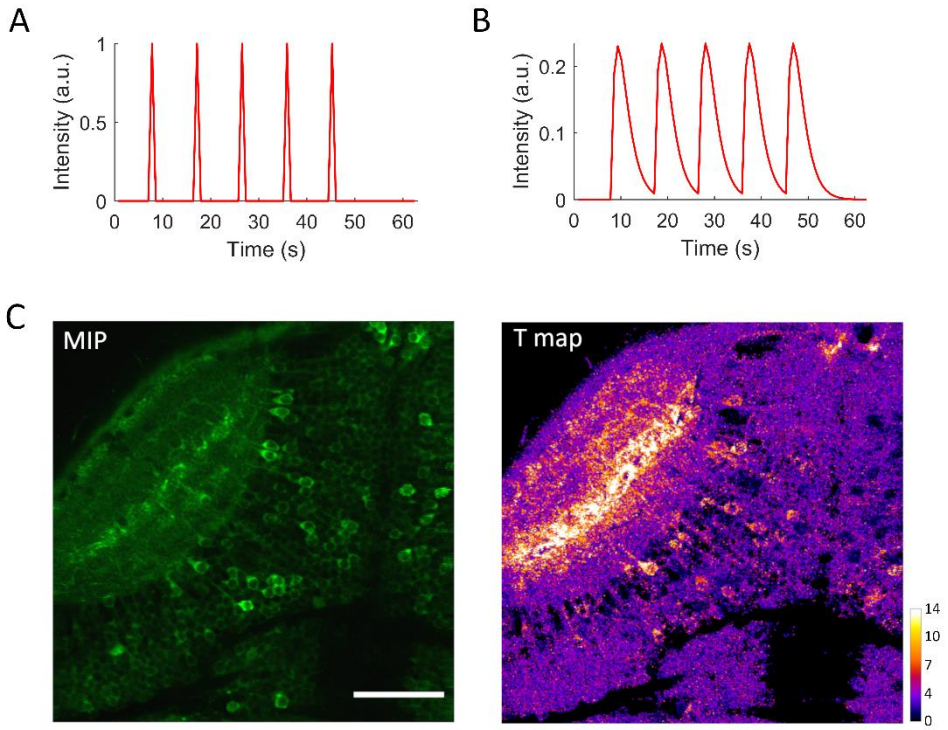

Figure 28. Pixel-based regression analysis.

(A) Protocol of visual stimulation consisting of five red flashes presented every 9.36 s. **(B)** Visual stimuli normalized regressor vector obtained by convolution of the time-dependent sequence of stimuli with the calcium impulse response function. **(C)** Left panel: GCaMP6s fluorescence maximum intensity projection (MIP) of an optic tectum plane of a 4dpf larva. Scale bar: 50 µm. Right panel: corresponding T score map obtained by applying a pixel-wise linear regression analysis. The brighter pixel clusters indicate the response to the visual stimulus as highlighted by the false color map in the figure.

4. RESULTS

4.1 Whole-brain imaging during visual stimulation

In this work, two-photon microscopy was used to image the whole brain and part of the spinal cord of elavl3:H2B-GCaMP6s transgenic larvae expressing, at pan-neuronal level, the genetically-encoded calcium indicator GCaMP6s (Figure 21A). Larvae were embedded in agarose (see sample mounting procedure) for immobilization under the microscope objective. We recorded neuronal activity during visual stimulation performed with light flashes emitted by four LEDs (Figure 21D) at wavelengths matching the absorption peaks of the four zebrafish retina cone types (Figure 21C). The four LEDs were mounted on the microscope so that the direction of stimulus presentation produced stimulation of mainly the dorsal-frontal area of the visual field (i.e. the *area temporalis* of the retina). Although we narrowed the emission bandwidth of each stimulus to less than 35 nm, the cone absorption spectra themselves are broad enough to determine an amount of insuppressible cross-talk, with the only exception of L cones for λ>590 nm (Figure 21C). Given the wavelength bandwidths of our stimuli (Figure 21C), we estimated for each LED the following relative excitation coefficients: L_1 1/0.54/0.04/0 for UV/S/M/L cones, respectively; L_2 0/1/0.37/0; L_3 0/0.14/1/0.22; L_4 0/0/0/1. For simplicity and adopting a terminology related to human perception which will make some descriptions more intuitive, in some instances we will refer to L_1, L_2, L_3 and L_4 stimuli also as UV, violet, blue and red, representing the corresponding data in the figures with magenta, green, blue and red, respectively. It should be noted here that the perception of color is a very complex process, implying even a degree of subjectiveness, so that we introduce the terms "color" and the use of colors experienced in our daily life after stressing that in this work uniform flashes were used (whereas much of the actual perception of colors derives indeed from the processing of information on contrast between adjacent areas of the visual field, edges and so on). Thus, the term "color" will be applied to discussing our findings for zebrafish larvae when it applies to what we believe is related to the larva perception of the world and thus involved in eliciting "color"-sensitive behaviors. We recorded neuronal activity in 3 and 5 dpf larvae (N = 7 each) during visual stimulation with 100 ms light flashes characterized by the spectra shown in Figure 21C and presented in the order L_1, L_2, L_3, L_4 in

triplicate Figure 21D. The power of each LED was set to 1 mW/cm^2 (see methods), which produced saturation of the measured responses (Figure 26). Three-dimensional mosaic two-photon fluorescence acquisition covered a volume of 1500x720x270 μm^3 (with z-steps of 5 µm), encompassing the whole encephalon and about one quarter of the spinal cord of the larva (corresponding to about eight segments). Cellular resolution of imaging and automatic segmentation (Figure 23) allowed us to extract GCaMP6s fluorescence and $\Delta F/F_0$ traces for each segmented neuron, so that measurements were analyzed directly at single-cell level (Figure 23). Each neuron (with a nucleus having ~5 µm of diameter) is imaged as a cluster of pixels with different fluorescent intensity levels based on its activity. The magnified view of a single neuron shown in Figure 23E (top panel) displays, in grey-scale, the fluorescence intensity associated with each pixel. Segmentation analysis thus produces, for each recorded plane, an image that is an overlay between the segmented neurons and the corresponding fluorescence maximum intensity projection. To match neurons diameter, each cell is segmented as a cluster of 13 pixels (highlighted with an arbitrary color; see Figure 23B, D) arranged in a precise star-like pattern (Figure 23E, bottom panel). The Matlab script employed for automatic neuron segmentation has been modified in order to consider tightly packed neurons as distinct (and so attributing to each of them different and non-overlapping pixel-clusters). We identified about 100000 (5 dpf) and 90000 (3 dpf) neurons in the encephalon of each larva, and about 10000 (5 dpf) and 3700 (3 dpf) in the part of spinal cord investigated. Figure 29 shows an example of six planes sampled in our volumetric recordings (which consisted typically of 54 planes along the z-axis for the encephalon) in one larva at 5 dpf.

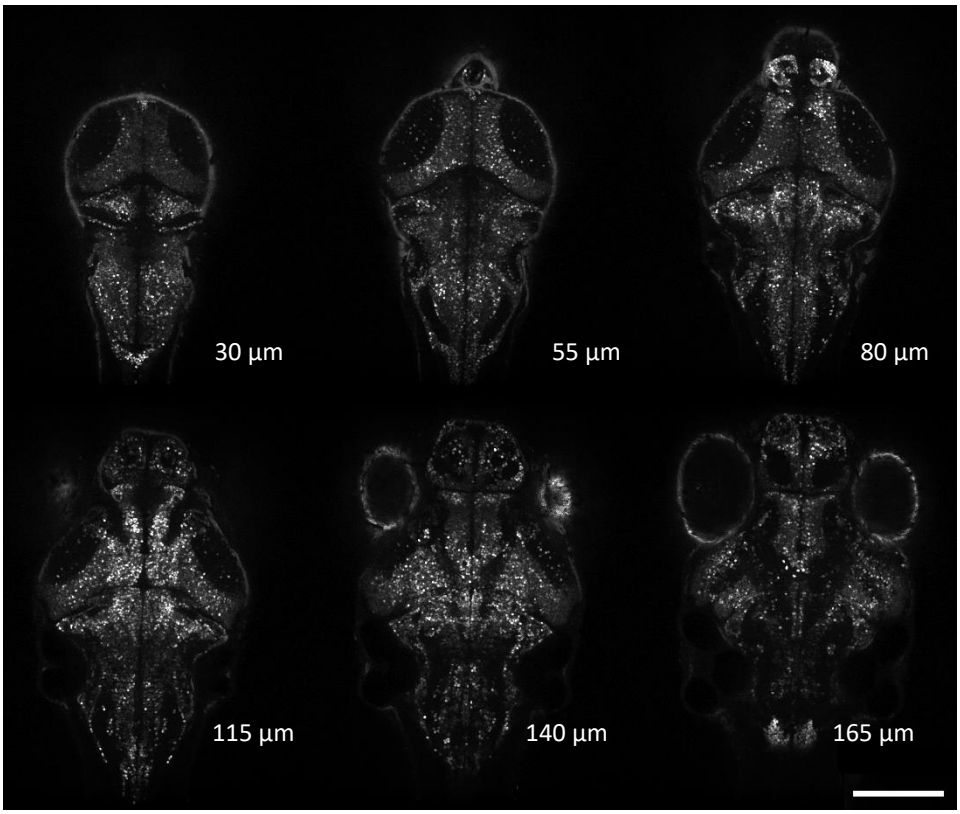

Figure 29. Volumetric imaging during visual stimulation.

H2B-GcaMP6s fluorescence maximum intensity projections of a 5 dpf larva during visual stimulation. The panel shows six planes at different depths (indicated in figure), each plane was sampled for 176 s during stimulation with the four spectral stimuli. Scale bar: 200 µm.

Figure 30A shows one plane of the encephalon of a 5 dpf larva with the selection of eight exemplary neurons. Figure 30B shows images of the respective ROIs during 176 s of recording. The ROIs intensities highlight spikes of activity (visible as an increase of fluorescence) associated with the responses triggered by the four stimuli, with variable responses from cell to cell. The trend of each response is better visible in the $\Delta F/F_0$ time traces shown in Figure 30C where, indeed, a wide-array of responses can be observed. The figure shows some representative responses we found in our data, including responses to one or multiple stimuli. Observation of the $\Delta F/F_0$ traces (Figure 30C) points out a certain level of variability both regarding their peak amplitudes and the presence of spontaneous activity

spikes. Despite some variability in amplitude of such responses (for example in panels 2,3 and 4), we can observe three peaks of activity that can be attributed to the three repetitions of the visual stimuli. However, some times, in addition to the activity patterns related to the visual stimulation, it is possible to observe also some spikes of spontaneous activity, visible for example in panel 2 or in panel 6. Even when occurring at the time of a visual stimulus, we cannot consider these sporadic peaks as associated with visual stimulation, since they do not occur at each stimulus repetition. Based on the complexity of responses in our data, a reliable and robust quantitative analysis method is needed to ensure selecting only responses elicited by the visual stimuli and avoiding possible spontaneous activity events. For this aim, we introduced in our analysis control experiments acquired in absence of visual stimulation (i.e. providing an extensive sampling of spontaneous activity) and compared them with the stimulated data, in order to evaluate the impact of spontaneous activity on the identification of visually-evoked responses.

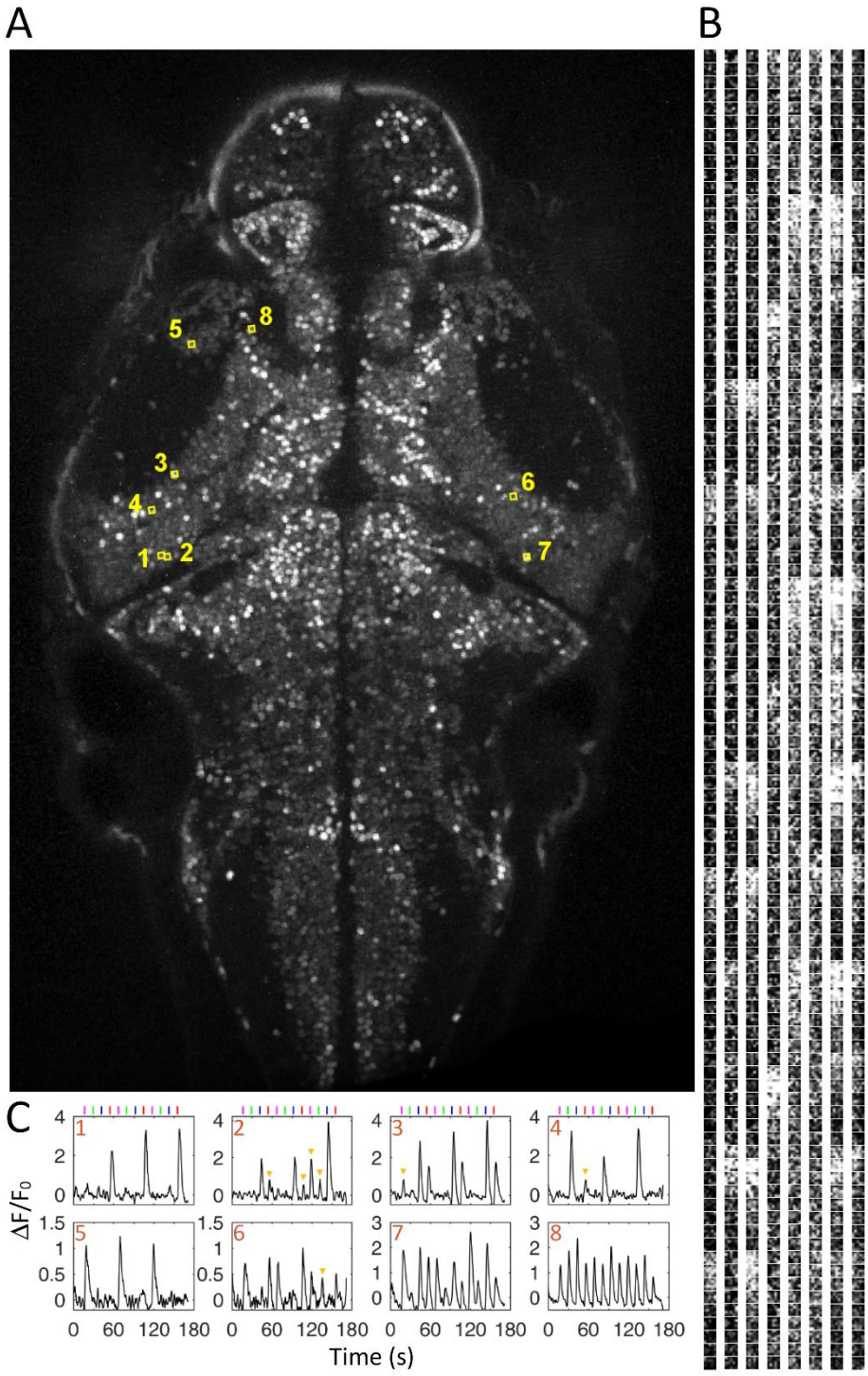
A
B
C
5
8
3
6
4
1
2
7
ΔF/F0
Time (s)
0 60 120 180

Figure 30. GCaMP6s functional imaging during visual stimulation.

(A) GCaMP fluorescence maximum intensity projection of one plane of a 5 dpf larva. FOV 480X740 μm^2. **(B)** Fluorescence time series of the eight neurons highlighted in A (ROIs 1-8 displayed in yellow) sampled every four frames (i.e. every about 1.7 s); the time series are shown vertically. **(C)** $\Delta F/F_0$ traces associated with the eight ROIs highlighted in A and B, showing responses to one stimulus (panels 1, 2, 4, and 5), two stimuli (panel 3 and 6) and multiple stimuli (panels 7 and 8). Stimulus time points are indicated at the top of the panels adopting the following color-codes: L_1-magenta, L_2-green, L_3-blue, L_4-red. The orange arrowheads in panels 2, 3, 4, 6 highlight some random spikes not associated with the pattern of visual stimulation and thus attributable to spontaneous activity.

4.2 Identification of neurons spectral identity

The traces shown in Figure 30 display very clear and spectrally-tuned responses of the selected neurons. We employed linear regression analysis on the $\Delta F/F_0$ traces to systematically and quantitatively measure the responses of all segmented neurons to each of the visual stimuli. As described in detail in the methods, regression analysis produces four T-scores that quantify the strength of response to each of the four stimuli. To assess spectrally-defined responses evoked by the visual stimuli across the CNS and spinal cord, we produced the distributions of the four T-scores for 3 and 5 dpf larvae (N = 7 each), comparing the distributions obtained during visual stimulation with those obtained from controls recorded in the absence of stimuli (N = 5 each). The results are shown in Figure 31; such distributions will be used to distinguish responses evoked by the visual stimuli (true positives) from spontaneous activity present also in the control measurements (false positives). Indeed, the difference between the stimulated and control larvae T distributions shown in Figure 31 highlights the presence of populations of neurons responding to the visual stimuli. Also, the T distributions at 5 dpf display noticeable differences with respect to those at 3 dpf, both quantitatively (a much larger proportion of spectrally-responsive neurons can be observed, with many of them characterized by higher T-scores than those measured at 3 dpf) and qualitatively (at 5 dpf L_1-responsive neurons are predominant followed, in descending order, by L_4, L_3, and L_2; at 3 dpf, on the other hand, L_4 responses are predominant). In addition to neurons with positive T values above the control distribution, a small population is also detected with negative T values (especially for L_1 stimuli), which indicate a negative response to the light flashes, i.e. an inhibitory effect of light on neuronal

activity. It is interesting to evaluate this result in light of the nature of GCaMP signal. These neurons may be characterized by a high basal spiking frequency (associated with a higher basal [Ca^{2+}] and so fluorescence intensity) at low-light level, which drops when light flashes of specific wavelengths are presented. As a consequence, it is possible to presume a spectrally-evoked reduction of spiking frequency (and a consequent decrease of fluorescence intensity) in these neurons, resulting in negative T values. Within this context, the use of GCaMP as Ca^{2+} reporter allows monitoring the neuron activity dynamics not necessarily associated with an increase in intracellular calcium concentration followed by neuron activation, as in the most common view of GCaMP imaging. The differences among the four experimental distributions shown in Figure 31 point at an appreciable degree of spectral identity for the populations of neurons involved (as also highlighted by some examples of unique vs. generalized spectrally-tuned responses shown in Figure 30C). As discussed above, the complexity of neuronal responses requires a quantitative method for identifying responsive neurons, distinguishing stimulus-evoked responses from spontaneous activity and quantifying the spectral specificity of the identified responses. From the distributions shown in Figure 31 we can see that the control data fall to zero at $T \sim 27$, whereas stimulated larvae display a fraction of neurons characterized by $T > 27$. Thus, the total deviation of this part of the distribution from the control data is clearly to be attributed to responses triggered by the visual stimuli.

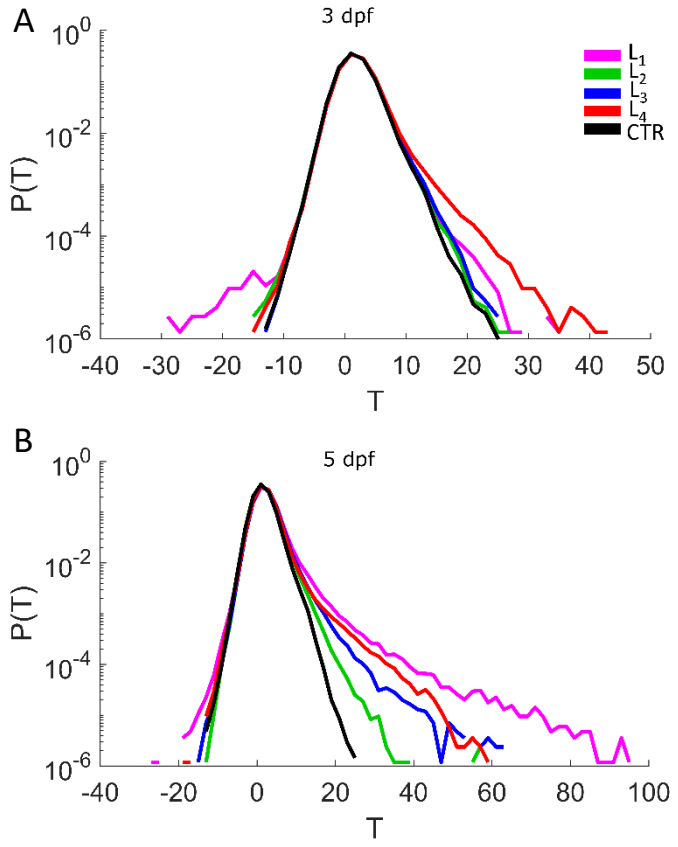

Figure 31. T distributions for stimulated and control larvae at 3 and 5 dpf.

Normalized distributions of T values for L_1, L_2, L_3, L_4 stimulation (magenta, green, blue and red traces, respectively; see legend) and control acquired in the absence of visual stimulation (black trace) measured for 3 dpf larvae **(A)** and 5 dpf larvae **(B)**. N = 7 for stimulated data, N = 5 for control data in both panels. It should be noted, however, that the distributions reported in the figure are cumulated over the total number of ROIs segmented over all larvae for each condition: 847068 (3 dpf stimulated); 588198 (3 dpf control); 845070 (5 dpf stimulated); 518409 (5 dpf control).

Before proceeding to the identification of the responsive neurons, we wanted to assess the robustness of our data analysis method with particular regard to the significance of T-values depending on the proper time-distribution of the regressors. To this end, we measured T distributions by analyzing the data with a shuffled order of the spectral stimuli (Figure 32). We applied the following order of regressors: L_2, L_1, L_4, L_3, L_3, L_4, L_1, L_2, L_4, L_3, L_2, L_1, thus permuting the identity of the stimuli compared to the

order presented in the experimental measurements (L_1, L_2, L_3, L_4, presented in triplicate). For simplicity, we refer to this pattern as "shuffled", while we term the protocol of visual stimulation used in our measurements (Figure 21D) "standard". The distributions clearly show that the data analyzed with the shuffled order fall onto the controls, thus highlighting that the presence of spectrally-defined responses characterized by higher T values is unique of data acquired under visual stimulation and analyzed with the proper order of regressors.

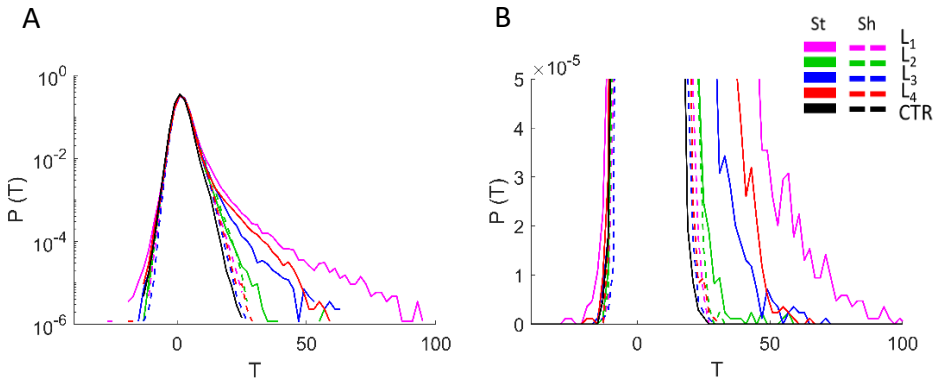

Figure 32. Spectral specificity of T analysis.

Normalized T distributions across 7 larvae at 5 dpf comparing experimental data analyzed with standard order of regressors (solid colored traces, same data as in Figure 31), shuffled pattern of regressors (dotted colored traced), and controls (black trace, same as in Figure 31) data (see legend). T distributions were plotted both in logarithmic scale **(A)** and in linear scale **(B)** to provide a better view in different ranges.

4.3 Spectrally-responsive neurons selection

To spectrally characterize the populations of responsive neurons, we proceeded with the identification of cells reliably responding to the visual stimuli. Following regression analysis, we needed to apply a quantitative method for neurons selection, optimizing the compromise between the false positive neurons of the control data and the positive neurons of the experimental one (Figure 33). Looking at the T distributions shown in

Figure 31, it is possible to observe the presence of a certain degree of overlap between control and stimulated data up to T∼27. This overlap derives from the spontaneous activity that randomly produces spikes temporally coinciding with one of the 12 stimuli used in our pattern of stimulation giving rise to a fraction of false positive neurons. Clearly, the probability of multiple (n) spontaneous peaks coinciding with the times of a given stimulus rapidly decays with n. This property was exploited after T-analysis with a peak analysis (more on this below; see also methods) to improve rejection of false positives. Because of this strong dependence on n, the effects of spontaneous activity on data analysis decrease with the increase of the number of stimuli repetitions. Increasing this number, on the other hand, increases the time required for the measurements. The choice of a stimulation pattern consisting of three repetitions of the four spectrally-distinct stimuli represents a good compromise between the robustness of regression/peak analysis and the duration of the whole experimental recording. One factor determining the duration of the recording is the duration of the responses to the visual stimuli: we observed that the responses of the activated neurons consisted of florescence spikes completely returning to the baseline 12 s after the stimulus. This response dynamics (much longer than the 100 ms stimulus duration) is a convolution of the neuronal activity itself with the GCaMP6s indicator dynamics (τ_{ON} 180 ms and τ_{Off} 550 ms, [114]); so, we decided to distance the stimuli 12.5 s from each other. Given the slow responses observed, the 0.4 s temporal resolution of our imaging allowed us to resolve the activity evoked by visual stimuli very well. Although sampling one repetition of the four spectrally-distinct stimuli would require only 50 s per plane, a single stimulus repetition does not ensure a reliable discrimination between stimulated responses and spontaneous activity, since one peak of activity may be related to either. As a consequence, it would be very hard to separate the false positives of the control data from the true positives of the experimental ones. Thus, we decided to perform a set of three stimulus repetitions to ensure a reliable regression analysis and discrimination between false and true positives. In this way the complete stimulus presentation protocol and fluorescence imaging lasts 176 s per plane. Since we recorded about 54 and 25 planes for the encephalon and spinal cord, respectively, the total volumetric acquisition requires 3h 40 min for each larva. We observed that this is the best compromise to guarantee sample viability and d-tubocurarine effect allowing also a good discrimination between experimental and control T distributions. Clearly, a higher number of stimulus repetitions would guarantee a larger separation between the

experimental and control distributions but, at the same time, the whole experimental recording would require a much longer time. Indeed, we observed that imaging the same plane for longer times led to sample damage (visible as an increase of fluorescence of the total scanned area, more on this in paragraph 4.10) and also to a decay of d-tubocurarine effect, resulting in movement artefacts. All these observations led us to choose a set of three stimulus repetitions as the best compromise. The selection of neurons significantly responding to the stimuli is based on T thresholds (T_{Th}) determined by quantitative comparison of experimental and control T distributions and calculation of false discovery rate (FDR) as described in materials and methods and illustrated in Figure 33.

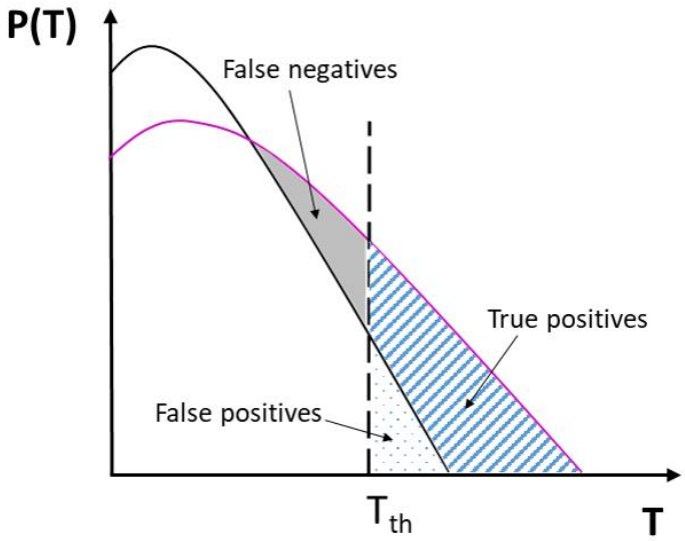

Figure 33. Schematic representation of T-distributions and the effects of threshold selection.

The figure illustrates a schematic representation of stimulated (magenta curve) and control (black curve) T distributions and the effects deriving from T threshold (T_{Th}) selection. The choice of a T_{Th} unavoidably includes in the selection a fraction of false positive neurons (blue dotted area in the figure) together with the true positives neurons of the stimulated data (blue striped area in the figure). On the other hand, the T_{Th} leaves out a fraction of responsive neurons above control, classified as false negatives (grey area).

Although imposing a value of T_{Th} as high as 27 would ensure a zero FDR, at the same time it would lead to missing a significant fraction of actually

responsive neurons (giving rise to a large proportion of false negatives), since deviation of the experimental distributions from control is evident in Figure 31 starting at T∼10. Thus, for $10<T_{Th}<27$ a compromise has to be reached between false positives and false negatives. We base our considerations on the false discovery rate, since false positives are more detrimental to our analysis than false negatives. Thus, we chose to set the FDR at 1%, ensuring that subsequent analysis selects positive neurons with 99% confidence. We defined the parameter $T_{4D} = \sqrt{T_U^2 + T_V^2 + T_B^2 + T_R^2}$ (where T_U, T_V, T_B and T_R indicate L_1, L_2, L_3 and L_4 stimuli, respectively) which quantifies neuron activity triggered by the stimuli but without spectral selection. Figure 34 shows T_{4D} distribution for N = 7 larvae at 5 dpf compared with the same distribution obtained from controls (N = 5 larvae at 5 dpf). From these data it is possible to observe that the T_{4D} distribution of the stimulated larvae (yellow trace in the figure) significantly deviates from the control one (black trace) which falls to zero at T∼27 whereas the experimental distribution assumed higher T_{4D} values up to ∼100.

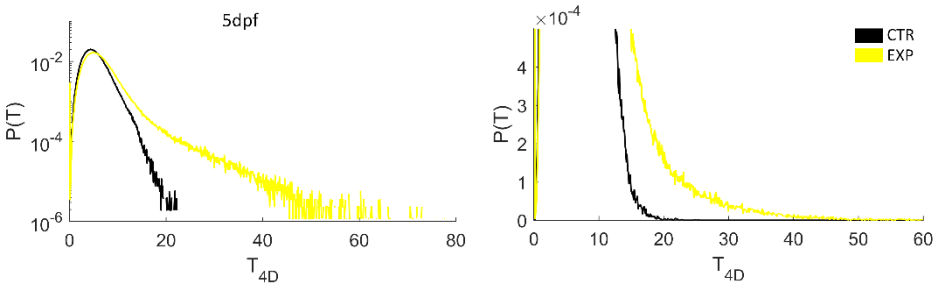

Figure 34. T_{4D} distributions for stimulated and control larvae at 5 dpf.

The figure shows a comparison of T_{4D} normalized distributions between experimental (yellow trace, N = 7 larvae) and control (black trace, N = 5 larvae) data. T distributions are shown both in logarithmic (left panel) and linear scale (right panel) to provide a better view in different range. The statistics reported in the figure are reported in Figure 31.

Figure 35 shows the use of T distributions in control and stimulated larvae for the calculation of FDR vs. T. From these data we can select a threshold (T_{Th}) ensuring FDR=1%. The panels of the figure show the calculations of

thresholds performed on T_{4D} and on each individual spectral stimulus, demonstrating the selection of a T_{Th4D} = 18.5, T_{ThU}= 17, T_{ThV}= 24.7, T_{ThB}= 20.8, T_{ThR}= 18.1. The different values of T threshold associated to each stimulus depend on the robustness of the responses elicited by the different wavelengths used in our measurements. Looking at the T distributions in Figure 31B it emerges that L_1 stimulus evokes stronger responses (both in term of number of responsive neurons and values of T) compared to the others, as demonstrated by the high T values reaching about 100 (magenta curve in the figure), followed by L_4 and L_3. In contrast, neuronal responses associated with L_2 stimulus (green curve) are the weakest with T values around 40 and clearly a lower number of responsive neurons. It is also important to take into consideration the direction of presentation of our stimuli, mainly stimulating the *area temporalis* of the retina, which is particularly rich in UV cones (more on this in the discussion section), thus contributing to the robust responses evoked by L_1 stimuli we can observe in Figure 31B. The very stringent criterion adopted for FDR unavoidably lead to miss some responsive neurons (i.e. gives rise to false negatives; see also schematic representation in Figure 33), especially those responsive to the L_2 stimulus whose T_{Th} is the highest compared to that of the other stimuli. However, we decided to ensure FDR 1% in order to select true positive neurons (avoiding the risk of including in our data a larger proportion of false positives due to spontaneous activity) with 99% confidence aware that only a fraction of all spectrally-responsive neurons actually pass the threshold selection criterion.

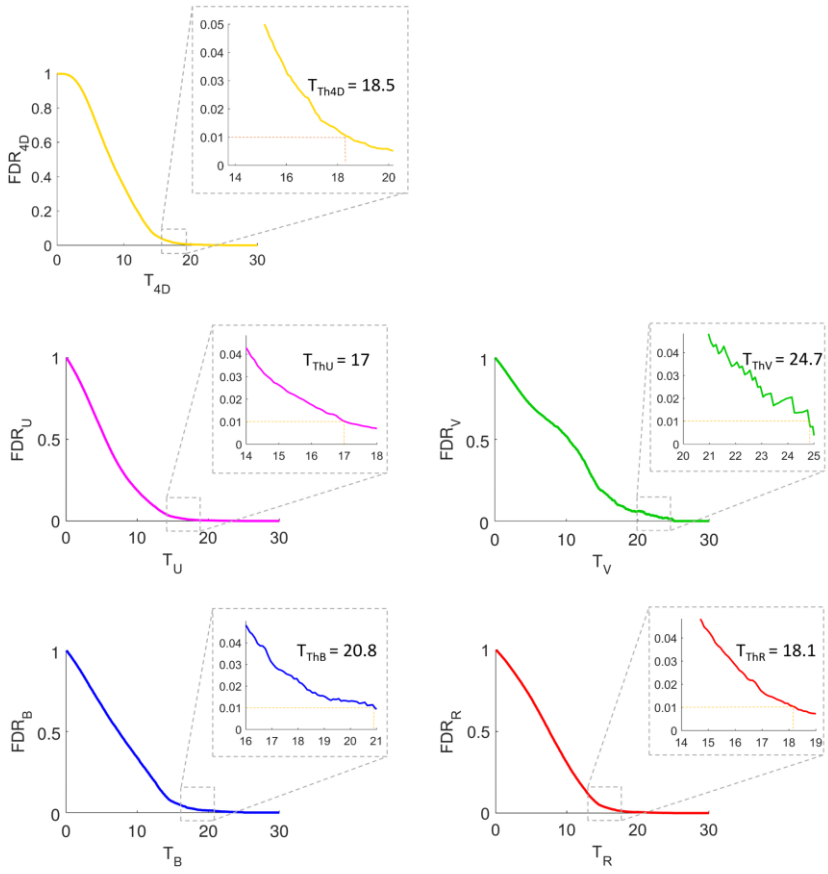

Figure 35. Choice of threshold for neuron selection.

Plots of FDR vs T_{Th}. Top panel: plot of False Discovery Rate (FDR) used to choose a T_{4D} threshold (T_{Th4D}) to automatically select neurons responsive to any of the stimuli we presented in our experiments with a confidence of 99%. The same criterion has been applied to choose T thresholds named T_{ThU}, T_{ThV}, T_{ThB}, T_{ThR}, for the selection of L_1, L_2, L_3 and L_4 responsive neurons, respectively, always ensuring FDR=0.01. T thresholds values are shown in the insets and applied to all subsequent analysis.

Although regression analysis is a robust method for responsive neurons selection, we had to overcome some issues we observed. Regression analysis is based on the calculation of the correlation coefficients (β) between the neuron fluorescence signal ($\Delta F/F_0$) and the pattern of 12 stimuli used for visual stimulation, represented by the regressors shown in Figure 24C. T analysis employs these coefficients introducing the calculation of the residuals ε (i.e. higher ε values lead to a reduction of T values) thus increasing the robustness of regression analysis (compared to the conventional correlation analysis). However, the main limitation of this method derives from its dependence on the amplitudes of the responses; we can illustrate this concept with an extreme example: a neuron responding to all stimulus repetitions (i.e. three peaks, which is a response that can be confidently attributed to the visual stimuli) with amplitude 1 (arbitrary units) for each peak will have the same β of a neuron displaying only one peak with amplitude 3 in one of the positions expected for the stimuli. This situation can arise from spontaneous activity where large peaks can be observed, and it is particularly insidious when analyzing activity in areas of the CNS involved in periodic spontaneous (or at least non visually-induced) motor events. Even though the former case is characterized by lower ε than the latter (due to its better adherence to the three-peak shape of the regressor) similar values of T can derive from these different scenarios. In this way, neurons responding with only one peak could display a high T value and pass the threshold selection criterion. Even though the numerical consistency of these false positives is restricted within the 1% limit we set for FDR, we wanted to also take advantage of peak analysis to further reduce the effective FDR. In fact, spontaneous activity could represent a real problem in our measurements since single peak responses may be linked to neuronal activity depending on motor-related artifacts (especially in relation to the most caudal regions more prone to motor events) and not directly associated to our visual stimuli. Although our choice of thresholds is very conservative (setting FDR to 1%) and thus generally provides great confidence in the selection of responsive neurons, we considered that it is based on all neurons from all areas, and so we wanted to provide further strength to the analysis even when moving out of the most densely responsive areas like mesencephalon. Based on these considerations, we implemented a peak selection criterion to ensure (and so select for subsequent analysis) spectral responses peaked during each stimulus repetition. We thus introduced peak analysis (see methods) in addition to the threshold selection that allowed us to select neurons above a specific T_{Th} and consistently responsive to all three stimulus repetitions

so to avoid including in our data possible spontaneous motor events (a quantitative assessment of such analysis is shown below). Figure 36 shows some representative examples to clarify this aspect pointing out the robustness of peak analysis in leaving spikes of spontaneous activity out from our data even if, as mentioned above, they would pass T threshold selection criterion. In other cases, as exemplified in Figure 36G, we observe peaks of activity starting before the stimulus presentation (the second peak in correspondence of L_4 stimulus and the low-amplitude response peaked at L_2 stimulus in the example shown) so clearly not evoked by the stimulus itself but rather due to spontaneous activity. These responses partly coincide with the shape of the regressors so that they contribute spurious effects to T calculation. In this panel also emerges another random lower amplitude peak, thus highlighting the random nature of spontaneous activity spikes which undoubtedly are not evoked by visual stimuli. The figure demonstrates that peak analysis overcomes these problems by discarding the largest majority of spontaneous activity.

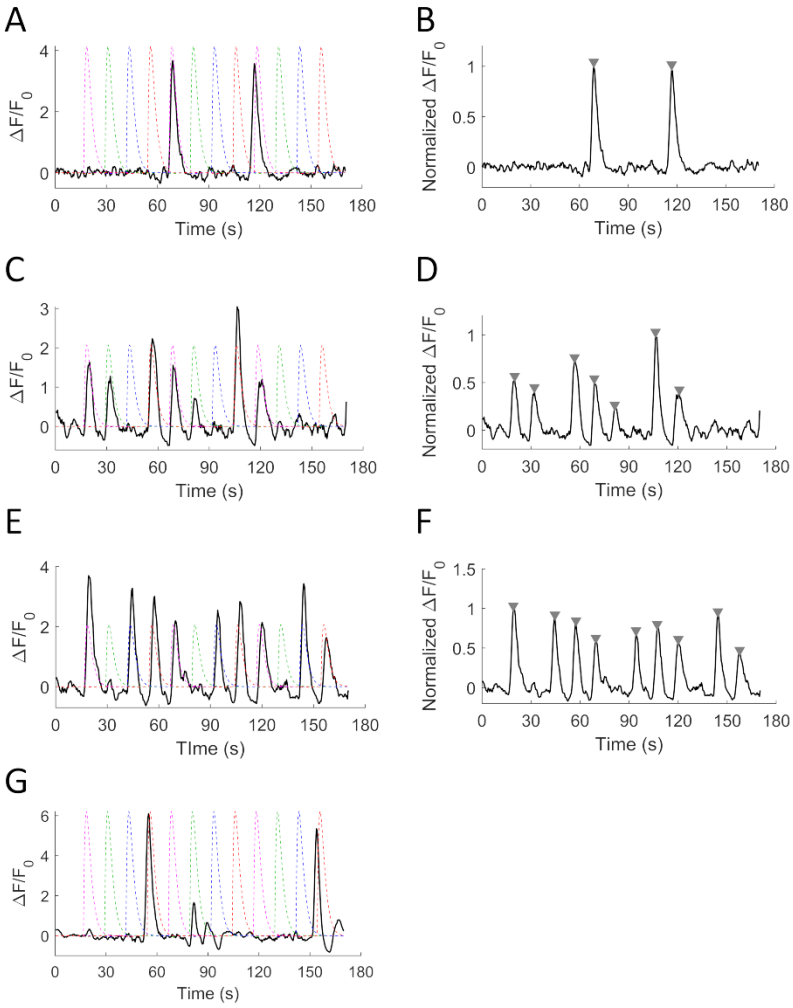

Figure 36. Robustness of peak analysis.

The figure shows the robust selection operated by peak analysis in filtering out spontaneous activity spikes. **(A)** The panel shows an example of $\Delta F/F_0$ trace overlapped with the regressors (dotted lines color-coded as follow: L_1-magenta, L_2-green, L_3-blue, L_4-red). The trace peaks in correspondence of two L_1 stimuli. However, this is a clear example of spontaneous activity as highlighted by lack of responses to all three stimuli and by the fact that the second peak starts before the stimulus. Regression analysis assigns to this responses the following T values: T_U 18.7, T_V -1.1, T_B 0.1, T_R -0.2. In this case such neuron would pass the T threshold selection since $T_U > T_{ThU}$ but is rejected by peak analysis. **(B)** The panel shows peak analysis selection on the normalized $\Delta F/F_0$ trace shown in A. The grey arrowheads highlight the peaks found by this analysis. Since we decided to select only responses following the three stimulus repetitions, the response displayed in the panel (albeit above T_{Th}) will be

discarded by peak analysis. **(C)** The example shown in this panel illustrates a $\Delta F/F_0$ trace of a neuron responsive to all three repetitions of L_1 and with peaks of activity synchronized with L_4 (two peaks) and L_2 (one peak) stimuli. Regression analysis assigns the following T values: T_U 17.1, T_V 7.0, T_B 0.05, T_R 21.2, thus classified it as responsive to both L_1 and L_4. The effect of peak analysis on this trace is shown in panel **D**. **(D)** The panel displays all peaks identified by peak analysis and, imposing a selection based on three peaks for each stimulus, it is considered and included in our data as responsive to only L_1. **(E)** Exemplary trace of a neuron responsive to L_1, L_3 and L_4 passing both T_{Th} and peak analysis selection criteria (no spontaneous activity spikes are present) and the correspondent peak analysis selection **(F)**. **(G)** $\Delta F/F_0$ trace of a clear example of spontaneous activity with a response peaked at two repetitions of L_4 stimulus. The trace also shows the trend of such response with the second peak starting before the visual stimulus, clearly a spontaneous spike.

Table 2 shows a quantification of such responses obtained by analyzing the number of neurons above threshold for each T and measuring the percentage of these active during each stimulus repetition. The combination of these two selection criteria (threshold and peak analysis) ensures that the data shown in this work can be attributed to the visual stimuli. Indeed, the percentages reported in the Table confirm that the concern that gave rise to peak analysis is justified, especially for the wavelengths with low numerical consistencies of responses in the caudal regions.

	Encephalon			Spinal cord		
	Above T_{Th}	Above T_{Th} + Peak analysis	%	Above T_{Th}	Above T_{Th} + Peak analysis	%
L_1	5356	4920	92%	138	128	93%
L_2	59	55	93%	1	1	100%
L_3	777	735	95%	40	11	27.5%
L_4	2681	2614	97%	0	0	0%

Table 2. Threshold analysis vs. peak analysis.

Quantification of responsive neurons for each stimulus (L_1, L_2, L_3, L_4) in the whole encephalon and in the spinal cord for seven larvae at 5 dpf. The table shows quantifications obtained by applying only threshold selection and by implementing peak analysis in addition to threshold selection, thus including in the data only neurons responding to all three stimulus repetitions.

4.4 Neuronal tuning to light of different colors – wavelength-independent analysis

We first quantify neuronal responses without spectral selection; this can be accomplished by applying the T_{Th4D} to the data. Figure 37A shows data ranked by T_{4D} values in descending order for 600 neurons in one 5 dpf larva. The $\Delta F/F_0$ heatmap shows the strong calcium responses associated with the visual stimuli (indicated in their respective color-codes at the top of the panel) for each of the 600 neurons selected (each row represents a neuron). Inspection of these data show that high T_{4D} values are associated especially with neurons strongly responding to L_1 and L_4 stimuli, and to a lesser extent to L_3, while very few responses are associated to L_2 stimulus. The neuron spectral identity is shown in the spectral column to the right of the heatmap. Note that in this column each stimulus is highlighted if the T value measured for that wavelength in that neuron is above the threshold for that stimulus and the three-peak selection has been passed (i.e. the response peaks at all three stimuli, see methods). The anatomical localization of these neurons shows that they are mainly, but not exclusively, distributed in the mesencephalon. Indeed, as shown by the anatomical column (Figure 37A, right panel), spectral responses were also found in other CNS regions (i.e. telencephalon, eyes, diencephalon, rhombencephalon, spinal cord). We then pooled the data from all 5 dpf larvae (N = 7 larvae, n. of responsive neurons = 12078) in Figure 37B, which shows all neurons above T_{Th4D} registered onto a reference brain for anatomical localization and correct overlay of data from different larvae. The anatomical distribution highlights the presence of positive neurons throughout the CNS regions mentioned above. The density of neurons observable in the different regions across seven larvae confirms the trend highlighted in the anatomical column of Figure 37A for one larva, with a high density of responsive neurons in the mesencephalon, but also distributed outside this region up to the spinal cord. We then spectrally and anatomically characterized all responsive neurons across the seven larvae. The spectral quantification (Figure 37C, top panel) points out predominant responses to L_1, followed by L_4, L_3 and a very small number to L_2. The anatomical data (Figure 37C, bottom panel), on the other hand, show the highest density in the mesencephalon. That the density of spectrally-

responsive neurons should be highest in this region of the CNS is expected, since it comprises the principal areas for processing visual (along with other sensorial) information (for example the optic tectum and the other retino-recipient areas). However, we also identified positive neurons in all other encephalic areas and in the spinal cord, indicating that the circuitry in charge of processing spectral information and color-selective responses is not limited to the mesencephalon. As anticipated above, these data based on T_{4D} selection provide an overall view of responses without an *a priori* spectral selection.

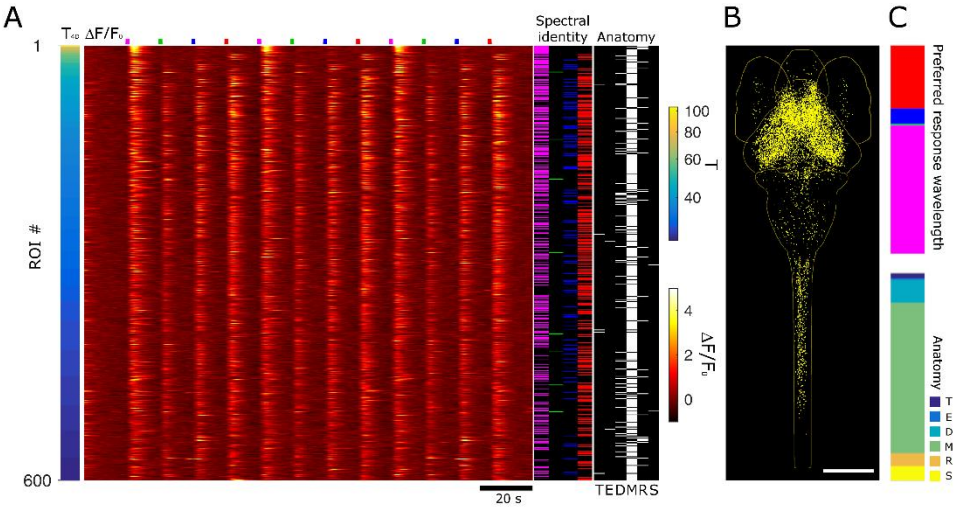

Figure 37. Overall view of stimulus-induced responses without spectral selection.

(A) Heatmap of 600 ROIs ranked by T_{4D} values in one 5 dpf larva. The bar on the left shows T_{4D} values (mapped with the T color scale shown on the right of the panel). The main panel shows a heatmap of $\Delta F/F_0$ calcium responses of the 600 neurons (mapped with the $\Delta F/F_0$ color scale shown on the right of the panel). Stimulus time points are indicated in their respective color-codes above the panel. The spectral column (next to the heatmap) indicates the spectral identity of each neuron as determined by threshold analysis: magenta, green, blue and red lines indicate neurons responsive to L_1, L_2, L_3 and L_4 stimuli, respectively; black indicates no response above threshold to the visual stimulus. The anatomical column shows the localization of each of the 600 neurons (T: telencephalon, E: ganglia eyes, D: diencephalon, M: mesencephalon, R: rhombencephalon, S: spinal cord). **(B)** Anatomical map of neurons selected above the T_{4D} threshold (each neuron is represented as a yellow dot) for 7 larvae at 5 dpf registered onto a reference brain (outlines of the anatomical regions mentioned above are displayed in light yellow). **(C)** Quantification of spectral and anatomical identities (N=7 larvae). The top bar graph shows

the normalized distribution of all responsive neurons above the T_{4D} threshold across the four spectral stimuli (with their respective color-code). The bottom bar graph quantifies the anatomical distribution of the neurons across CNS areas with the following color-coding from top to bottom: dark blue: telencephalon; light blue: eye, turquoise: diencephalon, green: mesencephalon, orange: rhombencephalon, yellow: spinal cord (see legend). The same data with standard errors are shown in Appendix (Figure A1).

4.5 Spectral identity and anatomical maps of responsive neurons in 5 dpf larvae

The four-dimensional threshold (T_{Th4D}) has the advantage of selecting any neuron that shows a response to at least one stimulus including neurons that would not otherwise be selected as positive based on the thresholds specifically used for each stimulus. For a better understanding of this point, Figure 38 shows a scatter plot of the pairwise correlations of T-values. In this plot each neuron is shown as an individual dot and its T-values are shown by placing the dot with an x-value corresponding to the T_U of the neuron and a y-value corresponding to its T of any of the other three stimuli; the color of the dot codes which stimulus is represented, so the green dot display T_V on the y-axis, the blue and red T_B and T_R, respectively. Looking at this graph, it is evident that the selection of neurons responding to the different stimuli based on applying to each stimulus its threshold (colored dashed lines in the figure) tends to leave out some responsive neurons that clearly lie outside of the control distribution (black dots in the figure). Based on this observation we calculated the 4D threshold as described above, thus selecting neuros for which there is a 99% probability to be correct stating that they respond to at least one of the four stimuli but without necessarily being able to point out which one.

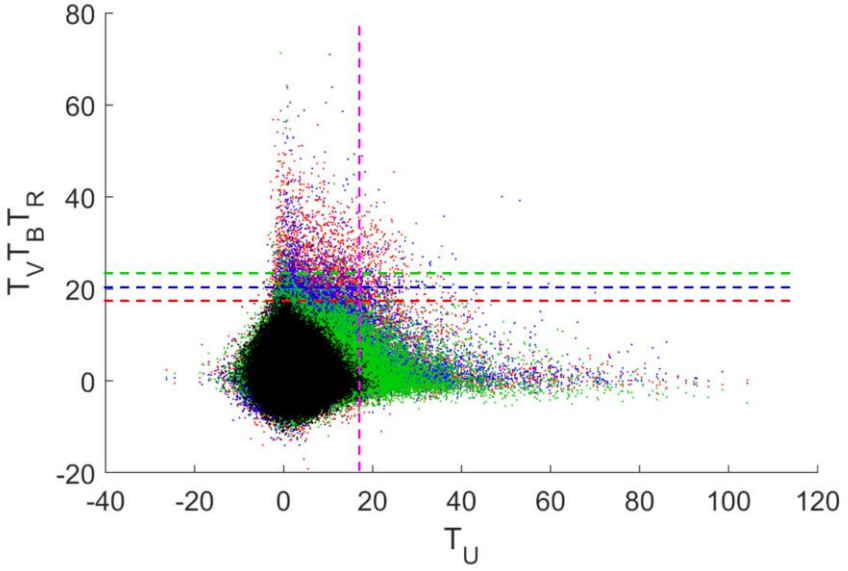

Figure 38. Pairwise response correlation.

Correlation of T-values between L_1 (horizontal axis) and L_2, L_3, and L_4 stimulation (vertical axis). Each black point in the graph is the measurement of the T values for each neuron identified in the control (N=5 larvae at 5 dpf recorded in absence of visual stimulation), while the colored points are the T values measured for each neuron in seven larvae at 5 dpf and specific for each stimulus (shown in their respective color-code in the figure). The dashed lines indicate the T threshold value for each stimulus (magenta-L_1, green-L_2, blue-L_3, red-L_4). The statistics reported in the figure are cumulated over the total number of ROIs segmented over all larvae for each condition: 847068 (3 dpf stimulated); 588198 (3 dpf control); 845070 (5 dpf stimulated); 518409 (5 dpf control).

To assess each stimulus specifically, we next ranked neurons based on each single T (L_1, L_2, L_3, L_4, separately), thus selecting neurons responding (with 99% confidence) to that stimulus, independently on the possibility that a neuron may respond to multiple stimuli (more on this in the following paragraph). Figure 39A shows $\Delta F/F_0$ heatmap of 600 neurons ranked by L_1 stimulus in one larva at 5 dpf (the same larva shown for T4D in Figure 38). The data show a robust response, with high T values in a large number of neurons, to the selected wavelength. Neurons spectral identity is also visible in the spectral column obtained by operating both threshold and peak selection. The latter criterion is highlighted along the spectral column as an interruption of the colored strips (Figure 39A, right panel), indicating

the presence of responses above the T threshold for the chosen stimulus whose activity does not follow the repetition of the flashes (and so they do not pass peak analysis). These responses are shown for a more complete understanding of our analysis method and overall assessment of the data quality but they were not included in our data. The anatomical column for the selected larva confirms the expected dominance of the mesencephalic localization with a lower (but not negligible) density of L_1-selective responses outside this region. The cumulative anatomical distribution across seven larvae (Figure 39B) confirms the mesencephalic dominance once again; however, significant spectrally-defined responses across the CNS (especially diencephalon and rhombencephalon), including the spinal cord, are also present. Spectral and anatomical quantification of these responses are shown in Figure 39C. Figure 39D, G, J show heatmaps ranked by L_2, L_3 and L_4 stimulus, respectively (same 5 dpf larva shown in the previous heatmaps). $\Delta F/F_0$ traces demonstrate the dominance of the stimulus selected for ranking over the others in each panel with L_2 providing the weaker responses among the other stimuli, followed by L_3, whereas L_4 provides stronger responses, comparable to those to L_1. In each spectral panel, the selection induced by ranking clearly demonstrates the presence of neurons robustly responding to a single wavelength stimulus but also some neurons responding to more than one wavelength. Regarding the anatomical distributions of these responses both in one larva (Figure 39D, G, J, right panels) and across seven larvae (Figure 39E, H, K), as for L_1 stimulus, the mesencephalon predominates over the other brain regions, as expected. Generally, L_2 stimulus does not elicit significant responses and they are localized mainly in the mesencephalon (Figure 39F, bottom panel). L_3 and especially L_1 responses, on the other hand, spread to the most caudal regions (Figure 39I, L, bottom panels). These data highlight that neurons in the spinal cord participate in responses only to the shorter wavelengths, lacking response to the L_4 stimulus. Thus, it is possible that long wavelengths in our measurements do not elicit color-evoked behaviors, in contrast with short ones that do. Indeed, we assume that the sensorimotor transformations elicited by the light flash stimuli may generate motor-related behaviors (probably comparable to startle responses) in which the discrimination of different wavelengths may play an important role. We expect that the spectrally-responsive spinal neurons take part of circuits involved in processing spectral information receiving inputs from the upstream regions. The lack of responses to long wavelengths in the spinal cord may thus be associated to the absence of circuits responsible for these type of responses, at least in this stage of development. Moreover, we need

to take into consideration two different aspects: the transparency of the larva and the position of our stimulator. Regarding the first it is possible that the transparency of larvae makes them more susceptible to short wavelengths-related motor events since short wavelengths could be dangerous at the larval stage. The position of our stimulator, on the other hand, evokes responses mainly in the area temporalis of the retina where UV circuits are the most abundant. It has been demonstrated that these circuits are involved in prey capture behavior (more on this in discussion), thus explaining the abundance of responses to this stimulus we found in the caudal region.

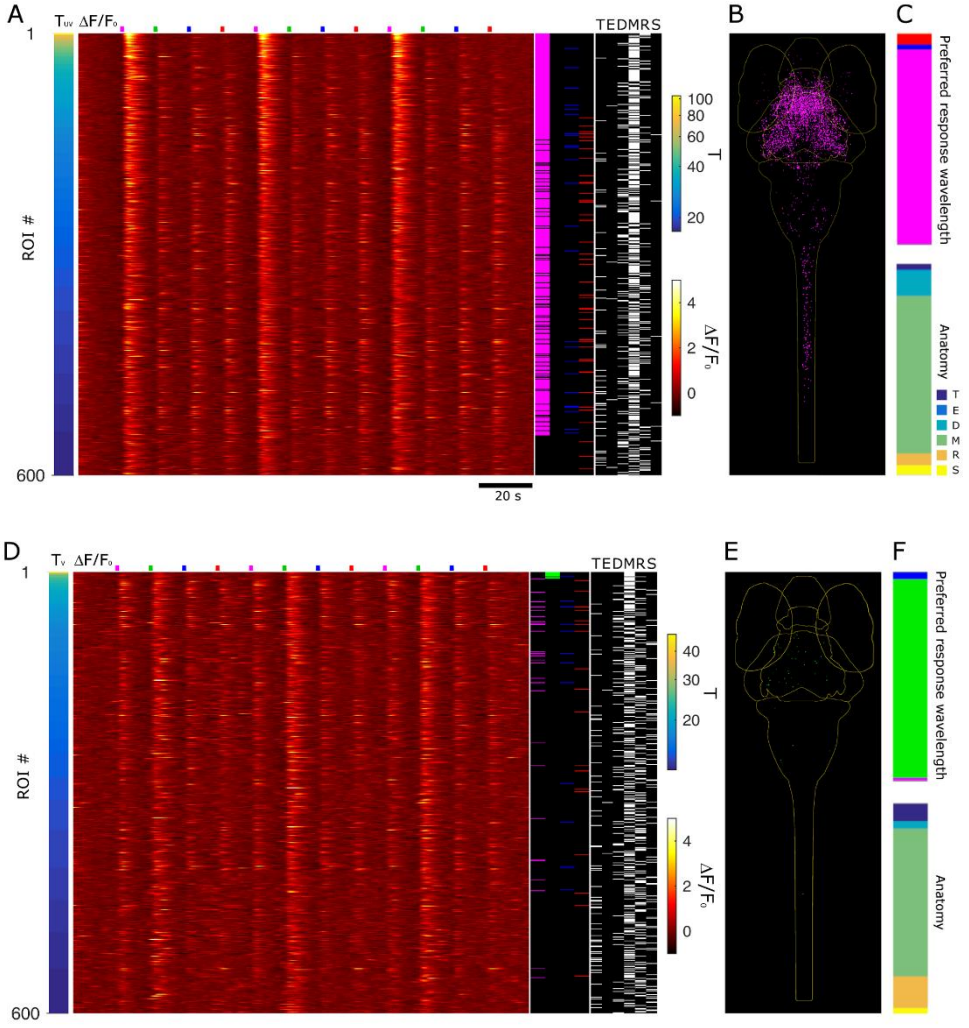

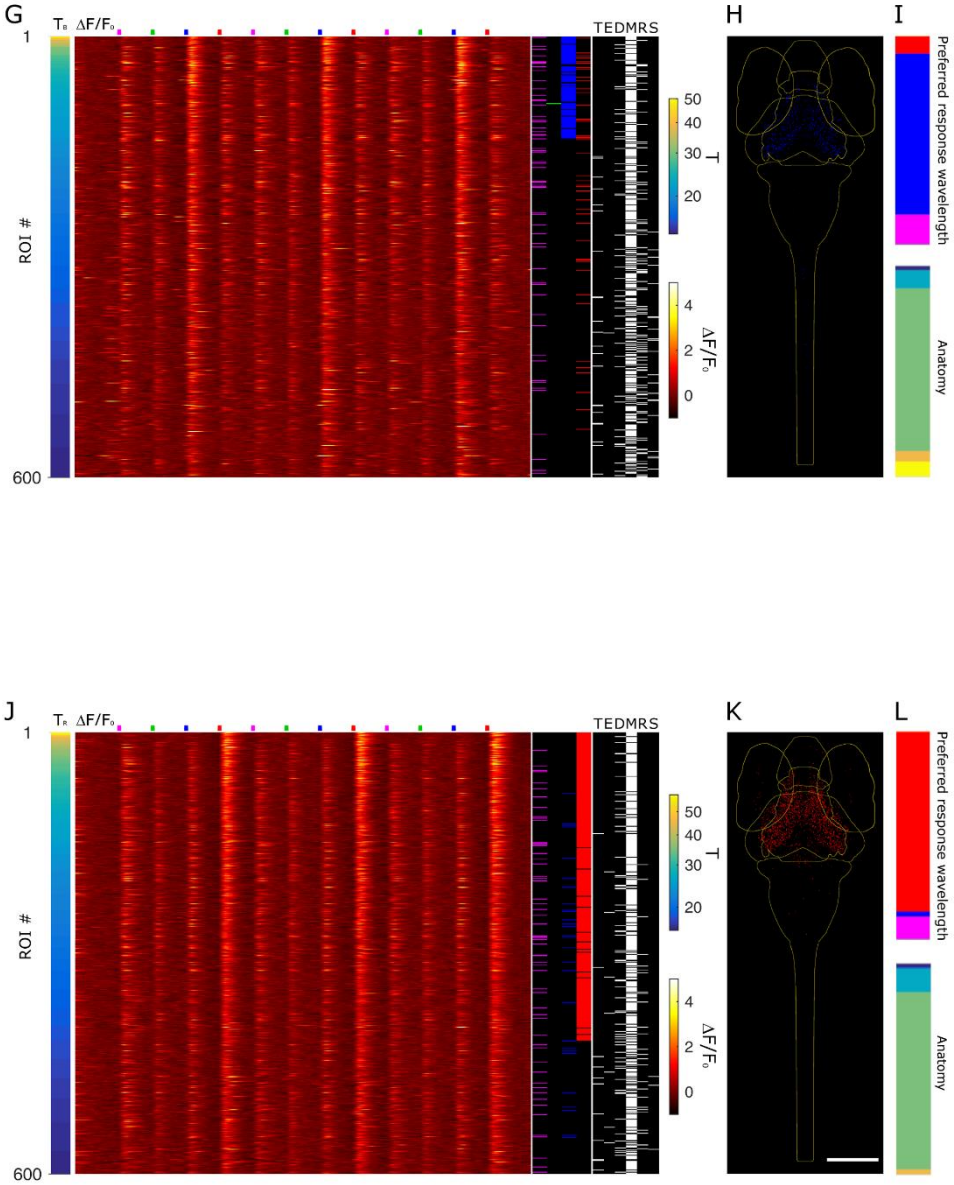
G
H
I
J
K
L
ROI #
1
600
TEDMRS
T
ΔF/F₀
50
40
30
20
4
2
0
Preferred response wavelength
Anatomy

Figure 39. Stimulus-induced neuronal activity: spectral and anatomical mapping.

A, D, G, J Heatmap of 600 ROIs (mapped with the $\Delta F/F_0$ color scale shown on the right of the figure) with ranking based on T_{UV}, T_V, T_B, T_R, respectively, for one larva at 5 dpf. Stimulus time points are indicated above each panel. The T value of each ROI is shown by the bar on the left with the color map shown on the color scale to the right of the heatmap. The spectral panels next to each heatmap show neurons spectral identity (each row represents one neuron). The neurons failing to show L_1, L_2, L_3 and L_4 identity in the spectral column while still having $T_{UV}>T_{ThUV}$, $T_V>T_{ThV}$, $T_B>T_{ThB}$, $T_R>T_{ThR}$, respectively appear as black lines across the colored strips and represent those cells that get filtered out by peak analysis. The anatomical column shows the localization of each of the 600 neurons (T: telencephalon, E: eyes, D: diencephalon, M: mesencephalon, R: rhombencephalon, S: spinal cord). **B, E, H, K** show anatomical distributions of all neurons passing threshold and peak analysis selection for L_1, L_2, L_3 and L_4 stimulus (magenta, green, blue, red dots), respectively, across seven larvae at 5 dpf registered onto a reference brain (the light yellow outlines show the different brain regions). Scale bar: 190 µm. **C, F, I, L** panels display cumulative spectral (top panels) and anatomical (bottom panels) quantifications of responsive neurons (N=7 larvae). The top bar graphs show the normalized distribution of all responsive neurons above the T_{Th} threshold across the four spectral stimuli (with their respective color-code). The bottom bar graphs quantify the anatomical distribution of the neurons across CNS areas with the following color-coding from top to bottom: dark blue: telencephalon; light blue: eye, turquoise: diencephalon, green: mesencephalon, orange: rhombencephalon, yellow: spinal cord (see legend). The same data with standard errors are shown in Appendix (Figure A1).

4.6 Spectral classification: T barcode

When looking at the spectral panels (Figure 39A, D, G, J), we can notice the presence of subsets of neurons responsive to multiple wavelengths. Due to the sequential stimulation in our experiments, we can assess the responsivity of each neuron to any of the stimuli and uniquely identify it based on the stimulus or stimuli it is sensitive to. For this aim, we defined a classifier, which we termed "Tbar" (where bar stands for “barcode”, see methods) which takes values from 1 to 15, based on the stimulus/i response of the neuron. Figure 40A shows average $\Delta F/F_0$ traces for all neurons belonging to Tbar classes significantly populated (n>10 neurons) across 7 larvae at 5 dpf. The traces demonstrate the presence of responses to one stimulus (Tbar classes 1, 2, 4 and 8 in Figure 40A, representing “monochromatic” responses to UV, violet, blue and red. respectively) and multiple stimuli (Tbar classes 3, 9, 10, 11 in Figure 40A, which indicate response to red/blue, red/UV, UV/blue, UV/blue/red, respectively)

indicating the complexity of responses that are elicited in the larva CNS by the visual stimuli. The numerical consistency of each Tbar class reflects the spectral responses shown in Figure 39, whereas the anatomical distributions (Figure 40B) highlight again that longer wavelengths (L_4) are not represented in the caudal regions (i.e. rhombencephalon and spinal cord) where, on the other hand, shorter wavelengths (L_1, L_2, L_3) are represented singly or in combination. We then anatomically localize some neurons chosen as examples to show the variety of responses we observed in our measurements. Figure 40C shows the anatomical localization of 12 neurons highlighted with their respective color code according to the stimulus or stimuli they respond to. Spectral selectivity of these neurons is demonstrated in Figure 40D, where the $\Delta F/F_0$ traces associated with the 12 neurons selected are shown. The experimental traces clearly demonstrate the stimulus-induced and spectrally-selective nature of the response, confirming the robustness of the selection criteria adopted. As first observed in the T distributions shown in Figure 31, some neurons exhibit a negative response to light (mainly UV). The last panel of Figure 40D shows the $\Delta F/F_0$ trace of one of these neurons belonging to the pineal region (neuron #12 in the figure). The Tbar selection includes all neurons passing threshold and peak analysis criteria so that the weaker responses to the stimuli outside the Tbar classification are excluded. (In light of this observation, looking at the average $\Delta F/F_0$ traces in Figure 40A we can see that responses to single wavelengths (i.e. Tbar 1, 2, 4, 8) are characterized by a single peak of higher amplitude in correspondence of each respective spectral stimulus (for example responses belonging to Tbar class 1 exhibit a high amplitude peak associated with L_4 stimulus) and by lower amplitude peaks in correspondence of the other stimuli not included in Tbar class selection (for example the lower peaks associated with L_1, L_2 and L_3 stimuli in Tbar class 1). The presence of lower amplitude peaks which do not pass selection criteria is more evident in Tbar classes related to responses to multiple stimuli (i.e. Tbar class 3, 9, 10, 11). The most evident example lies in Tbar class 11. This class indicates responses to L_1, L_3 and L_4 stimuli (Figure 40A); however, observing its corresponding average $\Delta F/F_0$ trace we notice also a peak (although with lower amplitude compared to the others) associated with L_2 stimulus, which does not belong to such Tbar class. The exclusion of this peak, and also of the others lower amplitude peaks in the different Tbar classes, from the Tbar class selection depends on the very stringent T thresholds we applied for each wavelength (as discussed in the paragraph above). In the example just depicted (Tbar 11) even if it is possible to observe, on average, some response to L_2, we had

to exclude it from Tbar class 11 given the high T threshold for such stimulus. We can state that features that emerge in an average trace, of course, cannot be used to justify selection on the individual traces. That is to say that the only statistically reliable and robust criterion we could adopt for spectral selection is the threshold method based on FDR calculation. As stated above, the use of very stringent T thresholds (to ensure 1% FDR) cuts some responsive neurons out from our data leading to exclude responses that are actually elicited by our protocol of visual stimulation. This is the reason why we observe responses evoked by the different stimuli also in Tbar classes in which that stimulus does not belong. However, applying less stringent T thresholds would lead to include in the selection a larger fraction of false positives, thus a compromise had to be chosen insuring the strongest reliability of the selected data.

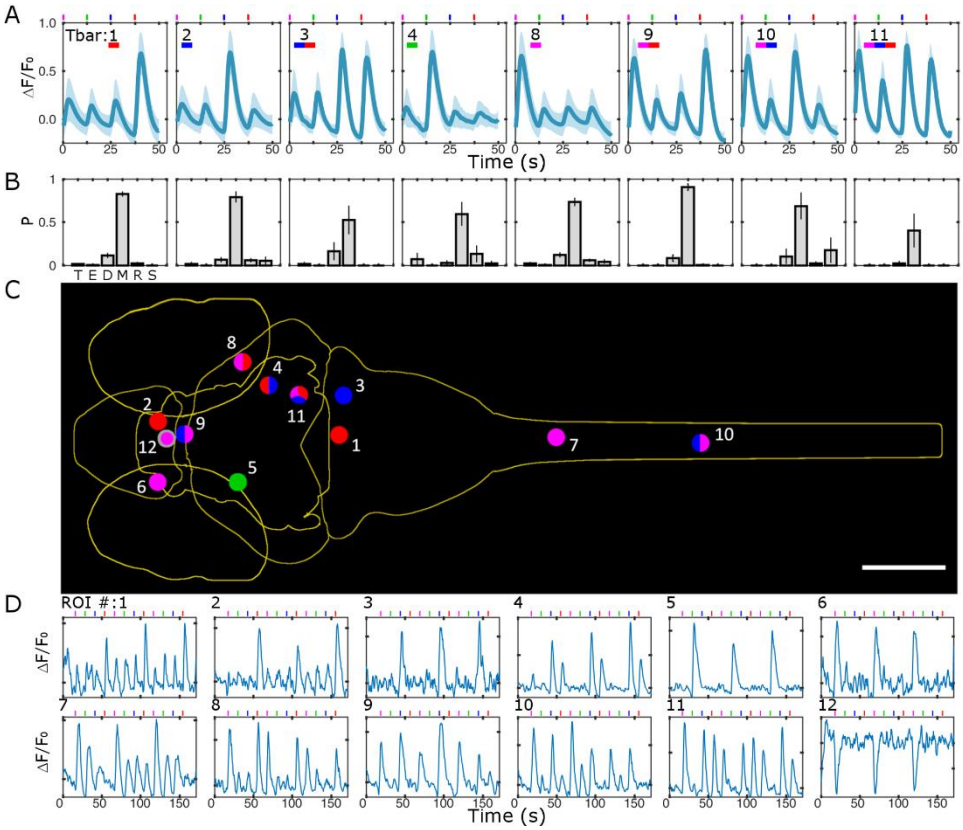

Figure 40. Unique spectral classification with Tbar.

(A) Average $\Delta F/F_0$ traces (blue line: mean; light blue area: standard deviation) for all neurons identified with the given Tbar (indicated in each panel). Number of neurons: 2243 (Tbar 1); 581 (Tbar 2); 49 (Tbar 3); 51 (Tbar 4); 4509 (Tbar 8); 308 (Tbar 9); 88 (Tbar 10); 14 (Tbar 11). The experimental trace of each neuron was first averaged over the three repetitions of the $L_1/L_2/L_3/L_4$ stimuli before averaging among different neurons. Standard deviations were calculated over all data (made of the three repetitions for each neuron, over all neurons found in each class for the seven larvae tested). Colored tick marks above each graph show the timing of the different stimuli. Only the classes with a total numerical consistency above 10 neurons are shown in the figure. The colored bars below each Tbar value indicate the spectral stimulus(i) to which neurons belonging to that class are responsive to. **(B)** Anatomical distributions of neurons for each Tbar class. Anatomical areas are classified and indicated as in the rest of the thesis: Telencephalon (T), Eye (E), Diencephalon (D), Mesencephalon (M), Rhombencephalon (R), Spinal cord (S). Values shown are averages and stderr calculated over the seven normalized distributions measured with the 7 larvae for each Tbar. The bars for the last plot (Tbar 11) do not add to 1 because the distributions were normalized to 1 for each larva across the anatomical areas but not all larvae tested actually contributed cells to this Tbar class (i.e. some larvae contributed 0 into averaging). **(C)** Anatomical localization of some example neurons for each of the Tbar classes shown in the previous panels. Each neuron is shown as a dot (not drawn to scale, for visibility) and colored according to its response(s) with the color-coding used throughout the thesis. The grey border around neuron #12 indicates a negative T value (T_{UV} = -23.6). Scale bar: 150 µm. **(D)** Experimental $\Delta F/F_0$ traces for the neurons shown in panel C. The scales were chosen to optimize visibility in each graph and are not shown for compactness of the figure; the two ticks shown on the vertical axis are as follows for each panel starting from top left: (-0.5, 2.2), (-0.3, 1.2), (-0.3, 1.4), (-0.6, 4.3), (-0.5, 3.7), (-0.3, 1.4), (-0.6, 2.1), (-0.5, 3.0), (-0.3, 1.3), (-0.4, 3.4), (-0.5, 4.0), (-0.4, 0.2).

To further demonstrate the consistency of Tbar classes without an *a priori* stimulus selection, we ranked neurons based on their T_{4D} values and evaluated their Tbar class. Figure 41A shows ~13000 neurons across seven larvae ranked by T_{4D} values and associated to their corresponding Tbar class (plotted on the y-axis). These data show a dominance of the Tbar classes 1, 2 and 8, and, to a lesser extent, 3, 4, 9, 10. We further tested Tbar consistency by applying a T threshold of 15 to all four stimuli (Figure 41B). These data show that T bar classes mainly represented are the same shown in Figure 41, the only difference is that by applying a lower threshold each Tbar class is populated by a higher number of neurons, whereas the spectral identity of the responses does not change; i.e. the Tbar classes shown in Figure 40 emerge in a substantially threshold-independent manner. Thus, the data show that the Tbar clusters do not depend significantly on the choice of threshold, excluding a potential issue that has to be considered

when using threshold analysis. We should note that this increase of numerical consistency will indeed comprise responsive neurons (i.e. reduce false negatives) but at the expense of an increase of false positives.

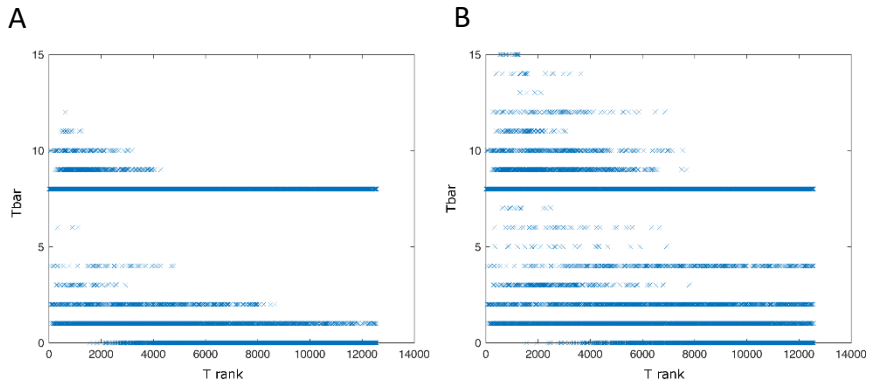

Figure 41. Tbar clusters in responsive neurons.

Neurons from the seven experimental larvae are ranked based on their T_{4D} value. Each neuron is plotted on the x-axis based on its T4D rank, while the values along the vertical axis correspond to its Tbar class. **(A)** The graph shows neurons classified for their Tbar class based on the thresholds used in our analysis. The data demonstrates a clear and strong emergence of the classes shown in Figure 40. **(B)** The same as in panel A plotted changing the threshold criterion and setting the threshold to 15 for all the four stimuli. This graph shows that the Tbar clusters do not qualitatively change, while, of course, their numerical consistency increases.

4.7 Dynamics of spectrally-tuned neuronal responses

To further demonstrate the sensory nature of the responses we observe, a histogram of peak timepoints was measured for each stimulus (Figure 42). We analyzed the distributions of peak timepoints for all neurons (N = 7 larvae) above each corresponding stimulus T threshold and compared them with the same analysis applied to the control data (N = 5 larvae). These results point out that the responses measured in the stimulated larvae indeed reflect spike of activity triggered by the spectral stimuli and follow the GCaMP6s dynamics.

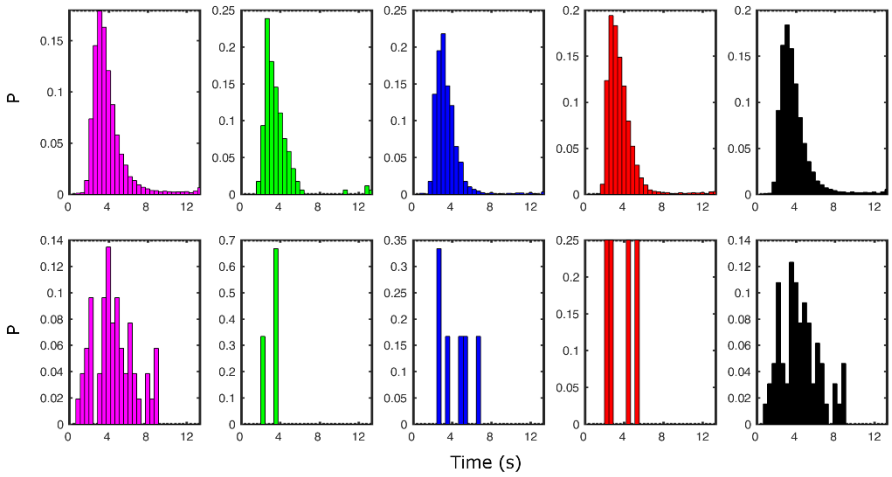

Figure 42. Calcium response dynamics.

The graphs show histograms of the distributions of peak times for the neurons responsive to each spectral stimulus (i.e. selected based on the respective thresholds and shown with its color code in the first four panels) and the cumulative distribution of all responsive neurons regardless of the stimulus wavelength. The top graphs show data measured on the experimental larvae (N = 7) that were visually stimulated, the bottom graphs show data measured on control larvae (N = 5) that were not visually stimulated. The time shown on the x-axis is measured relative to the presentation of the stimulus (t=0).

One more issue we considered to further assess the spectral specificity of responses observed is the presence of possible history-dependence effects. Indeed, since we applied a precise order of spectral stimuli (L_1, L_2, L_3, L_4 in triplicate), we wanted to verify if the order of the stimuli affects the responses we mapped. In other words, given the high number of neurons responsive to L_1 stimulus we found, and the fact that L_1 stimulus is the first one presented in our protocol, it might elicit stronger responses than the other stimuli or even inhibit/hinder such responses, exerting a sort of inhibition towards the other stimuli. This would represent an issue for the purpose of neurons spectral identification. We tested this possible history-dependent effects by performing stimulation of the same neuron populations across the larva brain volume with two different stimulation time patterns: our standard stimulus pattern, and a shuffled pattern L_3, L_4, L_2, L_1, L_4, L_3, L_1, L_2, L_2, L_3, L_4, L_1. For these experiments, we recorded

neuronal activity with both stimulation protocols on the same planes (10 planes sampled with 20 µm z-step) waiting 120 s between the two consecutive acquisitions (N = 3 larvae at 5 dpf). To investigate whether the responsive neurons maintain their spectral specificity regardless of the order of the stimuli, or rather possible history-dependence effects appear, we produced correlation plots comparing the responses (i.e. the T values) of each neuron to the four stimuli between standard and shuffled data (Figure 43A). From these data, it is possible to observe that a large population of neurons shows strong correlations, especially for L_1, L_3 and L_4 stimuli, responding to the same stimulus with similar strength independently of the order of the 12 stimuli. Figure 43B shows $\Delta F/F_0$ traces (across three larvae) of neurons maintaining spectral identity in spite of the different order of the stimuli. This is better quantified in Table 3 reporting the responses to the four stimuli calculated for both protocols. Although these percentages are in the order of 50-60%, it is important to consider several aspects leading to underestimation of such percentages. One consideration regards a slight drift occurring between the two acquisitions. We corrected in-plane (i.e. x-y) drift by registering the two acquisitions for each plane to each other and performing segmentation on a single MIP resulting from combination of the two MIP images. This segmentation thus provided one mask that was applied to analyze the same neurons in both planes for direct comparison of their responses to the different stimulus order (more on this in the methods section). Unfortunately, no correction could be applied for a similar drift occurring in the z-axis. Although this drift was quite small, the nature of two-photon imaging can easily lead to lose/gain some neurons in each of the two acquisitions with respect to the other; so, some neurons that respond to one order of stimuli and show a drop of T in the other order do so not because they stop responding due to a history-dependent effect but because they have simply moved out of the narrow two-photon excitation focal volume. Another factor to consider is the threshold selection criterion applied to our data. By its own nature, any threshold establishes a hard cutoff so that neurons responding close to it might be some times above and some times below, obviously not because of a change in their spectral sensitivity but simply because of a fluctuation of the strength of their response about the threshold.

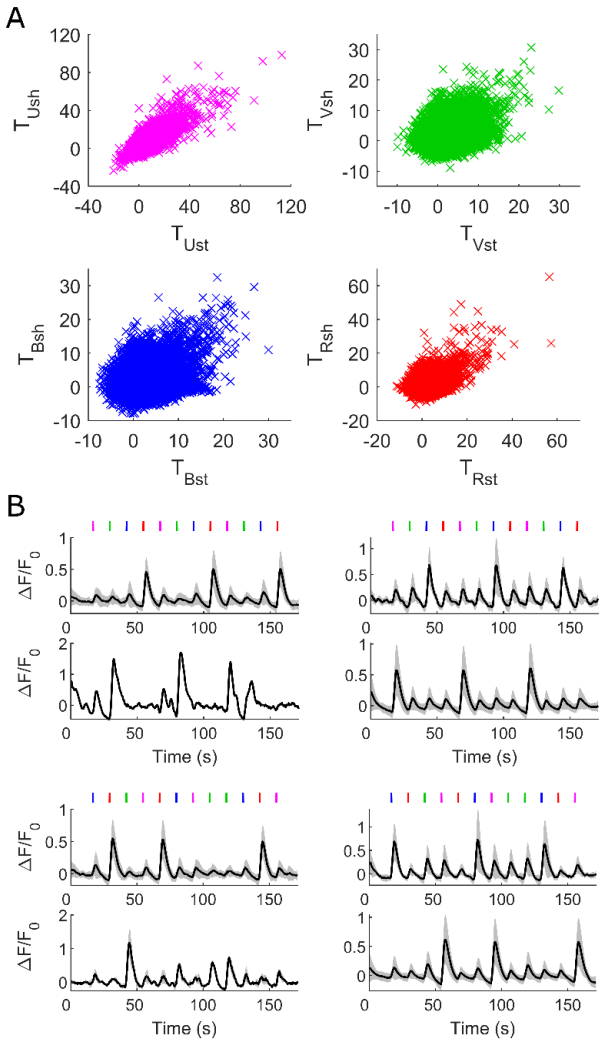

Figure 43. Robustness of spectral identity versus history-dependence: standard vs shuffled pattern of visual stimuli.

(A) Correlation plots of T values for each of the four stimuli (L_1-magenta, L_2-green, L_3-blue, L_4-red) between data acquired with the standard and shuffled protocol of visual stimulation (N = 3 larvae). **(B)** Average $\Delta F/F_0$ traces (black line: mean; grey area: standard deviation) of neurons responding to L_1, L_2, L_3, L_4, (indicated in orange) and calculated for both stimulation protocols (standard, top panel; shuffled, bottom panel). Stimulus time points are indicated in their respective order and color-code.

Thus, those neurons which appear to respond to one stimulus in the standard order but not in the shuffled one (or vice versa) do not necessarily represent an actual switch from one spectral class to another but rather could be affected by slight changes in T values leading them to fall below threshold selection. Tbar class analysis among these responsive neurons further demonstrates their spectral identity. Indeed, it reveals that variations of Tbar classes between standard and shuffled data do not represent a real change of neurons spectral identity but rather we observe a shift between classes sharing a response to the same stimulus. For example, some neurons

responsive to L_1 stimulus with the standard pattern which belong to Tbar class 8 are found in Tbar classes 10 and 14, where L_1 stimulus is also included, in the shuffled data. These observations, together with the analysis methods we employed (described above) allow us to assert that the majority of responsive neurons in our measurements maintain their spectral identity regardless of the order of stimuli presentation.

Stimulus	Standard	Shuffled	Shared	Percentage
L_1	614	627	408	66%
L_2	2	2	0	0
L_3	16	22	7	44%
L_4	73	54	29	54%

Table 3. Quantification of responsive neurons to standard and shuffled visual stimulation pattern.

The table quantifies the number of neurons across 3 larvae responding to the four stimuli with both protocols (standard and shuffled) and neurons which maintain the same spectral identity with both protocols (shared). We identified a total of 45766 ROIs across three larvae. The percentage reported refers to the ratio between shared and standard.

One final assessment of the spectral identity of the neurons we mapped was done in regards to the data analysis. This point was introduced based on Figure 32, where we observed the drastic drop of T-distributions when analyzed with a random sequence of stimuli. Based on the use of thresholds, we can now quantify the number of neurons above threshold for each stimulus between standard and shuffled analysis. The quantification reported in Table 4 includes neurons passing both threshold and peak analysis selection. As displayed in Table 4, a drastic reduction of responsive neurons emerges from shuffled compared to standard analysis confirming that the spectral identity of neurons identified in this work is robust in regards to both experimental protocol and analysis parameters.

Stimulus	Standard	Shuffled	Percentage
L_1	5048	233	4.6%
L_2	56	7	12.5%
L_3	745	10	1.3%
L_4	2614	113	4.3%

Table 4. Quantification of standard vs. shuffled analysis.

The table quantifies the total number of neurons (encephalon and spinal cord) responding to one of the four stimuli (selected by applying T threshold and peaks analysis criteria) between standard and shuffled analysis (see also Figure 32 and methods). The percentage of neurons above threshold with the shuffled analysis in respect to standard one is reported in the table demonstrating the robustness of analysis and specificity of T with respect to the spectral identity of the stimuli. N = 7 larvae at 5 dpf.

4.8 Spectral and anatomical distributions in 3 dpf larvae

The same measurements described in the previous sections have been performed in larvae at 3 dpf. Figure 44A displays $\Delta F/F_0$ responses measured in one larva and ranked based on T_{4D}. Comparison with Figure 37A highlights the much weaker calcium responses measured at 3 dpf. The spectral column of the figure also shows a much smaller fraction of responsive cells, with an apparent shift in favor of L_4. The anatomical column, on the other hand, shows a more evenly scattered distribution of the higher ranked neurons across the encephalic regions. Figure 44B shows all responsive neurons identified in 7 larvae after registration onto a reference brain. The histogram of spectral responses (Figure 44C, top panel) indicates a strong dominance of L_4 responses followed by L_1 and a negligible response to L_2 and L_3. We then quantify the anatomical localization of neurons (Figure 44C lower panels) from these data. We can see that the mesencephalic dominance is not yet fully established at this stage of development. We then applied to this data the Tbar classification and we found that responses to multiple wavelengths (which might be, to some extent, an indication of integration activity) are extremely rare (Tbar 3 = 1 neuron, Tbar 5 = 1 neurons, Tbar 9 = 4 neurons; N = 7 larvae). In contrast, responses to single stimuli, especially to L_1 and L_4 prevail (Tbar 1 = 423 neurons, Tbar 2 = 8 neurons, Tbar 8 = 122 neurons across seven larvae). We can notice that at 3 dpf we found no neurons with spectral-specificity in the spinal cord, indicating that at this stage of development the circuitries carrying spectrally-dependent information down to the spinal

cord and, thus, possibly eliciting color-selective motor behaviors, are not yet functional.

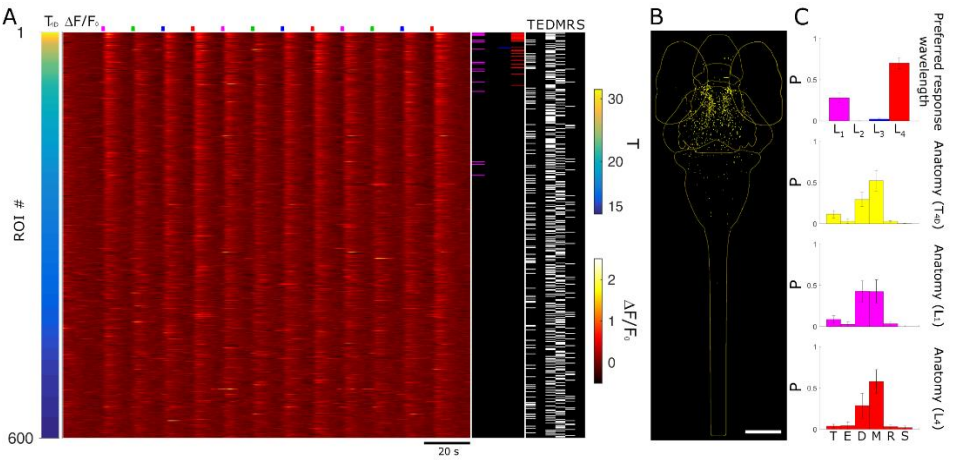

Figure 44. CNS spectral and anatomical mapping in 3 dpf larvae.

(A) $\Delta F/F_0$ responses of 600 ROIs ranked by T_{4D} values in a 3 dpf larva. Each row in the heatmap represents a neuron. The left bar indicates neurons T_{4D} values (T color scale is displayed on the right of the figure). Stimulus time points are indicated at the top of the panel highlighted in their respective color-codes. The spectral column on the right shows spectral responses of the neurons selected above threshold and peak analysis (highlighted in magenta, green, blue and red for the response to L_1, L_2, L_3 and L_4 stimulus, respectively). The anatomical column shows the localization of each ROI across the CNS regions (T: telencephalon, E: eyes, D: diencephalon, M: mesencephalon, R: rhombencephalon, S: spinal cord). **(B)** Anatomical map of neurons selected above the T_{4D} threshold (yellow dots) for 7 larvae at 3 dpf registered onto a reference brain for anatomical localization (light yellow outlines). Scale bar: 150 µm. **(C)** Quantification of spectral and anatomical identities (N = 7 larvae). The histogram on the top shows the normalized distribution of all responsive neurons above the T_{4D} threshold across the four spectral stimuli (displayed in their respective color-codes). The histograms on the bottom quantify the anatomical distributions of the neurons above T_{4D} (yellow histogram), T_{ThU} (magenta) and T_{ThR} threshold (red) (from top to bottom) across the CNS areas. Error bars = stderr, N = 7.

In opposition to the scarcity of positively responsive neurons (compared to the 5 dpf), we consistently find negatively responsive neurons also at 3 dpf. Figure 45 shows anatomical localization and an example trace for these neurons, which belong to the pineal region. Thus, we conclude that, while visual circuits are not fully developed, the inhibitory effect of light in the pineal gland is here demonstrated at single-cell level already at 3 dpf.

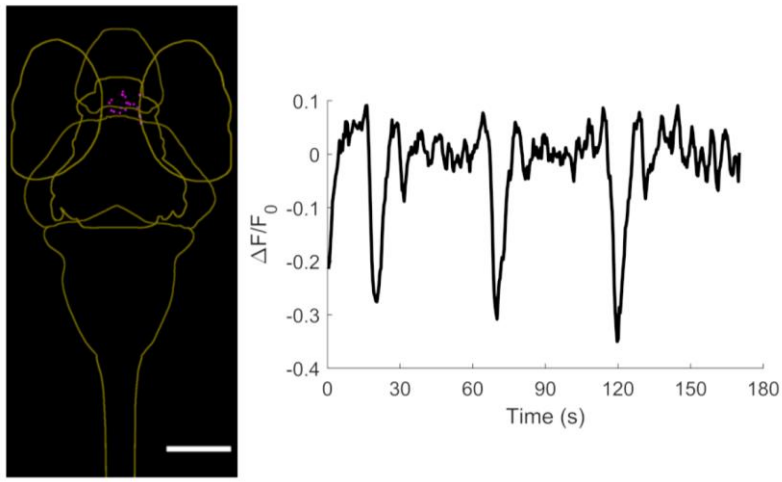

Figure 45. Anatomical distributions of inhibitory responses at 3 dpf.

Left panel: T-negative neurons identified specifically for L_1 stimulus (magenta dots) mapped in larvae at 3 dpf superimposed to a reference brain (light yellow outlines) for anatomical localization. The image highlights the localization of neurons responding in an inhibitory manner to L_1 radiation in the pineal region. Right panel: $\Delta F/F_0$ trace of an epiphysis neuron displaying a negative T value for L_1 stimulus as indicated by the following T score values: T_U = -29.6, T_V = -2.8, T_B = 2.3, T_R = 2.3. Scale bar: 150 µm.

Our measurements provide spectral and anatomical maps of neurons involved in spectrally-tuned responses in the zebrafish larva CNS. Besides the well-expected high density of responsive neurons in the visual areas of the mesencephalon (i.e. OT and other retinorecipient areas, which are the brain regions specifically involved in processing visual information and integrating it with other sensorial inputs), we found spectrally-defined responses also spread to all other brain regions, down to the spinal cord. It is possible that these neurons take part in circuits responsible for the propagation of spectrally-defined information presumably receiving inputs from mesencephalic neurons. Thus, we evidenced neural pathways maintaining spectral information throughout the CNS with predominant responses to L_1 and L_4 in 5dpf larvae, and to L_4 in 3 dpf larvae. These results open the way for a detailed dissection of the circuits responsible for different color-dependent behaviors with laser ablation, optogenetics or other perturbative experiments to investigate neuronal circuits underlying

color-evoked behaviors. The zebrafish larva is a very simple model yet representative of vertebrate CNS organization, so we expect the paradigm of spectral information propagating through non-visual areas to be relevant in all vertebrates.

4.9 Laser-induced cellular inactivation

The work described in the previous chapter provides a cellular-resolution mapping of spectrally-distinct responsive neurons across the zebrafish larva CNS. Understanding the structural and functional connectivity among these neurons, and so how they integrate specific inputs to generate a motor output, requires methods for deciphering the complex neuronal connectivity underlying these responses. Nowadays this is indeed one of the main challenges in Neuroscience, since it requires both a morphological and functional mapping of individual neurons in the whole brain. In this regard, the zebrafish larva represents the most suited vertebrate model for tackling this fascinating and daunting task. In fact, most of the limitations suffered by other models have been overcome in zebrafish larvae thanks to their optical transparency and the small size of the brain, in addition to the implementation of several technologies for circuits dissection. These technologies aim at providing a full mapping of neuronal morphology and/or perturbative approaches to control their function and monitoring the consequent circuit activity. Among the morphological strategies, the development of optical highlighting such as Brainbow imaging and photoactivatable fluorescent proteins allowed to resolve in a non-invasive way neurons and their projections [84, 88, 141]. These techniques, in fact, resolve one of the main aspects making morphological research of the nervous tissue so challenging compared to other tissues, i.e. the intricate structure of neurons and neuropil, with many circuit components often below the resolution limit of optical microscopy and certainly not discernible by conventional staining techniques. It was in fact the discovery of the so-called “black reaction” by Camillo Golgi at the end of the 1800s to first allow seeing the shape of neurons by labelling a small fraction of them [80]. About 150 years later, we would like to see all neurons at the same level of detail. Brainbow has been a step in implementing individual

mapping of all neurons in a dense and intricate structure. However, limits in number of colors attainable with this technique and in resolution of conventional fluorescence microscopy do not allow fully deploying this technique for the investigation of the whole brain of an animal. A more detailed morphological mapping is undoubtedly provided by electron microscopy, which allows 3D reconstruction of circuits at nanometric resolution, imaging all details of neuronal circuits down the single synapse level [82, 89]. To combine morphology with function, genetically-encoded calcium indicators represent a powerful tool enabling non-invasive measurements of intracellular [Ca^{2+}] variations in real-time, directly correlated with neuronal activity and synaptic transmission. This type of measurements thus enables optical highlighting/labeling of neurons in which the reporters are targeted and, at the same time, monitoring their activity. Most commonly, functional imaging requires immobilization of the sample under the microscope. This poses different issues depending on the animal model under investigation. One of the most relevant issue is that restriction of motion limits the monitoring of behaviors and might hinder them altogether. Several pathways for overcoming this limitation are currently being explored, both in regards to the development of novel probes (for example CaMPARI, [142]) and microscopy technologies apt to perform high-resolution 3D imaging in freely-behaving animals [143, 144]. In recent years, the development of photoconvertible proteins, such as CaMPARI, enabled to correlate neuronal activity with behaviors performed by the animal freely-swimming, whereas the most recent photoactivatable genetically-encoded calcium indicators (pa-GECIs) allowed to map processes and dendrites in individual neurons and to simultaneously monitor neuronal activity in a dense circuit structure [145]. Together with these strategies, perturbative approaches such as laser ablation and optogenetics, are widely employed to probe the function of individual neurons or neuron ensembles and dissect the circuits involved in response to specific stimuli and information processing, thus mapping neuron morphology and function [6, 146]. The anatomical and spectral maps provided in our work clearly require, as a next step, a correlation between morphology and function to decipher the connectivity patterns among the spectrally-responsive neurons identified and to study the color-evoked behaviors underlying them. With this aim, based on observations on GCaMP behavior during two-photon imaging, we have developed novel

optical approaches implementing both a perturbative and a highlighting strategy possibly applicable to circuitry mapping, based solely on the use of GCaMP. In this chapter, I will present these results, concerned with functional perturbation of responsive neurons and optical highlighting.

4.10 GLINP – harnessing the power of photodamage

Although calcium imaging through the expression of genetically-encoded calcium indicators allows monitoring neuronal-activity in a non-invasive way in the whole encephalon of the larval zebrafish, we observed that two-photon high-power imaging tends to induce a generalized and long-lasting activation of the whole raster scanning area. The expression of calcium reporters in this context helped us visualizing the effects of this procedure resulting in a massive increase of fluorescence intensity affecting the entire field of view (Figure 46). Based on the spectral and structural properties of GCaMP-family indicators, we know that the increase of fluorescence intensity in cells in which such indicators are expressed is associated with

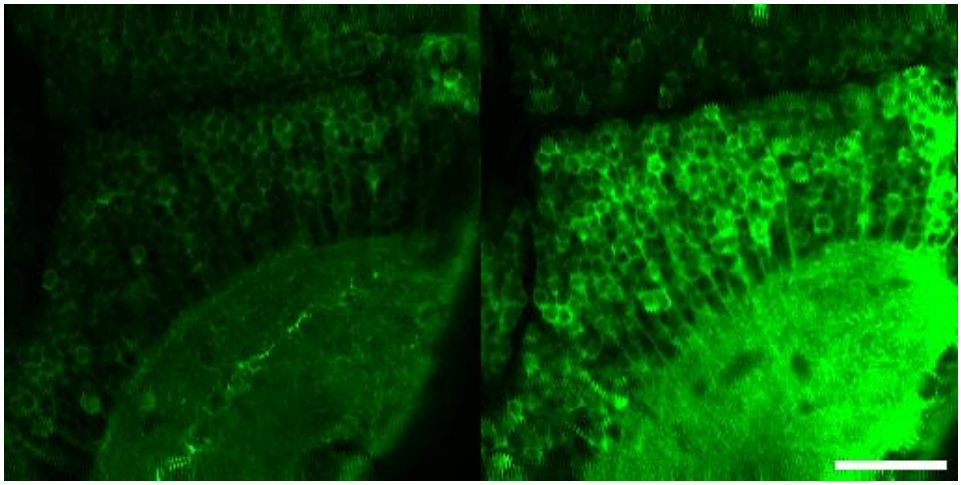

Figure 46. High-power two-photon imaging.

The panels show the effects resulting from two-photon imaging at high power. Here is shown an optic tectum plane of a 4 dpf Tg(elavl3:GCaMP6s) larva before (left panel) and after (right panel) imaging. It is possible to observe a generalized activation of the entire raster scanning area plane due to the high power of imaging restricted to the plane at issue. Scale bar: 40 µm.

a variation of intracellular [Ca^{2+}]. So, we assume that the "activation" we observe (in this part of the text, until further details are illustrated, I will use this term pointing at the observed fluorescence increase and neglecting, for now, the functional implications of what is going on in the neuron) may be related to a calcium imbalance in the cells due to an indiscriminate Ca^{2+} entry from the extracellular space or release from the internal stores. However, it is interesting to notice that this effect is restricted to the scanned plane. Indeed, sampling the volume of the scanned field of view along the z-axis, we observe no activation of the out-of-focus planes which preserve a basal level of fluorescence and activity. Thus, we cannot relate this activation (limited to the focused plane) to a permanent damage resulting in sample death. Indeed, in other experiments (for example in the long-term measurements performed for the whole volumetric recordings shown in the previous chapters), some times we observed an activation quickly spreading to all volume followed by neurons loss of function, a clear evidence of death of the larva, presumably due to sample overheating caused by the long scanning times. These two effects are undoubtedly not connected with each other, since the larvae in which we observe FOV "activation" as shown in Figure 46 were perfectly viable and, as highlighted above, suitable for functional imaging on all other planes. So, we wanted to investigate the biological events underlying the confined activation we observed. The nature of GCaMP makes it very favourable for this aim, since it allows to both label targeted neurons and follow their functional dynamics. As mentioned above, given the nature of two-photon imaging and genetically-encoded calcium reporters, we presume that the activation of the raster scanning area is related to an intracellular calcium leading to the increase of GCaMP green fluorescence intensity. Reasons behind this effect are surely to be related to the power employed in two-photon imaging leading to perturbative effects over certain levels. It is known, in fact, that the same laser used for two-photon imaging can be employed in laser ablation experiments confining the effect deriving from high-power irradiation to individual neurons chosen as targets. This approach is usually employed to dissect neuronal circuits based on targeted neurons loss of function and on the observation of the behaviors underlying them. In its more typical definition and application, laser ablation leads to the physical destruction of the irradiated targets, via physical mechanisms such as those described in Introduction. Since the activation we observed was restricted

to the irradiated area without inducing generalized sample and/or cells damage, we wanted to investigate if it could constitute the basis for a non-destructive perturbative approach alternative to classic laser ablation but yet still able to confine the effects of laser power at the single cell level. Laser irradiation effects depend, in fact, nonlinearly on several factors, mainly laser pulse frequency, power, and irradiation time. An example of a disruptive method deriving from high-power irradiation is shown in Appendix Figure A3. In the example shown we picked for target Rohon-Beard (RB) spinal cord neurons (mechanosensory neurons; [147]). High power and long irradiation time led to a damage in the target cell and in the neighboring area (Figure A3, 0') followed by cavitation bubble formation in the selected cell (Figure A3, 5' and 10'). This effect is clearly attributable to the damage induced by laser ablation. The effectiveness of the method thus requires the exploration of the optimal parameters to induce an effect restricted to the targeted cells without affecting the neighboring neurons and avoiding generalized sample damage. Since the approach we developed is distinguished from laser ablation and leads to a perturbation of neuronal calcium levels (and, thus, presumably, of neuronal activity), we will term this phenomenon GCaMP Laser-Induced Neuron Perturbation (GLINP). Beyond the laser irradiation parameters employed, another important aspect to be considered regards the localization of the calcium indicator. We never observed an activation comparable to that shown in Figure 46 (where GCaMP6s is expressed at cytoplasmic level) in samples expressing the nuclear-localized H2B-GCaMP6s, but rather the occasional massive activations of the whole larva brain, occurring with its death. Indeed, a comparison between cytoplasmic and nuclear localized GCaMP irradiation can produce interesting insights. In light of this observation, we wanted to test the effect deriving from the irradiation of the cell's nucleus in samples expressing the calcium indicator at the nuclear level (i.e. the H2B-GCaMP6s construct used in the previous chapter for functional imaging). We found that performing a line scan in correspondence of the nucleus produced a well localized photobleaching effect (Figure 47): just after the irradiation procedure, we observed a loss of fluorescence in the irradiated area (visible as a dark line; Figure 47, 0'); at subsequent times we assist to a slow recovery of fluorescence in the irradiated area. The recovery is similar to what is observed in standard FRAP (Fluorescence Recovery After Photobleaching) experiments: in this case, the diffusion of

H2B, albeit slow, can explain redistribution of GCaMP molecules, leading to recovery of fluorescence. In the frame acquired immediately after irradiation, in addition to the bleached line, we can also observe an increased fluorescence GCaMP on the nucleus compared to the previous frame. This indicates that some [Ca^{2+}] increase has taken place during irradiation but this effect quickly dissipates and is not visible in the subsequent frames.

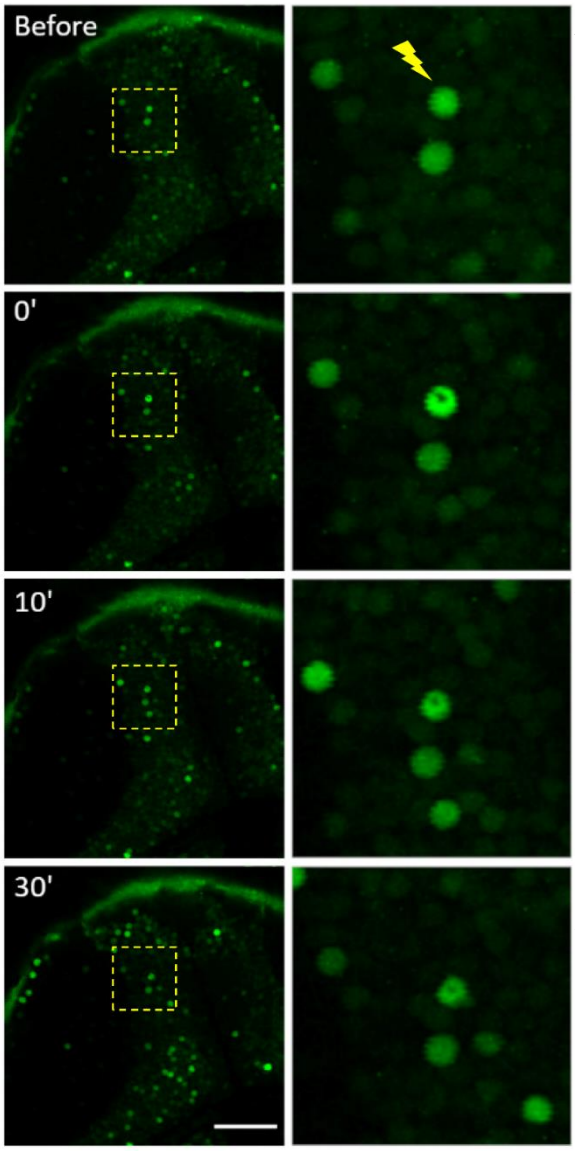

Figure 47. Irradiation inside the nucleus.

The panels show an optic tectum plane of a 4 dpf zebrafish larva expressing the nuclear-localized calcium indicator H2B-GCaMP6s. The insets on the right are magnified views of the yellow dashed square highlighted in the left panels. We performed a line scan in the nucleus applying a power of 20 mW/cm^2 (the neuron targeted for inactivation is indicated by the yellow lightning in the upper inset) and monitored the resulting effects at different time intervals (0, 10, 30 min later). Just after the irradiation procedure (0') the increase of fluorescence intensity in the selected neuron is associated with photobleaching in correspondence of the irradiation site (visible ad a dark line in the irradiated nucleus). In the panels sampled 10 and 30 min after irradiation we observe a slight recovery of fluorescence in the bleached area and a return to normal fluorescence in the rest of the nucleus. Scale bar: 50 µm.

Nucleus irradiation, in fact, does not perturb the neuron cell membrane nor the internal compartments membranes to a significant extent, so that no long-term consequence on the intracellular calcium levels and therefore no fluorescence intensity increase are observable. The difference observed in the effects of high-power irradiation between cytoplasmic and nuclear GCaMP suggests that irradiation close to the plasma (and/or inner organelles) membrane is responsible of GLINP. To corroborate the hypothesis described above, we thus employed samples expressing the cytoplasmic-localized GCaMP6s and proceeded testing different laser irradiation parameters restricting the procedure to a single cell. We performed a line scan spanning the cell membrane using an irradiation power of 20 mW/cm^2. As shown in Figure 48, after the irradiation procedure an increase of fluorescence intensity is observable, thus corroborating our hypothesis that such fluorescence increase is directly related to a calcium imbalance in the cell presumably due to membrane optoporation (effect not visible in nucleus irradiation). However, in this case the activation effect occurs in a cluster of neurons next to the one selected for irradiation. Being a manual procedure and being the neurons in the larval encephalon tightly packed together, it is possible that while performing the line scan in correspondence of the target cell membrane we also affected the neighboring neurons and/or their projections, resulting in an increase of fluorescence intensity in that cluster (Figure 48).

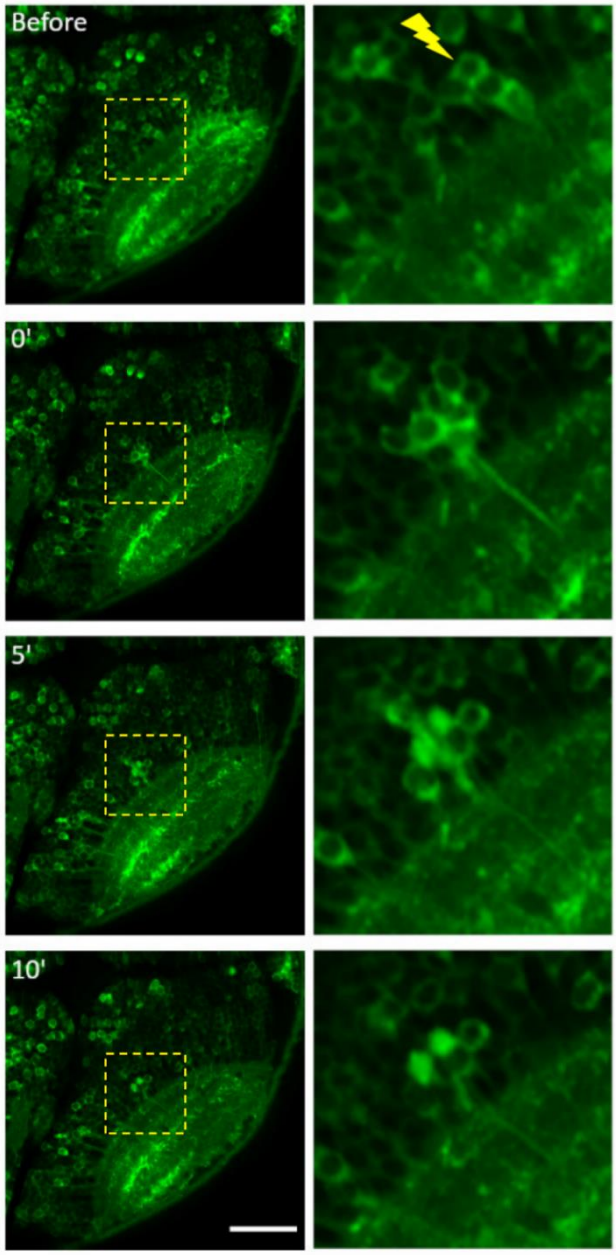

Figure 48. Permanent GLINP effect.

The figure shows the effects derived from irradiation of the cell membrane at high power (20 mW/cm^2) sampled at different times (before and 0', 5' and 10' after the irradiation). The panels on the left represent the imaging field of view (an optic tectum plane of a 4 dpf larva) and the insets on the right are magnified views of the irradiated neurons (highlighted by the yellow dashed square in the right panles). The upper inset shows the cell targeted for irradiation indicated by the yellow lightning. We sampled the consequences of the irradiation procedure at different times (0', 5' and 10' later) during which it is possible to observe a gradual increase of fluorescence intensity in the target neuron and in other cells next to it. This effect is visible just after the irradiation (0'), followed by a generalized increase of fluorescence in the whole area of the two neurons (5') which remain active in time (10'). The effect of irradiation at high power thus results in a permanent fluorescence increase. Scale bar: 50 µm.

We thus associated this effect to a permanent perturbation without any visible damages, as usually occurs in laser ablation experiments leading to cavitation bubble formation and damage in the ablated site. We tried to confine the irradiation procedure with more precision to a single cell, adjusting the length of the line scan to ensure irradiating as much as possible only the cell membrane of individual neurons, avoiding potential side effects on neighboring neurons. We tested the same irradiation power described above and in this condition we were able to obtain laser-induced perturbation on a single neuron. As a result of performing irradiation with optimized line-scan, we observed a massive fluorescence increase limited to the targeted cell, which spread to its axons and dendrites allowing to resolve its projections to the tectal neuropil. It should be noted that before irradiation the selected cell was barely visible and offered no possible chance to dissect its connections, especially in the neuropil. Indeed, the neuropil itself is the brain region consisting of mostly tangled dendrites and axons and the attempt to dissect them at the level of individual cell types is an issue difficult to address, without recurring to electron microscopy, as highlighted in the previous paragraphs Performing high-power irradiation on individual neurons thus enabled optical highlighting of their projections up to the tectal neuropil, an effect clearly visible immediately after the irradiation (Figure 49, 0') and still 10 minutes later (Figure 49, 10'). In the conditions of the experiment shown, however, after 30 minutes only the cell body maintains high fluorescence, while its axons and dendrites are no longer detectable (Figure 49, 30'). This suggests that in the conditions tested we were able to induce a long-lasting GLINP effect limited to the selected cell with the possibility to decipher its projections within a certain time interval (in these conditions we observed within 30 min). Similar results were obtained in the spinal cord, where the presence of bigger and less densely packed neurons compared to the tectal ones allows to better appreciate this effect. Also in this case the high-power irradiation of the cell membrane is followed by an irreversible perturbation restricted to the target cell (see Appendix Figure A4). The results thus far shown demonstrate the possibility of modulating the effects induced across the membrane of the neuron by laser irradiation. A plausible explanation of these observations is that passage of the laser at high-power on the cell membrane induces optoporation or analogous phenomena leading to a transient permeabilization and Ca^{2+} entry.

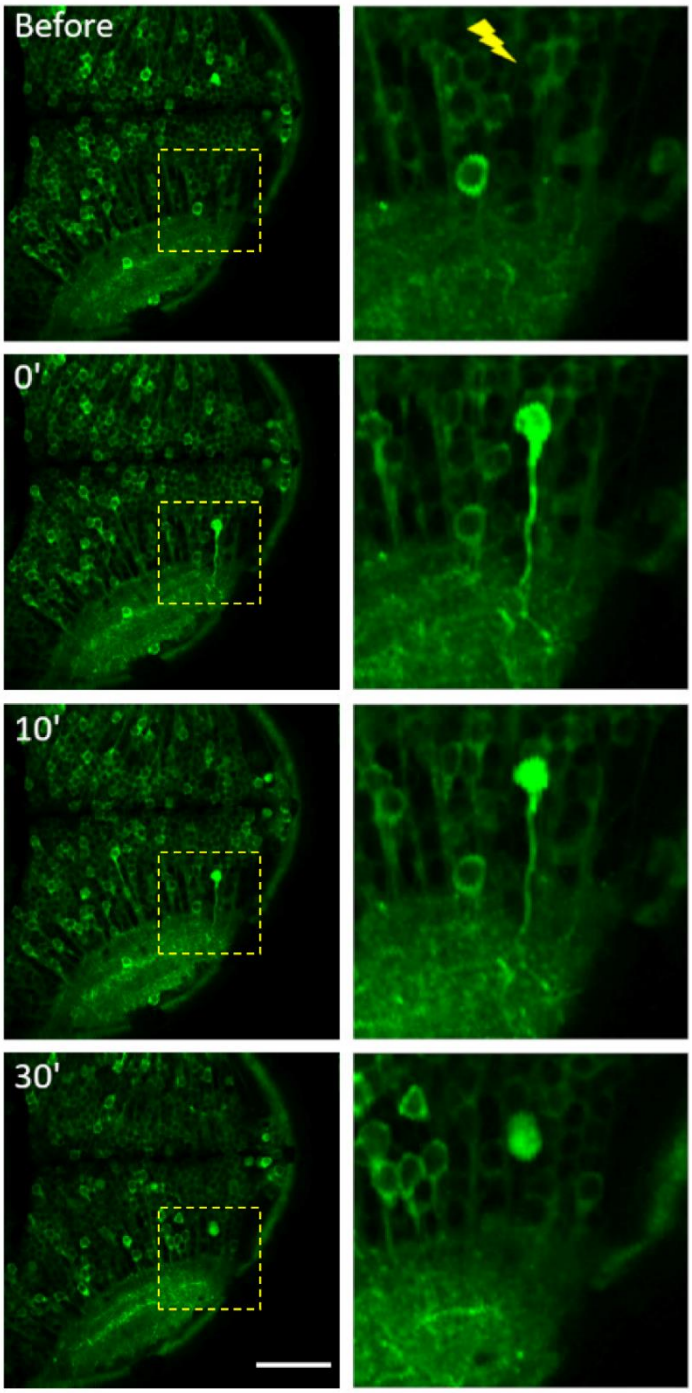

Figure 49. Localized long-lasting GLINP.

We employed high irradiation power 20 mW/cm^2 to perform a line scan in the cytoplasm of the neuron indicated by the yellow lightning. It should be noted that before the irradiation the selected neurons is barely visible. After the irradiation procedure (0') a huge increase of fluorescence intensity is visible, highlighting the neuron process up to the tectal neuropil. This activation is visible also 10 min later. Monitoring the irradiation procedure effects 30 min later a fluorescence increase of the selected cell is still visible; however, it is no longer possible to resolve its processes, probably as a consequence of the laser power parameters employed causing only a moderate imbalance of cellular [Ca^{2+}]. This effect is limited to the irradiated cell without affecting the neighbouring neurons. Scale bar: 50 µm.

Depending on the entity of the membrane damage, the cellular Ca^{2+} homeostasis systems might remain intact or be compromised, leading to recovery or permanent effects, respectively. This would mean that there is room for a very fine tuning of the GLINP effects based on irradiation power and scan parameters (such as shape, number of repetitions and so on). Based on these considerations and the observation of conditions (Figure 49) in which irradiated targets remain perturbed only within a finite time interval (presumably due to the laser power parameters adopted), we tried to reduce the irradiation power to 14 mW/cm^2 and to investigate the following effects in time. As a consequence of irradiation, also in this case an increase of fluorescence intensity occurs in the targeted neuron (Figure 50, 0'). However, this effect lasts just few minutes and already 10 minutes later it is possible to observe a recovery of a baseline fluorescence level comparable to that observed before the irradiation procedure (Figure 50). Figure A5 shows similar results in the spinal cord. Sampling the effects of low-power irradiation procedure at different time intervals we observed, also in this case, a temporary perturbation in the irradiated cell and a recovery of the initial fluorescence intensity levels already 5 minutes later (Figure A5). The bottom panel of Figure A5 shows the average fluorescence intensity measured in the target neuron before and 0, 5, 10, 15 minutes after the irradiation. It is then clear that the use of lower power induces a temporary perturbation in the target cell. Based on the different conditions tested, we can distinguish two different situations: an irreversible perturbation induced by high power irradiation, which will be suitable for structural/morphological mapping by optical highlighting of neuronal processes and connections; and a reversible perturbation, particularly appropriate for neuronal circuits functional mapping. These all-optical tools may thus be used as a starting point for deciphering the structural and functional connections among the spectrally-responsive neurons we mapped in the work described in the previous chapter.

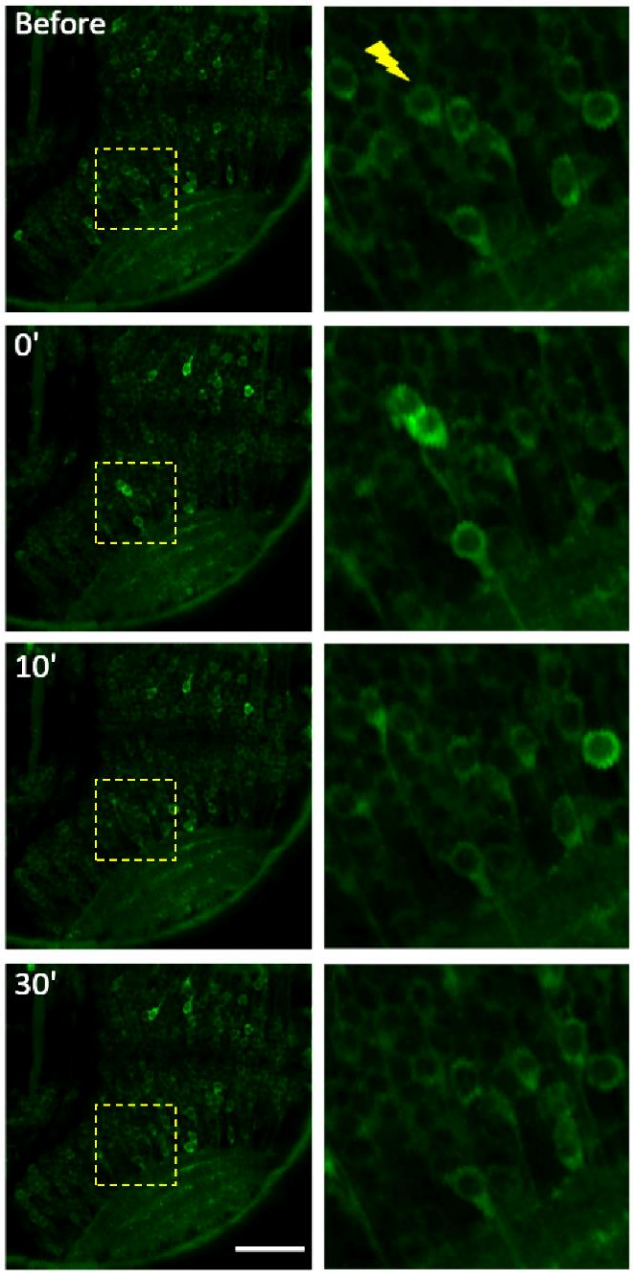

Figure 50. Reversible perturbation.

The panels show an optic tectum plane of a 4 dpf larva expressing the cytoplasm-localized calcium indicator GcaMP6s (left panels) and magnified view of the targeted neuron (right panels). Imaging has been performed at different times (before irradiation and 0, 10, 30 min after irradiation). The figure shows the effects we observed by employing 14 mW/cm^2 power. The selected neuron is highlighted by the yellow lightning in the upper inset. Just after the irradiation procedure (0') an increase of its fluorescence intensity is visible. This effect lasts few minutes and 10 min later the cell recovers the initial condition. Also at 30 min the cell shows no effect of the irradiation, indicating that lower irradiation power leads to a reversible and localized perturbation. Scale bar: 50 µm.

4.10.1 Temporary perturbation of spectrally-responsive neurons

We next tested and characterized the temporary perturbation effects in relation to spectrally-evoked responses. We employed transgenic larvae at 4 dpf expressing the cytoplasmic-localized calcium indicator GCaMP6s and chose as target for two-photon irradiation optic tectum neurons responsive to long-wavelength light flashes matching the absorption peak of zebrafish L cone type (580 nm). Neuronal activity was imaged with a custom-built two-photon microscope for 80 s during visual stimulation with five red flashes (100 ms duration and 1mW/cm^2 power). For the identification of the responsive neurons we implemented linear regression pixel-wise analysis following, with modifications, the method described in Miri et al., 2010 [136], as reported in the methods section. It should be noted that the choice of nuclear-localized H2B-GCaMP6s for the measurements reported in paragraphs 4.1 - 4.8 made segmentation and subsequent analysis at single neuron level much more readily implementable that the cytoplasmic GCaMP which produces images where the adjacent neurons touch each other and it is much more difficult to segment them. On the other hand, as demonstrated in the previous paragraphs, the GLINP concept works best with cytoplasmic GCaMP. For this reason, we performed analysis at pixel level rather than at cellular level. This analysis produced a T-score map, which allowed us to quantify the responsiveness to the spectral stimuli (as highlighted by the false color T score map shown in the bottom panel of Figure 51C). After identification of the responsive neurons, we then irradiated the cell membrane of one of the responsive neurons identified (applying the same line scanning procedure and irradiation power described above) and sampled the trend of the fluorescence intensity and neuronal activity in the whole FOV at different time intervals (0, 5, 10, 15 and 30 min later). Figure 51 shows a representative example of this experiment. Laser irradiation of the selected responsive neuron (characterized by high T score levels as shown by the T map in Figure 51A) led to its perturbation (as also demonstrated in the example in Figure 51) visible, just after the irradiation procedure, as an increase of fluorescence (Figure 51B). Fluorescence then returns to the initial levels already 15 minutes later (Figure 51C). We thus wanted to

investigate the effects of this reversible perturbation in relation to the neuron spectral response. Looking at the T maps shown in Figure 51, it is possible to observe a drastic reduction in T score values (from ~13 to ~4) after the irradiation (Figure 51B, bottom panel) followed by a gradual recovery toward the initial higher T values (Figure 51C, bottom panel). Variation in T score values points out how laser irradiation procedure affects neuron spectral responses. Observation of the fluorescence time traces before and after the irradiation procedure, in fact, demonstrates a temporary loss of response to the spectral stimuli followed by a gradual recovery of stimulus-evoked activity. Before the irradiation, it is possible to observe a response peaked after the five stimulus repetitions (Figure 51, orange trace). The increase of fluorescence in the irradiated cell is associated with a loss of response to visual stimuli (Figure 51, green trace). This effect lasts only few minutes since, together with the recovery of the initial fluorescence intensity levels, the cell gradually resumes its response to the spectral stimulus (Figure 51, violet trace). Figure 51D shows the average intensity sampled in the target neuron at the different time intervals after the irradiation procedure compared with that measured in an adjacent responsive neuron used as control (i.e. not selected for GLINP). The plot clearly shows the increase of fluorescence occurring in the target neuron after the irradiation and the subsequent recovery of the initial intensity levels. The neuron picked for control, on the other hand, shows a baseline fluorescence intensity during all time intervals tested independently from irradiation of the close neuron. Time course of the inactivation and subsequent recovery is shown in Figure 51E, where the different peak amplitudes of the responses sampled at different time intervals provide a better characterization of this effect. Another observation is that the perturbation is strictly limited to the targeted cell, without affecting stimulus-evoked responses and fluorescence intensity levels of the neighboring neurons. The graphs in Figure 51 (black traces) show examples of fluorescence time traces of a responsive neuron (highlighted by the red arrow in Figure 51A) localized next to the irradiated one and whose activity is not affected by irradiation confirming that, in the condition tested, irradiation induces a localized and reversible loss of function restricted to the cell targeted for irradiation. This approach represents a powerful tool for inducing functional perturbation aiming at the investigation of the local connectivity. The data shown in this thesis

represent preliminary results aiming to demonstrate the effectiveness of this method in inducing a reversible inactivation of selected cells without permanent damages and without affecting their capability to later resume visually-evoked activity. This method could thus lead to the development of a technique alternative or complementary to optogenetics without the need to express light-sensitive ion channels but rather taking advantage of GCaMP dynamics and spectral properties to perform combined functional imaging and optical perturbation.

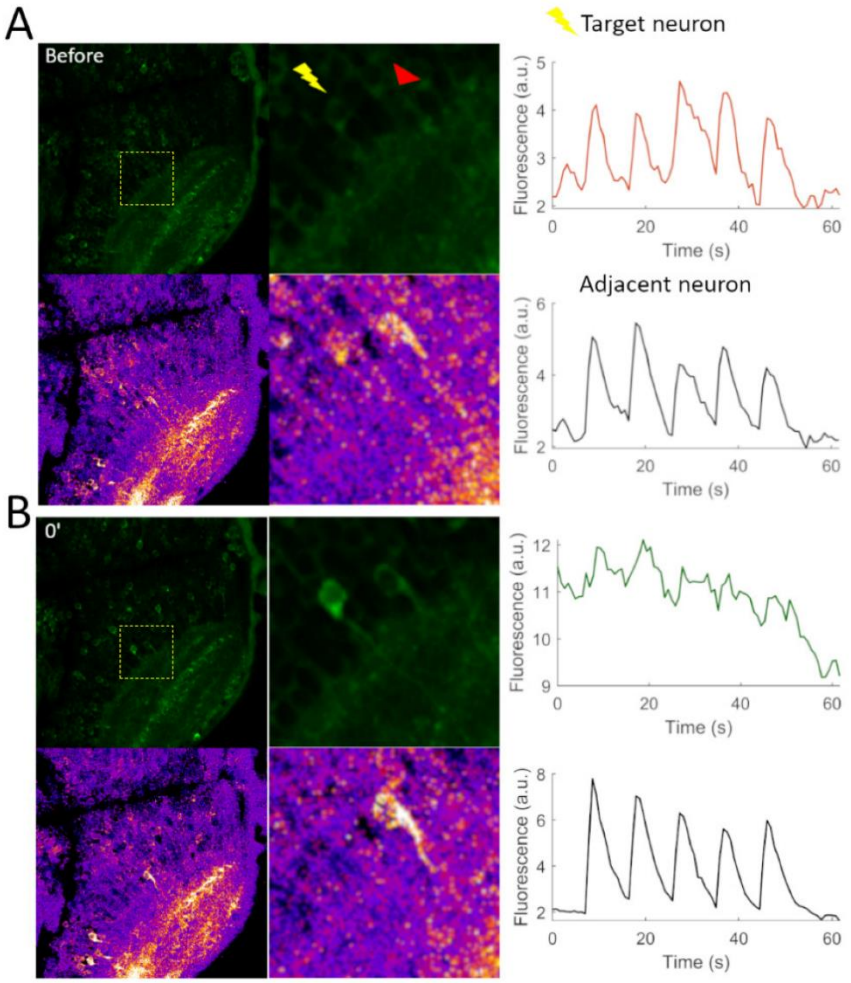

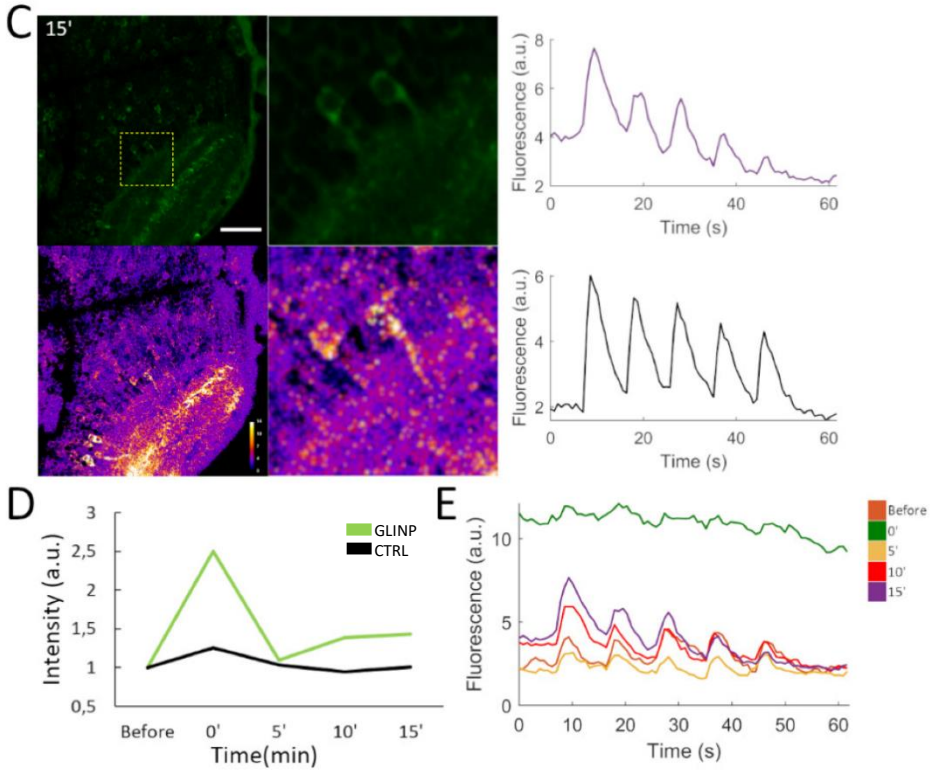

Figure 51. Temporary inactivation.

Maximum intensity projections (top left) and T-maps (bottom left) of an optic tectum area of a 4 dpf Tg(elavl3:GCaMP6s) larva. **(A)** Based on T-score, the neuron indicated by the yellow lightning in the upper inset was targeted for irradiation. The right insets are magnified views of the of the lefts panels (the enlarged area is highlighted by the yellow dashed square). The graphs on the right show GCaMP fluorescence recordings during visual stimulation with five red flashes; measurements were performed on the neuron targeted for inactivation (colored traces) and on an adjacent neuron (black traces) not irradiated (highlighted by the red arrow in the inset). Before the irradiation the targeted neuron is responsive to the visual stimuli as shown by the fluorescence time trace and by the high T values. The false color map (with the scale shown in the bottom panel in C) quantifies the level of responsiveness to the visual stimuli. **(B)** The effect of irradiation is shown immediately after (0') resulting in an increase of fluorescence intensity in the targeted neuron associated by a loss of response to the visual stimuli as demonstrated by the T values decrease and the fluorescence time trace (green trace). However, the neighboring neuron was not affected by the irradiation procedure and continues responding to the stimuli (black trace). **(C)** Fifteen minutes (15') after a recovery of the fluorescence intensity, T score levels and response to visual stimuli is visible. The data show reversible inactivation limited to the target neuron, whereas the visual response of the neighboring neuron is not affected by this procedure. Scale bar: 40 µm. **(D)** Normalized average intensity sampled before and 0, 5, 10, 15 minutes after the irradiation

in the neuron targeted for GLINP (green trace) and in the adjacent neuron (black trace). **(E)** The graph shows time course of inactivation before and after 0, 5, 10, 15 min pointing out the inactivation and subsequent recovery of activity (already 5 min after) of the irradiated neuron.

4.11 Optical highlighting

As highlighted previously, control of irradiation parameters modulates the perturbative effects between short-lived reversible and long-lasting irreversible effects. The latter may be used to trace the processes of the irradiated neuron in 3D in the tectal neuropil, due to an increased fluorescence throughout the cell dendrites and axon, as shown in the example above. We used this approach to demonstrate the possibility of reconstruction of the projections of several neurons in the optic tectum neuropil. We irradiated different tectal neurons in sequence and took advantage of the irreversible fluorescence increase induced by high power irradiation in the targeted cells to resolve their axons and dendrites up to the tectal neuropil, clearly not visible before irradiation. We thus targeted different tectal neurons belonging to the same plane and followed the highlighting along the z-axis for 3D reconstruction. In post-processing we produced for each z-stack a maximum intensity projection and difference images to label each target cell with different colors based on the temporal sequence of irradiation to better appreciate and distinguish the projections of each irradiated neuron in the total volume sampled. Figure 52A show a GCaMP maximum intensity projection of an optic tectum plane of a 5 dpf larva recorded before high-power irradiation. Figure 52B-D are maximum intensity projections of the same plane after high power irradiation of three different individual neurons (neurons #1-3 in Figure 52A). Looking at the image sequences, it is possible to observe the localized massive activations of each of the irradiated neuron and of their neurites. To provide a better contrast and mapping of these cells, we produced difference images obtained by the subtraction of each image with the previous according to the temporal sequence of irradiation (Figure 52E-G). We thus labeled each irradiated cell with individual colors to better highlight the projections of their axons and dendrites to the neuropil and possible connections (Figure 52H). This strategy represents a powerful tool for morphological

reconstruction of targeted cells by optical highlighting. Figure 53 show some examples of such optical highlighting in several neurons by comparing the same plane before and after irradiation and labeling them with arbitrary colors for a more suitable morphological mapping. The advantage of this method is that we were able to irradiate individual cells (no effects on surrounding neurons are visible) and, since it induces effects lasting in time (irreversible effect), it was possible to irradiate multiple cells in sequence to dissect potential neuronal connections.

By the results shown in this chapter we can assume that the cytoplasmic GCaMP6s can be specifically used to cause either reversible (employing lower power parameters) or irreversible (targeting the cell membrane with high power) cellular calcium imbalance, visible as an increased level of fluorescence. The first may be employed as a perturbative approach in order to induce a temporary loss of function in neurons responsive to different types of stimuli, for example spectral stimuli in the example shown, whereas the latter to provide a structural reconstruction of such responsive neurons thus investigating their local connectivity. This approach thus opens the way to a detailed investigation of the connectivity patterns among spectral responsive neurons with the possibility to observe how the irradiation of specific cells affect the spectral responses of others belonging to the same or different circuits.

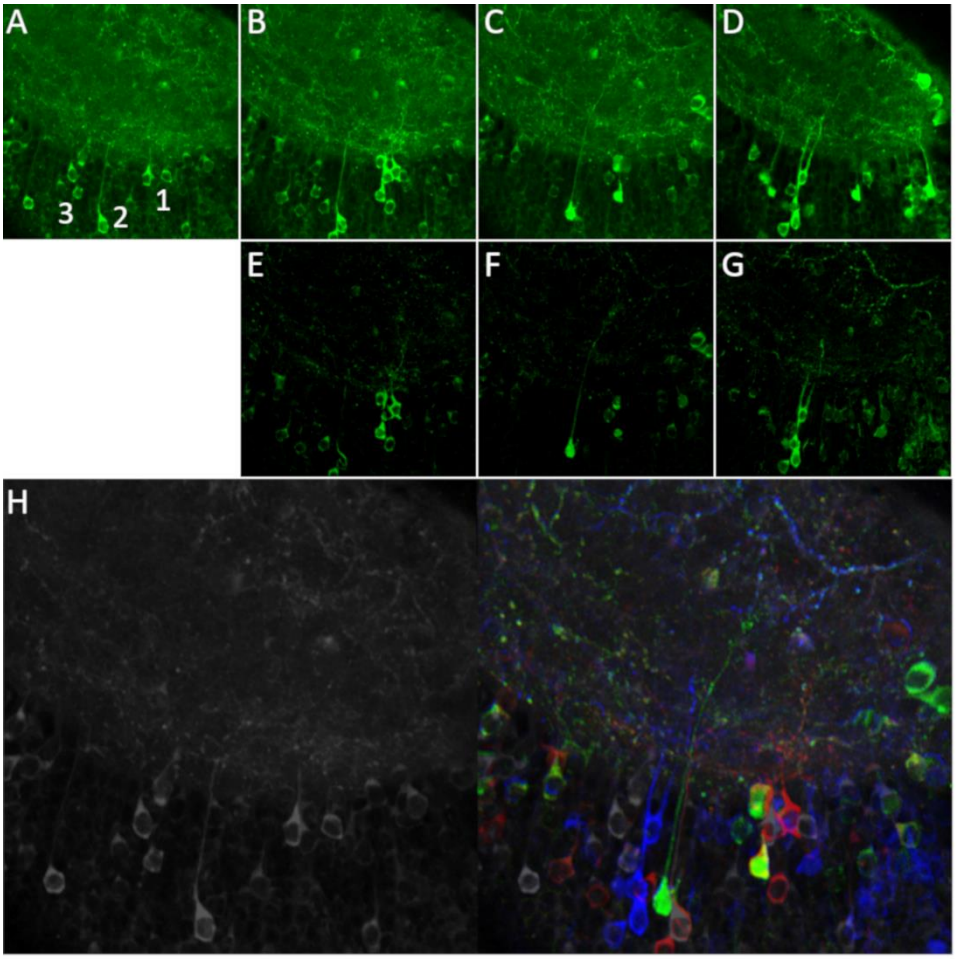

Figure 52. Optical highlighting.

(A) Maximum intensity projection (MIP) of an optic tectum plane of a 5 dpf Tg(elavl3:GCaMP6s) larva. The numbers 1-3 in the figure highlight the neurons targeted for the three separate and subsequent irradiations. **(B)** MIP of the same plane shown A after the irradiation of the neuron #1 visible as an increase of its fluorescence intensity. **(C)** After the irradiation of neuron #2. The image shows a huge increase of fluorescence intensity in the targeted cell and a further fluorescence increase also in neuron #1, simply due to the dynamics following its own irradiation. **(D)** After the irradiation of neuron #3. The panel shows the activation of the three selected neurons. **(E-G)** The figures represent difference images obtained by subtraction between the irradiated plane and that acquired just before (E = B-A; F = C-B; G = D-C). **(H)** Left panel: same as A displayed in grey scale. Right panel: overlay of difference images E-G color-coded following the temporal sequence of each irradiated neuron (neuron 1- red, neuron 2-green, neuron 3-blue) highlighting their processes in the tectal neuropil. FOV 133x133 μm^2, resolution 0.26 µm/px.

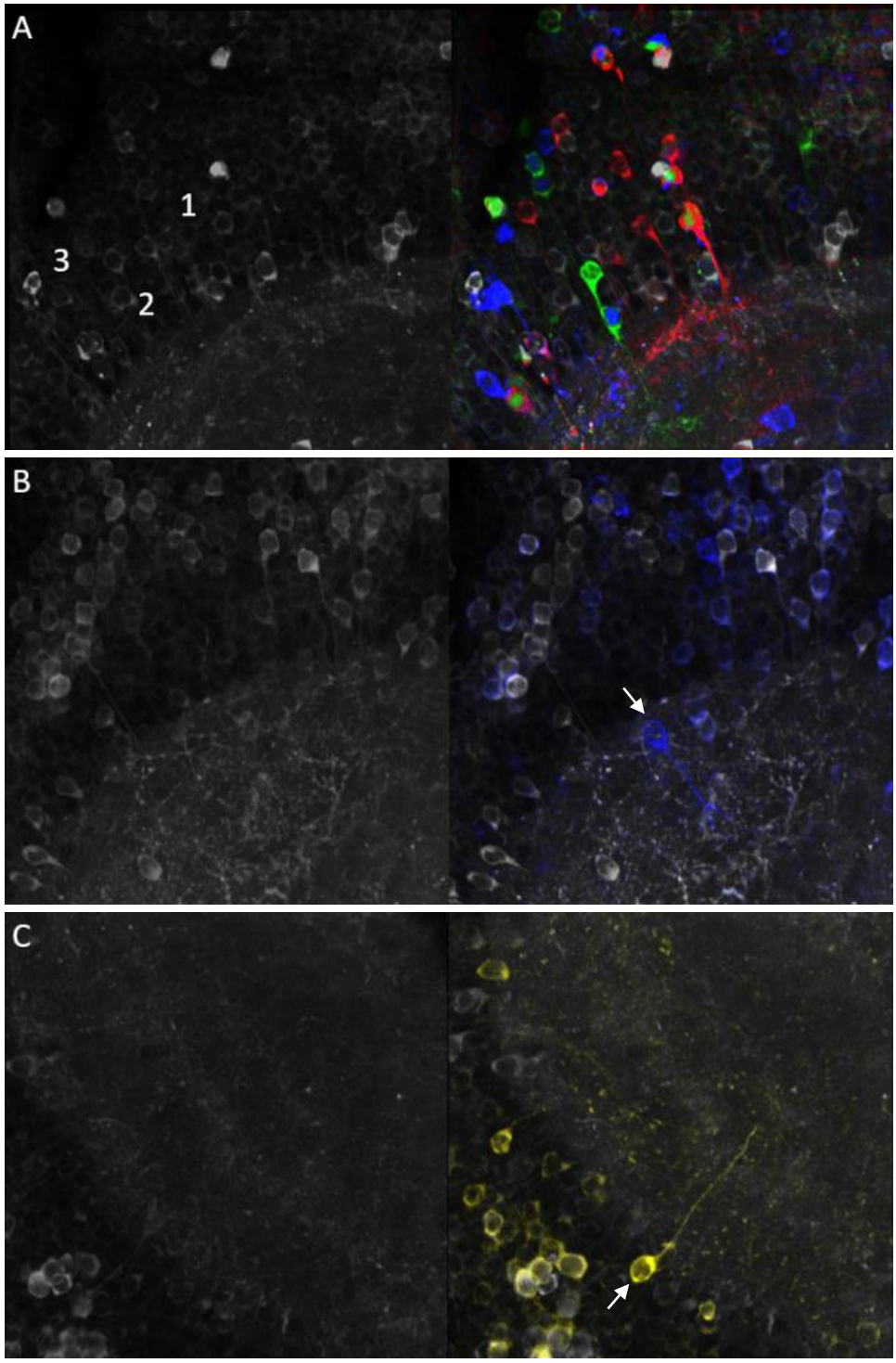
A
1
3
2
B
C

Figure 53. Optical highlighting.

(A) Maximum intensity projection of a 5 dpf Tg(elavl3:GCaMP6s) zebrafish larva before the irradiation procedure (left panel). The numbers 1-3 in the panel indicate the neurons selected for the serial irradiation procedure. Note that before irradiation the cells are barely visible. Right panel: overlay of irradiated planes showing the three irradiated neurons color-coded based on the temporal sequence of their irradiation (neuron 1- red, neuron 2- green, neuron 3-blue). The image highlights the irradiated neurons soma and axons projection up to the tectal neuropil, not visible before the irradiation procedure. **(B-C)** Other examples of optical highlighting before and after irradiation of a single neuron (indicated by the white arrows in the figures) labeled for a better visibility. FOV 133x133 μm^2, resolution 0.26 µm/px.

5. DISCUSSION

Understanding how the visual natural environment is perceived and how it influences the behavioral choices of most animal species, requires a detailed dissection of the information flow from the eye to the brain and of the processing occurring within the brain and leading to a response. Indeed, one of the most fundamental brain functions across all species is the ability to produce motor outputs depending on the animal behavioral requirements in response to integrated sensory inputs. This requires a complex integration between visual inputs and motor outputs in order to control the generation of precise movement patterns [61]. Indeed, one of the main challenges for understanding how brain generates behaviors is to investigate how visual and motor areas communicate each other. As a consequence, mapping the connectivity patterns underlying visually-evoked behaviors from the retina down to the most caudal regions, specialized in encoding motor variables specifically tuned to behavioral choices within a stimulus setting, is needed. This type of study requires a relatively simple and small brain, allowing imaging with enough spatial and temporal resolution to map neural activity at single cell and connections level in the whole brain. Among vertebrate models for vision, the zebrafish larva offers unique opportunities for obtaining a comprehensive understanding of the neuronal basis of visual behaviors at the synaptic, cellular, circuit and whole-brain levels [61]. This is due to its optical transparency and small brain volume (100000 neurons at 5 dpf; [7]), together with a highly developed visual system (which takes nearly a quarter of the larva total volume) and its wide behavioral repertoire [8-11], with a fundamental role played in the larva survival by visually-guided behaviors (such as predator escape and prey capture, just to mention the most crucial under an evolutionary standpoint). The first level of visual information processing occurs in the retina, where the presence of four spectrally-distinct cone types allows zebrafish to perceive and discriminate chromatic signals ranging from UV to red [14], providing a complex and information-rich map of its natural visual environment [29]. Spectral signals are integrated and processed across the different retinal layers before reaching, through Retinal Ganglion Cells (RGCs) axons, their targets in the brain (i.e. optic tectum (OT) and the other retinorecipient

areas (RAs)) where further processing occurs. In this context, during my PhD, we investigated how spectrally-distinct stimuli are propagated and integrated at different levels across the zebrafish larva central nervous system (CNS) up to the most caudal regions responsible of eliciting wavelength-dependent behaviors. We mapped spectrally-selective responses throughout the larva CNS encompassing the whole encephalon and part of the spinal cord. The development of the genetically-encoded calcium indicators, such as those belonging to the GCaMP-family, allowed real-time and non-invasive measurements of neuronal activity, given their high sensitivity to intracellular [Ca^{2+}] variations, which produce a variation of their fluorescence directly related to neurons spiking frequency and synaptic transmission. In this regard, the zebrafish larva is undoubtedly extremely well suited for functional imaging measurements, enabling to both label neurons in which the reporter is targeted with very efficient transgenesis techniques and then monitor their activity in the whole brain and at the single-cell level with the possibility to simultaneously present visual stimuli. Functional mapping requires, as a first step, a morphological reconstruction of neurons anatomical distribution and of their connectivity. Understanding the neuronal circuits underlying the spectrally-responsive neurons we mapped, thus requires a correlation between morphology and function to decipher their connectivity patterns and to study the associated color-evoked behaviors. Therefore, in this PhD thesis, I developed two approaches to tackle the problem of studying the processing of spectral information in the zebrafish brain: first I employed two-photon microscopy and calcium imaging during visual stimulation to produce a map of spectrally-tuned responses across the larval brain and spinal cord; second, taking advantage of GCaMP properties and functions, I developed novel optical methods based exclusively on the use of such indicator to implement both perturbative and highlighting strategies possibly exploitable for circuitry mapping and 3D reconstruction.

5.1 Spectrally-tuned neuronal responses

In this work, we mapped, with cellular resolution, spectrally-selective responses in the whole brain and part of the spinal cord of 3 and 5 dpf zebrafish transgenic larvae expressing the nuclear-localized calcium

indicator GCaMP6s (Figure 29). We implemented mosaic two-photon fluorescence imaging covering a volume of 1500x720x270 μm^3 encompassing the whole encephalon and about one quarter of the spinal cord of the larva, and measured neuronal activity during visual stimulation with light flashes with wavelengths centered on the absorption peaks of the four zebrafish retinal cones [23, 25, 26] (Figure 30). The use of IR light in two-photon microscopy, although not totally suppressing it, reduces the problem of direct retinal photoreceptors excitation [148], enabling imaging of neuronal activity with minimal interference with our protocol of visual stimulation. Spectrally-distinct stimuli elicit a strong and reproducible response in a subset of neurons of the larva CNS (Figure 31). We quantify such responses by linear regression and T score analysis. We observed that visual stimulation produces a very wide array of responses both quantitatively (i.e. the amplitude of response) and qualitatively (i.e. their spectral tuning to one or multiple wavelengths). Indeed, due to this variability, we found that there is no hard cutoff between a tail of high-amplitude spontaneous spikes and the low-medium amplitude visually-evoked responses. In fact, observation of the distributions in Figure 31 shows that experimental data are characterized by higher T values for each stimulus compared to the control ones, whose distribution falls to zero at T∼27. Identification of responsive neurons requires a choice of T threshold (T_{Th}) to exclude from our data spontaneous spikes (false positives). On the other hand, imposing a $T_{Th}>27$ would ensure a zero false positive rate (FDR) but, at the same time, it would increase the number of false negatives thus leaving out from the selection a significant fraction of actually responsive neurons (a schematic representation of the effects of T_{Th} on T distributions is illustrated in Figure 33). Based on the observation that the control distribution deviates from the experimental at T∼10 and, as mentioned above, it drops at zero at T∼27 (Figure 31), we decided to set the FDR at 1% imposing a $10<T_{Th}<27$. This ensured to select positive neurons with 99% confidence reaching a good compromise between false positives and false negatives. Indeed, the $\Delta F/F_0$ traces of the neurons selected with this criterion correlate strongly with the visual stimuli (as shown by the heatmaps in Figure 37 and Figure 39). Spectral characterization of neurons leads to the identification of single and multiple wavelengths responses (see for example the spectral column of Figure 37 and Figure 39). We characterized this aspect with the unique spectral

identifier Tbar and showed the most relevant spectral classes of neurons in Figure 40. Looking at Figure 21C, we notice that the four zebrafish cone types exhibit large overlaps of their absorption spectra. This is actually a fundamental evolutionary aspect for extending color perception through a wide range of wavelengths spanning the solar spectrum and providing the subjective perception of a continuum of colors depending on the light wavelengths. If we focus on the four wavelengths used for stimulation in our experiments, the figure shows that L_1, L_2 and L_3 produce excitation of multiple cone types, due to their spectral overlap. However, even considering this insuppressible cross-talk between some of our excitation sources and the broad cone absorption spectra, we notice that the most populated Tbar classes clustering neurons with responses to multiple wavelengths cannot be explained based on cross-talk. For example, neurons responding to both L_1 and L_4 must receive independent inputs from these two channels since there is no cross-talk between these two sources (see Figure 21C). We also assessed the robustness of the Tbar analysis by evaluating the emergence of the classes in a spectrally-unbiased analysis (shown in Figure 41). The data shown in Figure 41 demonstrate that single color classes are strongly populated across T_{4D} values and that these, as well as the multiple wavelength classes, emerge roughly with the same proportions even when lowering all the thresholds applied to a single value. This observation responds to an important caveat that should always be considered when applying thresholds: threshold analysis intrinsically imposes a compromise between false positives and false negatives and can never eliminate totally either of them (at least in the conditions highlighted by Figure 31). Our choice in this regard was extremely stringent, unavoidably leading to some false negatives (i.e. neurons actually responsive to the visual stimuli but not passing the threshold selection criterion, as exemplified by the graph shown in Figure 33), but at the same time ensuring the selection of neurons with very reliable responses across the CNS. Nevertheless, the identification of spectrally-selective responsive neurons in non-visual areas is one hand very interesting and, on the other hand, requires assessment of potential artefacts due to spontaneous motor activity. Given its random nature, in fact, spontaneous activity might introduce by chance some peaks at the timing in which the visual stimuli are presented in our measurements (see for example the $\Delta F/F_0$ shown in Figure 36A). As a consequence, regression analysis attributes to these

responses high T values which might be comparable to those attributed to three peaks of lower amplitude. In this way also one or two peaks of high-amplitude spontaneous activity might pass T threshold selection criterion for a given stimulus; indeed, these are the 1% false positives we accept. To avoid this, in addition to 1% FDR selection based on T thresholds, therefore, we implemented peak analysis to filter out the neurons not responding consistently to each of the three repetitions of the stimulus (see also materials and methods). Quantification of the effects of peak selection are reported in Table 2. Comparison between experimental (Table 2) and control (Table 4) data points out the effectiveness of peak analysis in filtering out peaks deriving from spontaneous activity. Indeed, since spontaneous activity introduces random peaks, the probability of them syncing with the times chosen for presenting the visual stimuli in the experiments scales with the power of n, with n being the number of repetitions of stimuli used in the experiment. Therefore, almost never will random peaks of spontaneous activity follow exactly the three stimulus repetitions. Thus, peak analysis operates a very robust selection against spontaneous activity, as demonstrated by our analysis. A clear example is shown in Figure 36A. The $\Delta F/F_0$ exhibits two high-amplitude peaks in correspondence of the timing of L_1 stimuli, so that regression analysis attributes to such response a T value above T_{ThU}. As a result, this neuron passes the T threshold selection criterion for L_1 stimulus, but it is filtered out by peak analysis (Figure 36B). This can be quantified by comparing the percentages of control neurons passing threshold with and without peak selection. By applying only threshold analysis we found 0.7%, 1.7%, 0.7%, 0.3% for L_1, L_2, L_3 and L_4 respectively (percentages are calculated with respect to the number of positive neurons from the stimulated data). These percentages are consistent with the 1% FDR selection imposed (the L_2 stimulus is statistically less robust than the others due to the lower number of responsive neurons to this wavelength). It is interesting to notice that these percentages drop to 0.3%, 1.7%, 0.3% and 0.08% after imposing peak selection, demonstrating that this analysis further reduces the number of false positives deriving from spontaneous activity.

	Encephalon			Spinal cord		
	Above T_{Th}	Above T_{Th} + Peak analysis	%	Above T_{Th}	Above T_{Th} + Peak analysis	%
L_1	38	17	44.7%	1	0	/
L_2	1	1	100%	0	0	0%
L_3	6	2	33%	0	0	0%
L_4	8	2	25%	2	1	0.5%

Table 5. Threshold analysis vs. peak analysis in controls.

The table shows quantification of responses attributed by chance to one of the four stimuli across the encephalon and spinal cord in control larvae recorded in absence of visual stimulation (N = 5 larvae at 5 dpf). The statistics reported in the table are cumulated over the total number of ROIs segmented over all larvae in our control experiments: 518409 (encephalon) and 70617 (spinal cord).

Clearly, the control data provides a good estimate of the characteristics of spontaneous activity, which we have to account for in the experimental data, where peaks of spontaneous activity will appear in the $\Delta F/F_0$ traces with comparable frequency and features. One demonstrative example is shown in Figure 36C-D. In this case, peak analysis leads to exclude from selection the L_4 responses (that do pass the T threshold selection) and thus consider this neuron responsive to only the L_1 stimulus. Looking at the $\Delta F/F_0$ trace, however, another consideration can emerge: L_2 (although under T threshold) and L_4 responses seem to both appear consistently in the first two repetitions of the stimuli, while they both fail to respond in correspondence of the third repetition. This is striking and it seems unlikely that it represents a coincidence, also considering that the $\Delta F/F_0$ trace highlights a robust response to both stimuli. Thus, it is possible that a sort of inhibition might be occurred. This is just an example to show the broad variability of combination of responses we found among the 100000 neurons of the larval brain. We have to consider that in this context the threshold analysis, although it is an effective method for responsive neurons selection especially in association with peak analysis, tends to leave out some response patterns which might have a biological meaning. However, in this work we have considered only those responses above T threshold for each stimulus and passing peak selection, so we could, as a first step, provide maps and discuss biological implications of data selected

with extreme robustness in mind. The robustness of the neuron selection methods applied is also demonstrated by example experimental traces (Figure 30C and Figure 40C), heatmaps (Figure 37 and Figure 39) and averaged traces (Figure 40A). One more aspect we wanted to analyze regards possible history-dependence effects of the stimulation protocol. Figure 43 shows that the majority of neurons do not change their spectrally identity with the order of the stimuli. Also the fluorescence time response of all selected neurons confirm the stimulus-triggered calcium dynamics based on the kinetics of GCaMP6s in our system. We should note that our choice of regressors unavoidably leads to selection of those neurons exhibiting this type of response while, for example, slower response neurons would be missed. Also, no discrimination between ON- and OFF-responses can be applied to our data, since the duration of our stimulus is much shorter than the response of the GCaMP6s itself. Based on the importance of visual cues already in larval stages and the consequent evolutionary investment on the processing of visual information, the numbers of positive cells we identified (representing about 2% of the total number of neurons in the CNS) might seem surprisingly low. However, it is important to consider the nature of the stimulus used in our experiments. Uniform illumination of the retina with monochromatic light would indeed produce a large amount of suppression in the retinal output, due to integration processes (for example, lateral inhibition) occurring in the retina itself [15, 52, 149, 150]. Our stimulus, on the other hand, can be assimilated to the perception of uniform illumination such as in phototaxis and chromatic preference experiments [27] and also in uniformly illuminated environments in general [53, 58, 64, 75, 151]. We should also note that, as discussed above, our threshold analysis has given priority to minimize FDR, unavoidably accepting a significant proportion of false negatives. Therefore, the percentage estimated is certainly an underestimate of the total number of neurons involved in response to our stimuli (as broadly discussed in results section). Another issue related to intra-retinal processing and contributing to reducing the number of stimulated neurons via signal suppression regards the intensity of the stimuli. In this work, we aimed at performing our measurements in a condition of saturation (1 mW/cm^2) for each color (see methods for further details) to reduce as much as possible sources of sample-to-sample variability (at least in regards to the experimental parameters under our

control). Undoubtedly, dependence of response distributions on intensity, ON/OFF-responses, color opponency, patterns, dynamics and direction of stimulus presentation are extremely interesting areas of future investigation. Also, a full understanding of the whole process of visual input and signal processing leading to visually-guided behaviors requires mapping activity in the whole CNS. Several works have been published dealing with either the retinal [29, 46-48, 60, 75] or the encephalic side [4, 56, 63-65, 152] of this story. In a recent preprint from the Engert lab [153] a double labeling technique was applied to measure activity in both Retinal Ganglion Cells (RGCs) and retinorecipient areas (RAs) of the encephalon. Given the advantages of zebrafish larvae for the study of neuronal activity correlates and circuits at the basis of vision and visuo-motor transformations, this is a very intense area of investigation. However, until now, "color" perception was tapped in just in a few works related to optomotor response [68], phototaxis [27] and retinal structures [29, 48, 60]. This was one of the main motivations for the work conducted in this thesis. Our work extended to the whole encephalon measurements of neuronal activity with single cell resolution showing, for the first time, the extent of spectrally-selective responses in all its regions. The anatomical maps shown in Figure 37 and Figure 39 highlight a high density of neurons responsive to L_1, followed by L_4 and L_3 radiation, while only a very small subset of neurons responding to L_2 stimuli. There are several reasons concurring to explain this observation. Firstly, we need to consider the high anisotropy of the larva visual system [29]. The position of our stimulation LEDs causes illumination of the dorsal-frontal region of the visual field, stimulating the *area temporalis* (also termed "strike zone") which is particularly rich in UV cones and UV-on circuits [29, 48] and is implied in prey capture [60]. In addition to UV, Zhou, Bear et al. [48] highlighted in this area of the retina strong responses also to red light, thus anticipating that the projections from the strike zone to the brain would mostly involve UV and red wavelengths, as we indeed observed. Secondly, it was demonstrated that UV cones develop first and are the most abundant in the larval retina, followed by blue and by the other cone types [14, 17, 18, 24, 154]. In addition to the direction of stimulation, we need to consider the nature of our stimulus: we performed brief (100 ms) flashes with narrow spectral band matching, as closely as possible, the four zebrafish cone types [23, 25, 26]. Uniform illumination and insuppressible spectral cross-talk

(occurring in all cases but L_4, see Figure 21C) elicits a high degree of processing within the zebrafish retina itself [14, 17, 38] before reaching the RGCs. RGCs are, in turn, the source of signal for the downstream encephalic neurons, which are the object of our measurements. Thus, rather than mapping the responses due to the activity of each cone type individually, we map neurons involved in the "perception" and processing of information which we may link to specific "colors" as "perceived" by the larva for the four spectra used in our stimulation. The pathway of visual information processing, starting from photoreceptors up to the RGCs, becomes functional at 70-74 hours post fertilization (hpf) and is necessary in establishing contacts with the optic tectum (OT) [17]. Connaughton & Nelson [50] demonstrated the capability of larval RGCs to spectrally discriminate light of different wavelengths, showing a prominent response to UV light. This capability was evident in zebrafish larvae starting from 5 dpf, explaining the strong UV response we observe at 5 dpf compared to 3 dpf larvae. A recent preprint from Engert lab [153] discusses the projection of spectral information from RGCs to RAs. Similarly to our findings, the authors report spectral responses outside the main visual brain areas (e.g. cerebellum and habenula), although not probing the whole brain and spinal cord like we did. Moreover, our results cannot be directly compared due to the different visual fields illuminated in these two works (dorsal retina in Engert's lab work [153] versus ventral retina in ours). The presence of neurons with spectral selectivity of response widespread throughout the brain is very interesting. In fact, in Teleosts the role of the OT and other mesencephalic regions as the main centers of integration and processing of sensorial information, including chromatic signals, is known [19], while the possible roles of other anatomical regions in processing visual information are less known. So, we envision neuronal circuit schemes in which the retinal information, relayed to the tectum and here integrated vastly with other visual and nonvisual stimuli, is transmitted to the downstream CNS districts for further processing and to elicit responses maintaining, as shown by our data, spectral specificity at single neuron level. It is known that sensorimotor transformations are produced by complex networks involving different neuron types distributed across multiple brain regions acting to generate a behavior. Naumann et al. [3] describe the neural circuitry underlying the OMR and point out the role of distinct neurons organized in the rostro-caudal direction to allow

propagation of the landscape motion information and consequent generation of a motor response. Similarly, our data indicate the presence of neurons whose response is triggered in a spectrally-specific manner throughout the larva CNS, thus indicating the presence of "color"-selective circuits with such extension. Thus, we can state that our maps possibly identify neurons which maintain a well-defined spectral identity and are on the pathway for generating "color"-dependent behaviors. In this regard, it was particularly striking to find spectrally-selective responses in some spinal cord neurons. Examining the spinal cord at 5 dpf, we observe a relevant number of neurons responding to L_1, L_2 and L_3 radiation but not to L_4 (Figure 39 C, F, I, L). A reasonable explanation could be associated with the visually-guided behaviors elicited by different wavelengths in zebrafish larvae. It is known that long-wavelengths contribute strongly to the OMR, while short-wavelengths elicit phototaxis [68]. Indeed, recent works have reported a strong UV avoidance both in larvae and adults, using phototaxis assays on larvae [27] and split tank assays in adults [126]. These behaviors can be most likely explained by the danger represented by strong UV light, particularly in the case of larvae, due to their transparency. In fact, we presume that the stimulation of UV cones will lead to the aforementioned avoidance reflexes, thus triggering a motor response visible in our experiments as activation of spinal cord neurons. The comparison of spectral maps of neurons responding to our stimuli at different stages of development shows a shift in the predominant response from red (at 3 dpf) to UV radiation (at 5 dpf), although there is a generalized lower density of responsive neurons in 3 dpf larvae (Figure 44). However, a direct comparison between 3 and 5 dpf larvae is not possible since at 3 dpf the larval visual system is still developing and the retina becomes fully functional by 72 hpf [17]. Moreover, important synaptic connections associated with the integration of color and spatial information start developing after 3 dpf, when an improved acuity in zebrafish larvae has been demonstrated [10, 17, 50]. In fact, the first visually-evoked responses such as escape behaviors appear between 68 and 72 hpf, while the first OKR between 72 and 80 hpf [8]. This is in accordance with the results obtained in 3 dpf larvae, where we found a negligible level of integration between the different wavelengths (in contrast to 5 dpf data). Furthermore, at 3 dpf we did not detect any neuron with spectral-specificity in the spinal cord, indicating that, at this early stage of development, the circuitries in

charge of carrying spectral information down to the spinal cord and, thus, possibly eliciting color-selective motor behaviors, are not yet functional. Another interesting observation from our maps derives from epiphysis. The zebrafish pineal gland is characterized by photoreceptors with different types of opsins and projection neurons [155-157], and it plays an important role in the regulation of the circadian rhythms. In this work, we observe some epiphysis neurons with strong negative values of T, especially for UV radiation, thus highlighting, at cellular level, the inhibitory effect of short-wavelength light on this organ (Figure 45). Different studies performed in other Teleosts and other vertebrate classes suggested that the pineal projection neurons show a direct sensitivity to light with an inhibitory response in the violet-UV range, and an excitatory response at medium-long wavelengths [158-160]. A recent study carried out on zebrafish [157] has highlighted the presence of a subpopulation of pineal projection neurons exhibiting an excitatory response to blue and green light whose activity is not modulated by RGCs. The inhibitory effect we observed in this work could be associated to a subset of neurons responding in an inhibitory manner to UV light. In this regard it is important to consider the spectral properties of the GCaMP indicator and its dynamics. It is known that GCaMP is highly sensitive to intracellular [Ca^{2+}] variations resulting in an increase of its fluorescence baseline intensity in consequence of an increase of such ion. Since [Ca^{2+}] changes are directly related to neuronal activity, we expect a fluorescence increase in stimulated neurons. However, given the presence of inhibitory responses in some pineal neurons, we can state that they are characterized by a high spiking frequency in resting conditions which decreases when a spectrally-defined stimulus is presented (effect associated with a decrease of fluorescence intensity). Differences between 3 dpf and 5 dpf clearly show that while visual and visuo-motor transformation circuits are still largely under development at 3 dpf, circadian-related sensory inputs are well in place and working in the pineal gland already at 3 dpf.

5.2 GLINP – an approach for optical perturbation complementary to optogenetics and laser ablation

The anatomical mapping of neuronal responses evoked by spectrally-defined stimuli across the larva CNS reported in this work provides an overall view of the populations of neurons involved, of their response types and complexity. The next step in understanding the roles of mapped neurons in producing different behaviours is represented deciphering the connectivity patterns existing among these neurons to correlate structure and function and to investigate how each part of the brain works, how these parts are connected and how the brain works as a whole. Not only for visual inputs but in general, this is one of the main challenges in systems neuroscience, requiring the development of novel technologies and approaches. However, despite of the wide array of strategies nowadays available, the comprehensive reconstruction of the network of elements and connections in a whole vertebrate brain (termed "connectome", [161]) is a daunting task. In this context, once again, zebrafish larva represents the most suitable vertebrate model allowing to tackle such challenge. Indeed, its easy manipulation, versatility and optical access enable the employment of all current circuit dissection techniques at their best. In light of this, with the attempt to dissect neuronal connections among the spectrally-responsive neurons mapped in this work, we developed a novel all-optical strategy allowing to either temporarily perturb or optically highlight targeted neurons, based exclusively on the use of the GCaMP calcium indicator. Although two-photon imaging is a non-invasive technique, when performed at high power it can cause permanent damages in the sample. In our observations on zebrafish larvae imaging of CNS with GCaMP6s we found conditions affecting sample vitality or inducing a long-lasting apparent neuronal activation (visible as a generalized increase of fluorescence) limited to the scanning area. The first occurs with a wave of activation spreading to the whole volume of the sample, leading to neurons loss of function and death of the larva (generally during long-term imaging measurements); whereas the latter phenomenon was observed as an activation restricted to the focus plane without affecting out-of-focus planes (still suitable for functional imaging recordings) or inducing generalized sample damage. Figure 46 shows an example of this effect.

With the aim to confine the observed high power effects to the single cell level, we developed a novel perturbative approach, which we termed GCaMP Laser-Induced Neuron Perturbation (GLINP). Being a non-destructive method, we distinguish it from conventional laser ablation known for inducing a permanent physical cell destruction (visible as cavitation bubbles formation in the ablated site) and subsequent loss of function [123, 124]. Laser ablation experiments are broadly employed in zebrafish to investigate the neuronal basis underlying specific behaviors. In this context the brain regions/neuronal circuits responsible for the wide array of larval visual behavioral repertoire have been vastly studied. Among the numerous experiments carried out in this field, laser ablation has been employed to demonstrate the role of Mauthner cells in affecting escape behaviors and in the execution of visually-evoked swimming patterns [125]. Temizer et al. [75], on the other hand, pointed out the importance of an intact tectum for looming-evoked escape behaviors, whereas Roeser and Baier [55] showed that retinotectal neuropil is not required for OKR execution. Naumann et al. [3] investigated the neuronal basis of OMR by laser ablation of the posterior commissure and arborization fields 6 (AF6), highlighting the loss of binocular integration and optic flow processing, respectively. These experiments led to the destruction of the ablated site and subsequent loss of function without the possibility to recovery the initial conditions and to perform function measurements. In contrast, our approach can induce different levels of perturbation according to the different conditions tested. In fact, setting up of these new tools required testing different irradiation conditions mainly laser pulse frequency, power, irradiation time, length of the line scan and subcellular localization of the calcium indicator. Regarding the localization of the calcium indicator, we found that the nuclear-localized H2B-GCaMP construct is not appropriate for GLINP experiments since nucleus irradiation does not induce long-term calcium imbalance (associated with a fluorescence increase), but rather a localized photobleaching effect followed by a gradual fluorescence recovery (Figure 47). This effect can be attributed to the histone H2B function. Since it is involved in the regulation of chromatin structure and function, it is possible that after nucleus irradiation a slow diffusion of such histone occurs in the irradiated area resulting in a redistribution of GCaMP molecules. We thus consider the cytoplasmic-localized GCaMP surely more suitable for GLINP. The

differences we observed lie on the structures targeted for irradiation and the subsequent biological effects. Indeed, we observed that a line scan in correspondence to the plasma membrane of the neuron triggers a localized and robust perturbation which appears as an increase of GCaMP fluorescence (Figure 48 and Figure 49). This indicates that some intracellular [Ca^{2+}] increase has taken place in the irradiated cell following the membrane optoporation (effect not observable in nucleus irradiation). The effectiveness of GLINP on neurons expressing the cytoplasmic-localized GCaMP was then demonstrated through the investigation and characterization of this procedure in regards to two further factors: the irradiation power and the length of the line scan. Since the larval brain is characterized by neurons highly packed together, and considering the microscope objective 3D PSF, it was very difficult to irradiate a single cell without affecting closely neurons and/or their projections. This is the case shown in Figure 48 where high power irradiation (20 mW/cm^2) led to the activation of a cluster of neurons next to the targeted one. To confine the effect with more precision to individual cells, we had to improve the technique by reducing the length of the line scan. As a result, the same power irradiation parameters allowed to induce a perturbation limited to the selected cell and, at the same time, to resolve its projections to the tectal neuropil, otherwise not resolvable (Figure 49). The data shown in Figure 50 and Figure 51 point out that high power irradiation parameters induce a long-lasting perturbative effect visible as an increased fluorescence lasting in time. This observation led us to assume that an alteration of the homeostatic mechanisms involved in calcium handling by the internal stores presumably occurred in the irradiated cells. However, at this moment, we based our interpretations on GCaMP properties (i.e. high sensitivity to intracellular [Ca^{2+}] variations) without considering the detailed mechanisms of the effects induced in the irradiated neuron. Figure 49 show the dynamics of our perturbation sampled at different time intervals (0, 5, 10, 30 minutes after the irradiation), demonstrating that the perturbation induced with a power of 20 mW/cm^2 persists over such interval of time. Decreasing power irradiation to 14 mW/cm^2 a completely different result has been observed. Figure 50 and Figure 51 demonstrate that in this condition GLINP effect appears immediately after the irradiation but subsequently the target cell recovers quite rapidly its initial condition (at least as seen by a recovery of the fluorescence baseline level).

This evidences that laser power can indeed perturb neuronal calcium state either in a reversible or in an irreversible (or at least long-lasting) way. Consistently with our results we thus employed the reversible perturbation to investigate how this procedure affects the spectrally-evoked responses; and the irreversible perturbation to optically highlight neurons axons and dendrites up to the tectal neuropil, otherwise impossible to resolve in resting conditions. Together, these two approaches represent an attempt to develop effective methods applicable to reconstruct the local connectivity with the only use of the GCaMP indicator. Regarding the temporary perturbation, we chose to test the approach targeting neurons responsive to L_1 stimuli (see methods section for a more detailed description of the stimulation protocol). Responsive neurons have been identified by applying a pixel-wise regression analysis and the resulting T-score maps allowed to quantify the responsiveness to the visual stimulus. Low-power irradiation of individual responsive neurons led to a temporary activation (consistently with the data shown in Figure 50) of the targeted cell, associated with a loss of responses to the visual stimuli. The experimental traces show no signal saturation insofar as the detector, so the lack of response could be due to either saturation of GCaMP with Ca^{2+} or lack of physiological response in the cell altogether. It will of course be interesting to investigate these possible explanations in future experiments. At present we can point out that both of them, anyway, represent a drastic impairment in neuronal signaling. The T-score maps shown in Figure 51 highlight very well this effect, pointing out a drastic reduction of T levels occurring in the selected cells after the irradiation procedure. The temporary effect of this procedure allows the cell to recovery its initial condition together with a gradually recovery of the spectral-evoked response already 5 minutes after the irradiation (Figure 51). The advantage of this approach consists in confining the effect to a single cell level without affecting the neighbor neurons (as demonstrated by the fluorescence time traces of a neuron localized next to the irradiated one). The same experiments have been repeated on different samples (N = 5 larvae at 4 dpf) and in all the conditions tested we observe a temporary loss of the spectral response and a gradual recovery starting 5 min after the irradiation (data shown in appendix, Figure A2). Limited to the analysis performed and to the low number of larvae tested we did not find other neurons whose T values dramatically decrease after the irradiation of a selected cell. We expected

that the perturbation of one or more neurons in sequence would affect the activity (activation or inhibition) of other neurons being part of the same or of other downstream circuits. However, we have to consider the limited FOV imaged mainly covering the half section of the optic tectum directly receiving from RGCs. Finding downstream neurons in the circuits affected by GLINP requires expanding such investigations to the whole brain; at this stage of development of the method one limitation to this stems from the rapid recovery of the initial resting state occurring after the irradiation procedure that, in the conditions tested, does not allow to change FOV to investigate the resulting effects downstream. Thus, at this moment, we were able to induce a temporary perturbation limited to individual tectal neurons. High-power irreversible irradiation, on the other hand, allowed to trace neuron projections in 3D up to the tectal neuropil. Representative examples are shown in Figure 52 and Figure 53, where it is possible to appreciate the robustness of this approach in dissecting structures barely visible. We thus benefit from the use of GCaMP without the need of labeling neurons with other probes or expressing light-sensitive ion channels as in optogenetics experiments [146, 162]. Within this context we were able to perturb more than one neuron in sequence with the attempt to resolve their local connections and at the same time without damaging the scanned FOV and/or the sample. Clearly further development of this technique would benefit from several validation experiments, including, for example, electrophysiogical assessment of the functional state of neurons in the different conditions of perturbation. The results shown in this thesis are preliminary results demonstrating the effectiveness of this innovative tool to both induce a reversible perturbation and to optically dissect neuron projections aimed at the study of morpho-functional relationships underlying neuronal circuits.

5.3 Conclusion

Color vision is a crucial aspect of world perception for most animals. Our measurements provide spectral and anatomical maps of neurons involved in color-driven responses in the zebrafish larva CNS. Besides the well-expected high density of responsive neurons in the visual areas of the mesencephalon (i.e. OT and other RAs, the brain regions specifically

involved in processing visual information and integrating it with other sensorial inputs), we found spectrally-defined responses also in all other areas down to the spinal cord. Thus, we evidenced neural pathways maintaining spectral information throughout the CNS. The zebrafish larva is a very simple model yet representative of vertebrate CNS organization, so we expect the paradigm of spectral information propagating through non-visual areas to be relevant in all vertebrates. These results open the way for a detailed dissection of the circuits responsible for different color-dependent behaviors. For this aim we developed novel optical approaches implementing both a perturbative and a highlighting strategy possibly applicable to circuit mapping, based solely on the use of GCaMP. The results shown in this thesis demonstrate the possibility to employ these methods to both induce a temporary loss of function in the responsive neurons followed by a rapid recovery of their activity and to optically reconstruct their connectivity pattern, by inducing a non-destructive long-lasting perturbation leading to optical highlighting of all the neuron's processes.

The work on spectral responses was recently published in BMC Biology:

Fornetto C, Tiso N, Pavone FS, Vanzi F: Colored visual stimuli evoke spectrally tuned neuronal responses across the central nervous system of zebrafish larvae. *BMC Biol* 2020, 18(1):172.

6. BIBLIOGRAPHY

1. Ahrens MB, Li JM, Orger MB, Robson DN, Schier AF, Engert F, Portugues R: **Brain-wide neuronal dynamics during motor adaptation in zebrafish**. *Nature* 2012, **485**(7399):471-477.
2. Panier T, Romano SA, Olive R, Pietri T, Sumbre G, Candelier R, Debrégeas G: **Fast functional imaging of multiple brain regions in intact zebrafish larvae using selective plane illumination microscopy**. *Front Neural Circuits* 2013, **7**:65.
3. Naumann E, Fitzgerald J, Dunn T, Rihel J, Sompolinsky H, Engert F: **From Whole-Brain Data to Functional Circuit Models: The Zebrafish Optomotor Response**. *Cell* 2016, **167**(4):947-+.
4. Portugues R, Feierstein CE, Engert F, Orger MB: **Whole-brain activity maps reveal stereotyped, distributed networks for visuomotor behavior**. *Neuron* 2014, **81**(6):1328-1343.
5. Chen X, Mu Y, Hu Y, Kuan AT, Nikitchenko M, Randlett O, Chen AB, Gavornik JP, Sompolinsky H, Engert F *et al*: **Brain-wide Organization of Neuronal Activity and Convergent Sensorimotor Transformations in Larval Zebrafish**. *Neuron* 2018, **100**(4):876-890.e875.
6. Dal Maschio M, Donovan JC, Helmbrecht TO, Baier H: **Linking Neurons to Network Function and Behavior by Two-Photon Holographic Optogenetics and Volumetric Imaging**. *Neuron* 2017, **94**(4):774-789.e775.
7. Naumann EA, Kampff AR, Prober DA, Schier AF, Engert F: **Monitoring neural activity with bioluminescence during natural behavior**. *Nat Neurosci* 2010, **13**(4):513-520.
8. Easter SS, Nicola GN: **The development of vision in the zebrafish (Danio rerio)**. *Dev Biol* 1996, **180**(2):646-663.
9. Brockerhoff SE, Hurley JB, Janssen-Bienhold U, Neuhauss SC, Driever W, Dowling JE: **A behavioral screen for isolating zebrafish mutants with visual system defects**. *Proc Natl Acad Sci U S A* 1995, **92**(23):10545-10549.
10. Clark DT: **Visual responses in the developing zebrafish (B*rachydanio rerio)***. Eugene, OR: University of Oregon Press; 1981.

11. Borla M, Palecek B, Budick S, O'Malley D: **Prey capture by larval zebrafish: Evidence for fine axial motor control**. *Brain Behavior and Evolution* 2002, **60**(4):207-229.
12. Masland RH: **The fundamental plan of the retina**. *Nat Neurosci* 2001, **4**(9):877-886.
13. Gestri G, Link BA, Neuhauss SC: **The visual system of zebrafish and its use to model human ocular diseases**. *Dev Neurobiol* 2012, **72**(3):302-327.
14. Meier A, Nelson R, Connaughton VP: **Color Processing in Zebrafish Retina**. *Front Cell Neurosci* 2018, **12**:327.
15. Baden T, Euler T, Berens P: **Understanding the retinal basis of vision across species**. *Nat Rev Neurosci* 2020, **21**(1):5-20.
16. Schmitt EA, Dowling JE: **Early eye morphogenesis in the zebrafish, Brachydanio rerio**. *J Comp Neurol* 1994, **344**(4):532-542.
17. Schmitt E, Dowling J: **Early retinal development in the zebrafish, Danio rerio: Light and electron microscopic analyses**. *Journal of Comparative Neurology* 1999, **404**(4):515-536.
18. Raymond P, Barthel L, Curran G: **Developmental Patterning Of Rod And Cone Photoreceptors In Embryonic Zebrafish**. *Journal of Comparative Neurology* 1995, **359**(4):537-550.
19. Burrill JD, Easter SS: **Development of the retinofugal projections in the embryonic and larval zebrafish (Brachydanio rerio)**. *J Comp Neurol* 1994, **346**(4):583-600.
20. Dowling JE: **The retina: an approachable part of the brain**: The Belknap Press of Harvard University Press, Cambridge, MA; 1987.
21. Connaughton V: **Organization of ON- and OFF-pathways in the zebrafish retina: neurotransmitter localization, electrophysiological responses of bipolar cells, and patterns of axon terminal stratification.** *Prog Brain Res* 2001, **76**:131:161.
22. Engström K: **Cone Types and Cone Arrangement in the Retina of Some Cyprinids 1234**. In., vol. 41:277-295: Acta Zoologica; 1960.
23. Robinson J, Schmitt E, Harosi F, Reece R, Dowling J: **Zebrafish Ultraviolet Visual Pigment - Absorption-Spectrum, Sequence, And Localization**. *Proceedings of the National Academy of Sciences of the United States of America* 1993, **90**(13):6009-6012.

24. Allison W, Barthel L, Skebo K, Takechi M, Kawamura S, Raymond P: **Ontogeny of Cone Photoreceptor Mosaics in Zebrafish**. *Journal of Comparative Neurology* 2010, **518**(20):4182-4195.
25. Cameron DA: **Mapping absorbance spectra, cone fractions, and neuronal mechanisms to photopic spectral sensitivity in the zebrafish**. *Vis Neurosci* 2002, **19**(3):365-372.
26. Govardovskii V, Fyhrquist N, Reuter T, Kuzmin D, Donner K: **In search of the visual pigment template**. *Visual Neuroscience* 2000, **17**(4):509-528.
27. Guggiana-Nilo D, Engert F: **Properties of the Visible Light Phototaxis and UV Avoidance Behaviors in the Larval Zebrafish**. *Frontiers in Behavioral Neuroscience* 2016, **10**.
28. Fadool JM: **Development of a rod photoreceptor mosaic revealed in transgenic zebrafish**. *Dev Biol* 2003, **258**(2):277-290.
29. Zimmermann M, Nevala N, Yoshimatsu T, Osorio D, Nilsson D, Berens P, Baden T: **Zebrafish Differentially Process Color across Visual Space to Match Natural Scenes**. *Current Biology* 2018, **28**(13):2018-+.
30. Branchek T: **The development of photoreceptors in the zebrafish, brachydanio rerio. II. Function**. *J Comp Neurol* 1984, **224**(1):116-122.
31. Branchek T, Bremiller R: **The development of photoreceptors in the zebrafish, Brachydanio rerio. I. Structure**. *J Comp Neurol* 1984, **224**(1):107-115.
32. Bilotta J, Saszik S: **The zebrafish as a model visual system**. *International Journal of Developmental Neuroscience* 2001, **19**(7):621-629.
33. Connaughton VP, Nelson R: **Axonal stratification patterns and glutamate-gated conductance mechanisms in zebrafish retinal bipolar cells**. *J Physiol* 2000, **524 Pt 1**:135-146.
34. Connaughton VP, Graham D, Nelson R: **Identification and morphological classification of horizontal, bipolar, and amacrine cells within the zebrafish retina**. *J Comp Neurol* 2004, **477**(4):371-385.
35. Emran F, Rihel J, Adolph AR, Wong KY, Kraves S, Dowling JE: **OFF ganglion cells cannot drive the optokinetic reflex in zebrafish**. *Proc Natl Acad Sci U S A* 2007, **104**(48):19126-19131.
36. Li YN, Tsujimura T, Kawamura S, Dowling JE: **Bipolar cell-photoreceptor connectivity in the zebrafish (Danio rerio) retina**. *J Comp Neurol* 2012, **520**(16):3786-3802.

37. Chapot C, Euler T, Schubert T: **How do horizontal cells 'talk' to cone photoreceptors? Different levels of complexity at the cone-horizontal cell synapse**. *The Journal of physiology* 2017, ***595*(16)**:5495–5506.
38. Baden T, Osorio D: **The Retinal Basis of Vertebrate Color Vision**. *Annu Rev Vis Sci* 2019, **5**:177-200.
39. Twig G, Levy H, Perlman I: **Color opponency in horizontal cells of the vertebrate retina**. *Prog Retin Eye Res* 2003, **22**(1):31-68.
40. Connaughton VP, Nelson R: **Spectral responses in zebrafish horizontal cells include a tetraphasic response and a novel UV-dominated triphasic response**. *J Neurophysiol* 2010, **104**(5):2407-2422.
41. Li YN, Matsui JI, Dowling JE: **Specificity of the horizontal cell-photoreceptor connections in the zebrafish (Danio rerio) retina**. *J Comp Neurol* 2009, **516**(5):442-453.
42. Song PI, Matsui JI, Dowling JE: **Morphological types and connectivity of horizontal cells found in the adult zebrafish (Danio rerio) retina**. *J Comp Neurol* 2008, **506**(2):328-338.
43. Torvund MM, Ma TS, Connaughton VP, Ono F, Nelson RF: **Cone signals in monostratified and bistratified amacrine cells of adult zebrafish retina**. *J Comp Neurol* 2017, **525**(7):1532-1557.
44. Jusuf PR, Harris WA: **Ptf1a is expressed transiently in all types of amacrine cells in the embryonic zebrafish retina**. *Neural Dev* 2009, **4**:34.
45. Franke K, Baden T: **General features of inhibition in the inner retina**. *J Physiol* 2017, **595**(16):5507-5515.
46. Robles E, Laurell E, Baier H: **The retinal projectome reveals brain-area-specific visual representations generated by ganglion cell diversity**. *Curr Biol* 2014, **24**(18):2085-2096.
47. Preuss SJ, Trivedi CA, vom Berg-Maurer CM, Ryu S, Bollmann JH: **Classification of object size in retinotectal microcircuits**. *Curr Biol* 2014, **24**(20):2376-2385.
48. Zhou M, Bear J, Roberts PA, Janiak FK, Semmelhack J, Yoshimatsu T, Baden T: **Zebrafish Retinal Ganglion Cells Asymmetrically Encode Spectral and Temporal Information across Visual Space**. *Curr Biol* 2020, **30**(15):2927-2942.e2927.
49. Zhang R, Wei H, Xia Y, Du J: **Development of light response and GABAergic excitation-to-inhibition switch in zebrafish retinal ganglion cells**. *Journal of Physiology-London* 2010, **588**(14):2557-2569.

50. Connaughton, P V, Nelson, F R: **Ultraviolet dominates ganglion cell light responses in larval zebrafish retinas.** *Investigative Ophthalmology & Visual Science* 2015, **56**:3251-3251.
51. Gabriel JP, Trivedi CA, Maurer CM, Ryu S, Bollmann JH: **Layer-specific targeting of direction-selective neurons in the zebrafish optic tectum**. *Neuron* 2012, **76**(6):1147-1160.
52. Nikolaou N, Lowe AS, Walker AS, Abbas F, Hunter PR, Thompson ID, Meyer MP: **Parametric functional maps of visual inputs to the tectum**. *Neuron* 2012, **76**(2):317-324.
53. Lowe A, Nikolaou N, Hunter P, Thompson I, MP M: **A systems-based dissection of retinal inputs to the zebrafish tectum reveals different rules for different functional classes during development.** *J Neurosci* 2013.
54. Semmelhack JL, Donovan JC, Thiele TR, Kuehn E, Laurell E, Baier H: **A dedicated visual pathway for prey detection in larval zebrafish**. *Elife* 2014, **3**.
55. Roeser T, Baier H: **Visuomotor behaviors in larval zebrafish after GFP-guided laser ablation of the optic tectum**. *J Neurosci* 2003, **23**(9):3726-3734.
56. Kubo F, Hablitzel B, Dal Maschio M, Driever W, Baier H, Arrenberg AB: **Functional architecture of an optic flow-responsive area that drives horizontal eye movements in zebrafish**. *Neuron* 2014, **81**(6):1344-1359.
57. Robles E, Filosa A, Baier H: **Precise lamination of retinal axons generates multiple parallel input pathways in the tectum**. *J Neurosci* 2013, **33**(11):5027-5039.
58. Niell CM, Smith SJ: **Functional imaging reveals rapid development of visual response properties in the zebrafish tectum**. *Neuron* 2005, **45**(6):941-951.
59. Hunter PR, Lowe AS, Thompson ID, Meyer MP: **Emergent properties of the optic tectum revealed by population analysis of direction and orientation selectivity**. *J Neurosci* 2013, **33**(35):13940-13945.
60. Yoshimatsu T, Schröder C, Nevala NE, Berens P, Baden T: **Fovea-like Photoreceptor Specializations Underlie Single UV Cone Driven Prey-Capture Behavior in Zebrafish**. *Neuron* 2020, **107**(2):320-337.e326.

61. Bollmann JH: **The Zebrafish Visual System: From Circuits to Behavior**. *Annu Rev Vis Sci* 2019, **5**:269-293.
62. Dunn TW, Mu Y, Narayan S, Randlett O, Naumann EA, Yang CT, Schier AF, Freeman J, Engert F, Ahrens MB: **Brain-wide mapping of neural activity controlling zebrafish exploratory locomotion**. *Elife* 2016, **5**:e12741.
63. Wang K, Hinz J, Haikala V, Reiff DF, Arrenberg AB: **Selective processing of all rotational and translational optic flow directions in the zebrafish pretectum and tectum**. *BMC Biol* 2019, **17**(1):29.
64. Antinucci P, Folgueira M, Bianco IH: **Pretectal neurons control hunting behaviour**. *Elife* 2019, **8**.
65. Wolf S, Dubreuil AM, Bertoni T, Böhm UL, Bormuth V, Candelier R, Karpenko S, Hildebrand DGC, Bianco IH, Monasson R *et al*: **Sensorimotor computation underlying phototaxis in zebrafish**. *Nat Commun* 2017, **8**(1):651.
66. Orger MB, Kampff AR, Severi KE, Bollmann JH, Engert F: **Control of visually guided behavior by distinct populations of spinal projection neurons**. *Nat Neurosci* 2008, **11**(3):327-333.
67. Neuhauss SC, Biehlmaier O, Seeliger MW, Das T, Kohler K, Harris WA, Baier H: **Genetic disorders of vision revealed by a behavioral screen of 400 essential loci in zebrafish**. *J Neurosci* 1999, **19**(19):8603-8615.
68. Orger M, Baier H: **Channeling of red and green cone inputs to the zebrafish optomotor response**. *Visual Neuroscience* 2005, **22**(3):275-281.
69. Burgess HA, Schoch H, Granato M: **Distinct retinal pathways drive spatial orientation behaviors in zebrafish navigation**. *Curr Biol* 2010, **20**(4):381-386.
70. Ahrens MB, Orger MB, Robson DN, Li JM, Keller PJ: **Whole-brain functional imaging at cellular resolution using light-sheet microscopy**. *Nat Methods* 2013, **10**(5):413-420.
71. Gahtan E, Tanger P, Baier H: **Visual prey capture in larval zebrafish is controlled by identified reticulospinal neurons downstream of the tectum**. *J Neurosci* 2005, **25**(40):9294-9303.
72. Bianco IH, Kampff AR, Engert F: **Prey capture behavior evoked by simple visual stimuli in larval zebrafish**. *Front Syst Neurosci* 2011, **5**:101.

73. Del Bene F, Wyart C, Robles E, Tran A, Looger L, Scott EK, Isacoff EY, Baier H: **Filtering of visual information in the tectum by an identified neural circuit**. *Science* 2010, **330**(6004):669-673.
74. Yin C, Li X, Du J: **Optic tectal superficial interneurons detect motion in larval zebrafish**. *Protein Cell* 2019, **10**(4):238-248.
75. Temizer I, Donovan JC, Baier H, Semmelhack JL: **A Visual Pathway for Looming-Evoked Escape in Larval Zebrafish**. *Curr Biol* 2015, **25**(14):1823-1834.
76. Dunn TW, Gebhardt C, Naumann EA, Riegler C, Ahrens MB, Engert F, Del Bene F: **Neural Circuits Underlying Visually Evoked Escapes in Larval Zebrafish**. *Neuron* 2016, **89**(3):613-628.
77. Zhang BB, Yao YY, Zhang HF, Kawakami K, Du JL: **Left Habenula Mediates Light-Preference Behavior in Zebrafish via an Asymmetrical Visual Pathway**. *Neuron* 2017, **93**(4):914-928.e914.
78. Swanson LW, Lichtman JW: **From Cajal to Connectome and Beyond**. *Annu Rev Neurosci* 2016, **39**:197-216.
79. Willis T: **Cerebri anatome: cui accessit nervorum descriptio et usus**. London: Flesher,Martyn and Allestry; 1664.
80. Cajal S: **Estructura de los centros nerviosos de las aves**. 1888, **1:1–10**.
81. Cajal R: **El nuevo concepto de la histologia de los centros nerviosos**. *Rev Cien Méd Barc* 1892, **18:361–376, 457–476, 505–520, 529–541**.
82. Kasthuri N, Hayworth KJ, Berger DR, Schalek RL, Conchello JA, Knowles-Barley S, Lee D, Vázquez-Reina A, Kaynig V, Jones TR *et al*: **Saturated Reconstruction of a Volume of Neocortex**. *Cell* 2015, **162**(3):648-661.
83. Kasthuri N, Lichtman JW: **The rise of the 'projectome'**. *Nat Methods* 2007, **4**(4):307-308.
84. Lichtman JW, Livet J, Sanes JR: **A technicolour approach to the connectome**. *Nat Rev Neurosci* 2008, **9**(6):417-422.
85. Lichtman JW, Pfister H, Shavit N: **The big data challenges of connectomics**. *Nat Neurosci* 2014, **17**(11):1448-1454.
86. Pan YA, Livet J, Sanes JR, Lichtman JW, Schier AF: **Multicolor Brainbow imaging in zebrafish**. *Cold Spring Harb Protoc* 2011, **2011**(1):pdb.prot5546.

87. Weissman TA, Sanes JR, Lichtman JW, Livet J: **Generating and imaging multicolor Brainbow mice**. *Cold Spring Harb Protoc* 2011, **2011**(7):763-769.
88. Livet J, Weissman TA, Kang H, Draft RW, Lu J, Bennis RA, Sanes JR, Lichtman JW: **Transgenic strategies for combinatorial expression of fluorescent proteins in the nervous system**. *Nature* 2007, **450**(7166):56-62.
89. Hildebrand DGC, Cicconet M, Torres RM, Choi W, Quan TM, Moon J, Wetzel AW, Scott Champion A, Graham BJ, Randlett O *et al*: **Whole-brain serial-section electron microscopy in larval zebrafish**. *Nature* 2017, **545**(7654):345-349.
90. Lakowicz JR: **Principles of Fluorescence Spectroscopy**, Third ed. edn: Springer; 2006.
91. Zheng Q, Jockusch S, Zhou Z, Blanchard SC: **The contribution of reactive oxygen species to the photobleaching of organic fluorophores**. *Photochem Photobiol* 2014, **90**(2):448-454.
92. Shimomura O, Johnson Fh, Saiga Y: **Extraction, purification and properties of aequorin, a bioluminescent protein from the luminous hydromedusan, Aequorea**. *J Cell Comp Physiol* 1962, **59**:223-239.
93. Yang F, Moss LG, Phillips GN, Jr: **The molecular structure of green fluorescent protein**. *Nature biotechnology* 1996, **14(10)**:1246–1251.
94. Tsien RY: **The green fluorescent protein**. *Annu Rev Biochem* 1998, **67**:509-544.
95. Morise H, Shimomura O, Johnson FH, Winant J: **Intermolecular energy transfer in the bioluminescent system of Aequorea**. *Biochemistry* 1974, **13**(12):2656-2662.
96. Ormö M, Cubitt AB, Kallio K, Gross LA, Tsien RY, Remington SJ: **Crystal structure of the Aequorea victoria green fluorescent protein**. *Science* 1996, **273**(5280):1392-1395.
97. Shimomura O: **Structure of the chromophore of Aequorea green fluorescent protein**. *FEBS Letters* 1979, **104**(2):220-222.
98. Heim R, Prasher DC, Tsien RY: **Wavelength mutations and posttranslational autoxidation of green fluorescent protein**. *Proc Natl Acad Sci U S A* 1994, **91**(26):12501-12504.
99. Cubitt AB, Heim R, Adams SR, Boyd AE, Gross LA, Tsien RY: **Understanding, improving and using green fluorescent proteins**. *Trends Biochem Sci* 1995, **20**(11):448-455.

100. Cody CW, Prasher DC, Westler WM, Prendergast FG, Ward WW: **Chemical structure of the hexapeptide chromophore of the Aequorea green-fluorescent protein**. *Biochemistry* 1993, **32**(5):1212-1218.
101. Chattoraj M, King BA, Bublitz GU, Boxer SG: **Ultra-fast excited state dynamics in green fluorescent protein: multiple states and proton transfer**. *Proc Natl Acad Sci U S A* 1996, **93**(16):8362-8367.
102. Yokoe H, Meyer T: **Spatial dynamics of GFP-tagged proteins investigated by local fluorescence enhancement**. *Nat Biotechnol* 1996, **14**(10):1252-1256.
103. Prasher DC, Eckenrode VK, Ward WW, Prendergast FG, Cormier MJ: **Primary structure of the Aequorea victoria green-fluorescent protein**. *Gene* 1992, **111**(2):229-233.
104. Chalfie M, Tu Y, Euskirchen G, Ward WW, Prasher DC: **Green fluorescent protein as a marker for gene expression**. *Science* 1994, **263**(5148):802-805.
105. Inouye S, Tsuji FI: **Aequorea green fluorescent protein. Expression of the gene and fluorescence characteristics of the recombinant protein**. *FEBS Lett* 1994, **341**(2-3):277-280.
106. Yasuda R, Nimchinsky EA, Scheuss V, Pologruto TA, Oertner TG, Sabatini BL, Svoboda K: **Imaging calcium concentration dynamics in small neuronal compartments**. *Sci STKE* 2004, **2004**(219):pl5.
107. Akerboom J, Chen TW, Wardill TJ, Tian L, Marvin JS, Mutlu S, Calderón NC, Esposti F, Borghuis BG, Sun XR *et al*: **Optimization of a GCaMP calcium indicator for neural activity imaging**. *J Neurosci* 2012, **32**(40):13819-13840.
108. Cobbold PH, Rink TJ: **Fluorescence and bioluminescence measurement of cytoplasmic free calcium**. *Biochem J* 1987, **248**(2):313-328.
109. Mank M, Griesbeck O: **Genetically encoded calcium indicators**. *Chem Rev* 2008, **108**(5):1550-1564.
110. Mao T, O'Connor DH, Scheuss V, Nakai J, Svoboda K: **Characterization and subcellular targeting of GCaMP-type genetically-encoded calcium indicators**. *PLoS One* 2008, **3**(3):e1796.
111. Topell S, Hennecke J, Glockshuber R: **Circularly permuted variants of the green fluorescent protein**. *FEBS Lett* 1999, **457**(2):283-289.

112. Nagai T, Ibata K, Park ES, Kubota M, Mikoshiba K, Miyawaki A: **A variant of yellow fluorescent protein with fast and efficient maturation for cell-biological applications**. *Nat Biotechnol* 2002, **20**(1):87-90.
113. Graf R, Schachman HK: **Random circular permutation of genes and expressed polypeptide chains: application of the method to the catalytic chains of aspartate transcarbamoylase**. *Proc Natl Acad Sci U S A* 1996, **93**(21):11591-11596.
114. Chen TW, Wardill TJ, Sun Y, Pulver SR, Renninger SL, Baohan A, Schreiter ER, Kerr RA, Orger MB, Jayaraman V *et al*: **Ultrasensitive fluorescent proteins for imaging neuronal activity**. *Nature* 2013, **499**(7458):295-300.
115. Göppert-Mayer M: **Über Elementarakte mit zwei Quantensprüngen**. *Annalen der Physik* 1931, **401**:273-294.
116. Zipfel W, Williams R, Webb W: **Nonlinear magic: multiphoton microscopy in the biosciences**. *Nature Biotechnology* 2003, **21**(11):1368-1376.
117. Denk W, Strickler JH, Webb WW: **Two-photon laser scanning fluorescence microscopy**. *Science* 1990, **248**(4951):73-76.
118. Helmchen F, Denk W: **Deep tissue two-photon microscopy**. *Nat Methods* 2005, **2**(12):932-940.
119. Xu C, Webb WW: **Measurement of two-photon excitation cross sections of molecular fluorophores with data from 690 to 1050 nm**. *Journal of the Optical Society of America B* 1996, **13**:481-491.
120. Theer P, Hasan MT, Denk W: **Two-photon imaging to a depth of 1000 microm in living brains by use of a Ti:Al2O3 regenerative amplifier**. *Opt Lett* 2003, **28**(12):1022-1024.
121. Galbraith JA, Terasaki M: **Controlled damage in thick specimens by multiphoton excitation**. *Mol Biol Cell* 2003, **14**(5):1808-1817.
122. Vogel A, Noack J, Hüttman G, Paltauf G: **Mechanisms of femtosecond laser nanosurgery of cells and tissues**. *Applied Physics B* 2005, **81**(8):1015-1047.
123. Vogel A, Venugopalan V: **Mechanisms of pulsed laser ablation of biological tissues**. *Chem Rev* 2003, **103**(2):577-644.
124. Tsai PS, Blinder P, Migliori BJ, Neev J, Jin Y, Squier JA, Kleinfeld D: **Plasma-mediated ablation: an optical tool for submicrometer surgery on neuronal and vascular systems**. *Current Opinion in Biotechnology* 2009, **20**(1):90-99.

125. Liu KS, Fetcho JR: **Laser ablations reveal functional relationships of segmental hindbrain neurons in zebrafish**. *Neuron* 1999, **23**(2):325-335.
126. Nava SS, An S, Hamil T: **Visual detection of UV cues by adult zebrafish (Danio rerio)**. *J Vis* 2011, **11**(6):2.
127. Oliveira J, Silveira M, Chacon D, Luchiari A: **The Zebrafish World of Colors and Shapes: Preference and Discrimination**. *Zebrafish* 2015, **12**(2):166-173.
128. Park JS, Ryu JH, Choi TI, Bae YK, Lee S, Kang HJ, Kim CH: **Innate Color Preference of Zebrafish and Its Use in Behavioral Analyses**. *Mol Cells* 2016, **39**(10):750-755.
129. Spence R, Smith C: **Innate and learned colour preference in the zebrafish, Danio rerio**. *Ethology* 2008, **114**(6):582-588.
130. Avdesh A, Martin-Iverson M, Mondal A, Chen M, Askraba S, Morgan N, Lardelli M, Groth D, Verdile G, Martins R: **Evaluation of Color Preference in Zebrafish for Learning and Memory**. *Journal of Alzheimers Disease* 2012, **28**(2):459-469.
131. Nüsslein-Volhard C, Dahm R: **Zebrafish: A Practical Approach.** Oxford, United Kingdom: Oxford University Press; 2002.
132. Müllenbroich MC, Turrini L, Silvestri L, Alterini T, Gheisari A, Tiso N, Vanzi F, Sacconi L, Pavone FS: **Bessel Beam Illumination Reduces Random and Systematic Errors in Quantitative Functional Studies Using Light-Sheet Microscopy**. *Front Cell Neurosci* 2018, **12**:315.
133. Vladimirov N, Mu Y, Kawashima T, Bennett DV, Yang CT, Looger LL, Keller PJ, Freeman J, Ahrens MB: **Light-sheet functional imaging in fictively behaving zebrafish**. *Nat Methods* 2014, **11**(9):883-884.
134. Freeman J, Vladimirov N, Kawashima T, Mu Y, Sofroniew NJ, Bennett DV, Rosen J, Yang CT, Looger LL, Ahrens MB: **Mapping brain activity at scale with cluster computing**. *Nat Methods* 2014, **11**(9):941-950.
135. Kawashima T, Zwart M, Yang C, Mensh B, Ahrens M: **The Serotonergic System Tracks the Outcomes of Actions to Mediate Short-Term Motor Learning**. *Cell* 2016, **167**(4):933-+.
136. Miri A, Daie K, Burdine RD, Aksay E, Tank DW: **Regression-based identification of behavior-encoding neurons during large-scale optical imaging of neural activity at cellular resolution**. *J Neurophysiol* 2011, **105**(2):964-980.

137. Randlett O, Wee CL, Naumann EA, Nnaemeka O, Schoppik D, Fitzgerald JE, Portugues R, Lacoste AM, Riegler C, Engert F *et al*: **Whole-brain activity mapping onto a zebrafish brain atlas**. *Nat Methods* 2015, **12**(11):1039-1046.
138. Jefferis GS, Potter CJ, Chan AM, Marin EC, Rohlfing T, Maurer CR, Luo L: **Comprehensive maps of Drosophila higher olfactory centers: spatially segregated fruit and pheromone representation**. *Cell* 2007, **128**(6):1187-1203.
139. Rohlfing T, Maurer CR: **Nonrigid image registration in shared-memory multiprocessor environments with application to brains, breasts, and bees**. *IEEE Trans Inf Technol Biomed* 2003, **7**(1):16-25.
140. Turrini L, Fornetto C, Marchetto G, Müllenbroich MC, Tiso N, Vettori A, Resta F, Masi A, Mannaioni G, Pavone FS *et al*: **Optical mapping of neuronal activity during seizures in zebrafish**. *Sci Rep* 2017, **7**(1):3025.
141. Lukyanov KA, Chudakov DM, Lukyanov S, Verkhusha VV: **Innovation: Photoactivatable fluorescent proteins**. *Nat Rev Mol Cell Biol* 2005, **6**(11):885-891.
142. Fosque BF, Sun Y, Dana H, Yang CT, Ohyama T, Tadross MR, Patel R, Zlatic M, Kim DS, Ahrens MB *et al*: **Neural circuits. Labeling of active neural circuits in vivo with designed calcium integrators**. *Science* 2015, **347**(6223):755-760.
143. Kim DH, Kim J, Marques JC, Grama A, Hildebrand DGC, Gu W, Li JM, Robson DN: **Pan-neuronal calcium imaging with cellular resolution in freely swimming zebrafish**. *Nat Methods* 2017, **14**(11):1107-1114.
144. Cong L, Wang Z, Chai Y, Hang W, Shang C, Yang W, Bai L, Du J, Wang K, Wen Q: **Rapid whole brain imaging of neural activity in freely behaving larval zebrafish (***Elife* 2017, **6**.
145. Berlin S, Carroll EC, Newman ZL, Okada HO, Quinn CM, Kallman B, Rockwell NC, Martin SS, Lagarias JC, Isacoff EY: **Photoactivatable genetically encoded calcium indicators for targeted neuronal imaging**. *Nat Methods* 2015, **12**(9):852-858.
146. Fenno L, Yizhar O, Deisseroth K: **The development and application of optogenetics**. *Annu Rev Neurosci* 2011, **34**:389-412.
147. Bernhardt RR, Chitnis AB, Lindamer L, Kuwada JY: **Identification of spinal neurons in the embryonic and larval zebrafish**. *J Comp Neurol* 1990, **302**(3):603-616.

148. Euler T, Franke K, Baden T: **Studying a Light Sensor with Light: Multiphoton Imaging in the Retina.** In: *Hartveit E (eds) Multiphoton Microscopy.* vol. Neuromethods, vol 148: Humana, New York, NY; 2019.
149. Franke K, Berens P, Schubert T, Bethge M, Euler T, Baden T: **Inhibition decorrelates visual feature representations in the inner retina**. *Nature* 2017, **542**(7642):439-444.
150. Chklovskii DB, Koulakov AA: **MAPS IN THE BRAIN: What Can We Learn from Them?** *Annual Review of Neuroscience* 2004, **27**:369-392.
151. Bianco IH, Engert F: **Visuomotor transformations underlying hunting behavior in zebrafish**. *Curr Biol* 2015, **25**(7):831-846.
152. Wang K, Hinz J, Zhang Y, Thiele TR, Arrenberg AB: **Parallel Channels for Motion Feature Extraction in the Pretectum and Tectum of Larval Zebrafish**. *Cell Rep* 2020, **30**(2):442-453.e446.
153. Guggiana Nilo DA, Riegler C, Hübener M, Engert F: **Colors everywhere: enhanced chromatic processing across the first visual synapse in the zebrafish central brain**. *bioRxiv* 2020.
154. Robinson J, Schmitt E, Dowling J: **Temporal And Spatial Patterns Of Opsin Gene-Expression In Zebrafish (Danio-Rerio)**. *Visual Neuroscience* 1995, **12**(5):895-906.
155. Mano H, Kojima D, Fukada Y: **Exo-rhodopsin: a novel rhodopsin expressed in the zebrafish pineal gland**. *Molecular Brain Research* 1999, **73**(1-2):110-118.
156. Wada S, Shen B, Kawano-Yamashita E, Nagata T, Hibi M, Tamotsu S, Koyanagi M, Terakita A: **Color opponency with a single kind of bistable opsin in the zebrafish pineal organ**. *Proceedings of the National Academy of Sciences of the United States of America* 2018, **115**(44):11310-11315.
157. Sapede D, Chaigne C, Blader P, Cau E: **Functional heterogeneity in the pineal projection neurons of zebrafish**. *Molecular and Cellular Neuroscience* 2020, **103**.
158. Morita Y: **Lead pattern of the pineal neuron of the rainbow trout (Salmo irideus) by illumination of the diencephalon.** In., vol. 289(3),155–167: Pflugers Arch. Gesamte Physiol. Menschen Tiere; 1966.
159. Meissl H, Ueck M: **Extraocular photoreception of the pineal gland of the aquatic turtle Pseudemys scripta elegans.** In., vol. 140,173–179: Journal of Comparative Phisiology A; 1980.

160. Falcón J, Meissl H: **The photosensory function of the pineal organ of the pike (Esox lucius L.) correlation between structure and function.** In., vol. 144,127–137: Journal of Comparative Physiology A; 1981.
161. Sporns O, Tononi G, Kötter R: **The human connectome: A structural description of the human brain**. *PLoS Comput Biol* 2005, **1**(4):e42.
162. Akerboom J, Carreras Calderón N, Tian L, Wabnig S, Prigge M, Tolö J, Gordus A, Orger MB, Severi KE, Macklin JJ *et al*: **Genetically encoded calcium indicators for multi-color neural activity imaging and combination with optogenetics**. *Front Mol Neurosci* 2013, **6**:2.

7. APPENDIX

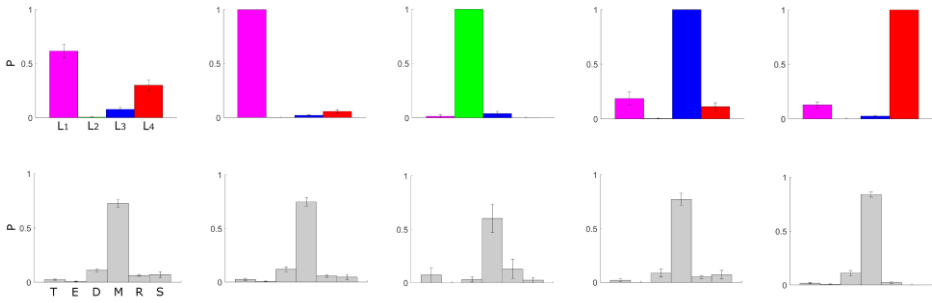

Figure A1. Quantification of spectral and anatomical identities in 5 dpf larvae

From left to right: same data shown in bar form in Figure 37C and Figure 39C, F, I, L, respectively. Here we additionally report error bars (stderr, N = 7 larvae).

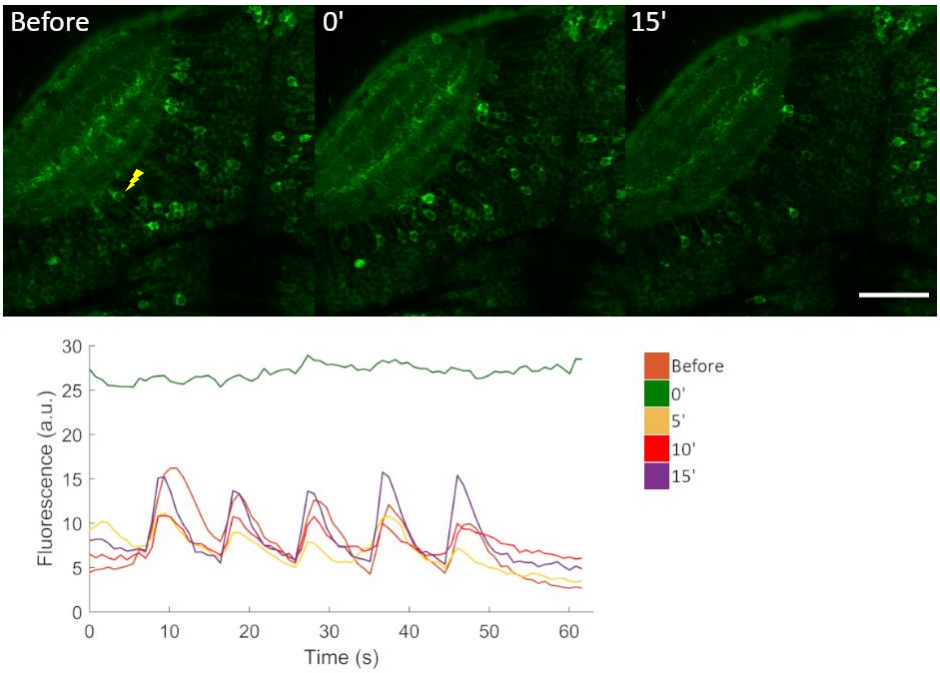

Figure A2. Tectal neuron temporary inactivation.

The panel shows another example of low-power irradiation on the cell indicated by the yellow lightning (top left panel). The three panels show the FOV before, just after and 15 minutes after the irradiation. the bottom panel shows the fluorescence time traces measured in the targeted neuron during visual stimulation (see methods) at different times before and after irradiation (see legend). Scale bar: 50 µm.

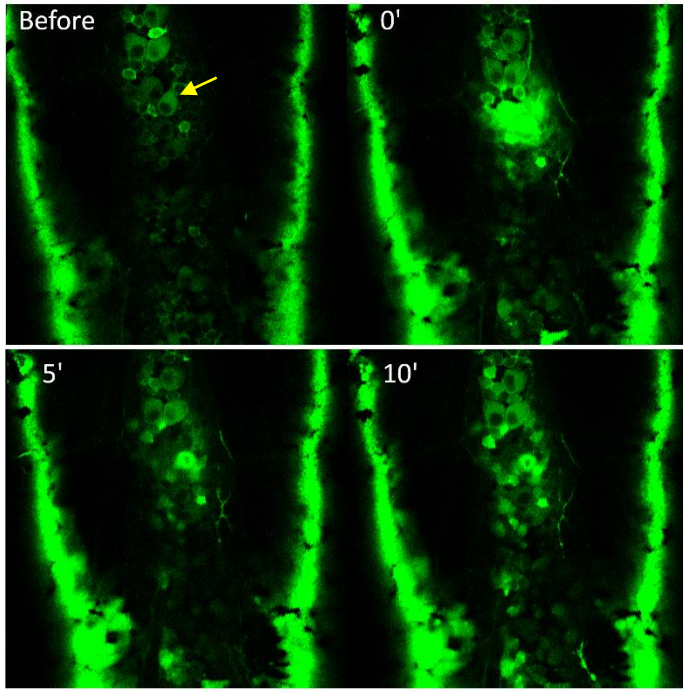

Figure A3. Laser-induced damage in spinal cord neurons.

Effect of high-power irradiation in targeted Rohon-Beard spinal cord neuron and monitoring of the damage at different time intervals. Neuron selected for irradiation is highlighted by the yellow arrow in the top left panel. After the irradiation (0') it is possible to observe a massive activation of the selected cell involving also the neighboring area, followed by an evident damage (5', 10' panels) restricted to the selected cell. The figure shows a clear example of the destructive effect induced by high-power laser parameters.

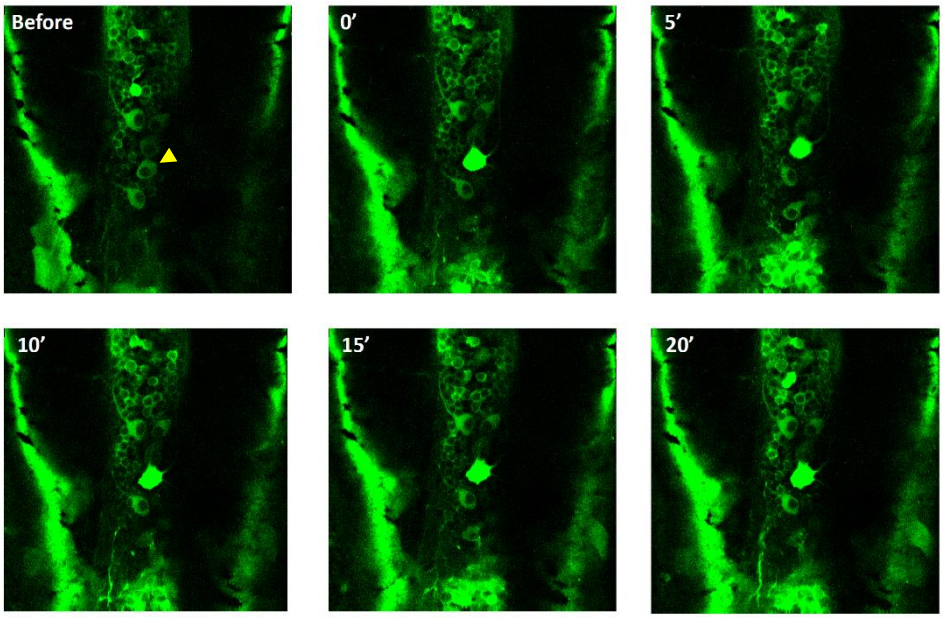

Figure A4. Irreversible perturbation in spinal cord neuron.

High-power irradiation with a more restricted line scan induces an irreversible activation of the target cell lasting in time (panels 0', 5', 10', 15', 20') allowing to resolve its projections. We observed a high increase of fluorescence in the spinal cold neuron selected for irradiation (indicated by the yellow arrowhead) which never returns to the initial intensity levels.

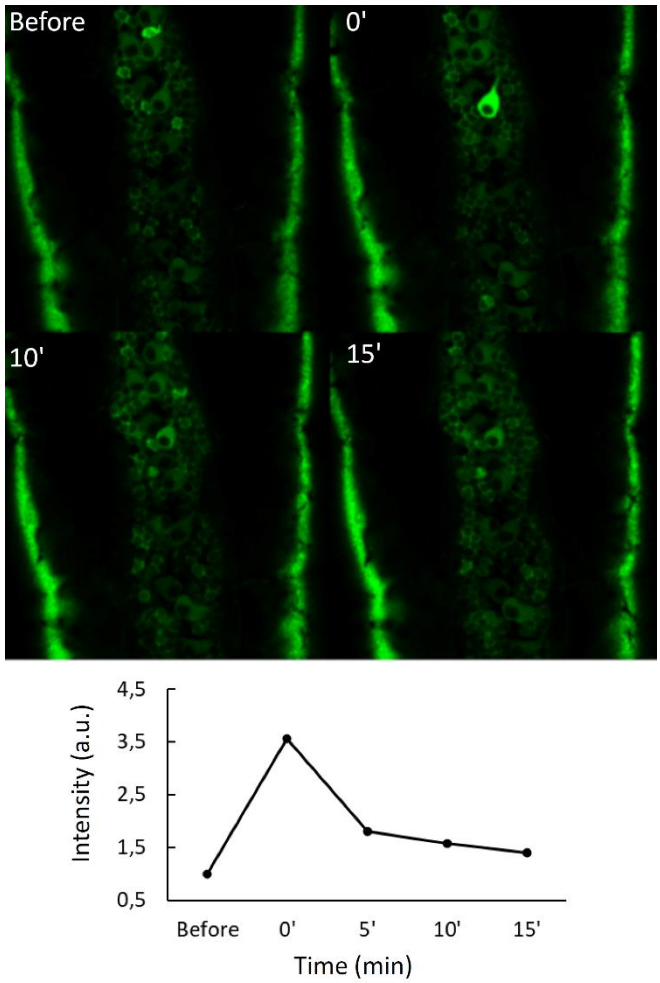

Figure A5. Temporary perturbation in a spinal cord neuron.

Effect of low-power irradiation in Rohon-Beard spinal cord neuron. As for the tectal neuron, also in this case we observe an increase of fluorescence restricted to the selected cell just after the irradiation (0') and a recovery of the initial baseline fluorescence levels already few minutes later (10' and 15' panels). The bottom graph shows the normalized average intensity measured in the targeted neuron at different time intervals.

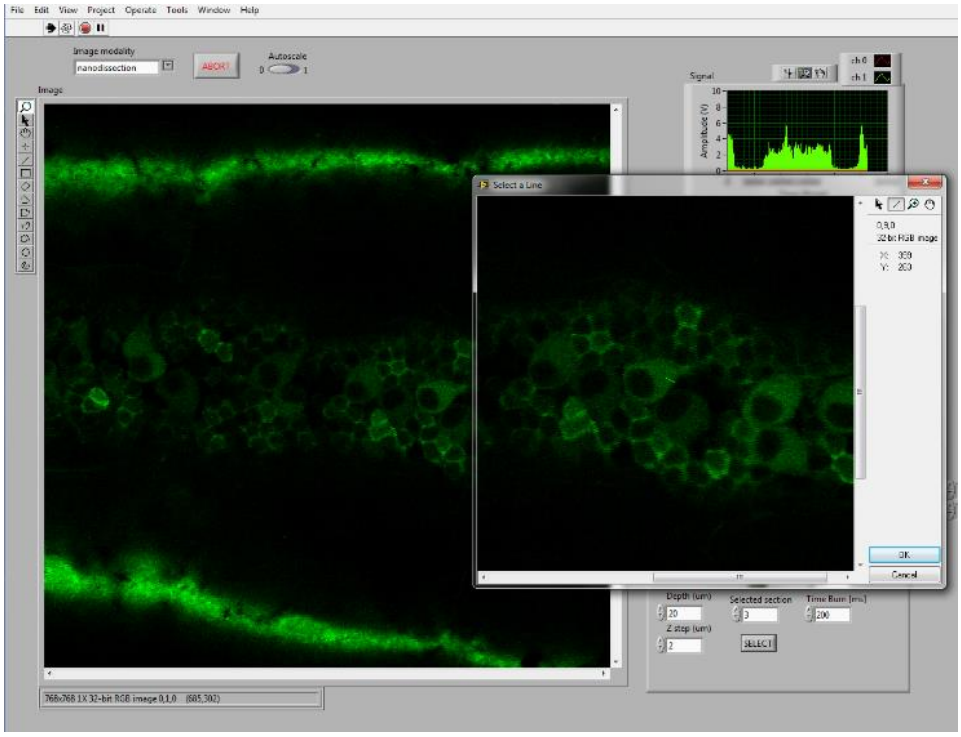

Figure A6. Software control panel for irradiation procedure.

Custom-written Labview program used for performing the line scan on the neuron cell membrane targeted for irradiation. The line used for irradiation is shown in green on the cell magnified in the right panel.

```
% Setup folders for reading data and analysis

mainfolder=pwd;
strfolders=dir;
folders=extractfield(strfolders,'name');
folderanalysis=strcat(mainfolder,'\analisi');
outdir=folderanalysis;  %% specify output directory
mkdir(outdir);
paginate=strcat(folderanalysis,'\paginate');
mkdir(paginate);
nf=length(folders)-2;

% Generates regressors
fr=transpose(1:418);
tauon=3.5;
tauoff=5;
x_impulse=0:100;
irf=-exp(-x_impulse/tauon)+exp(-x_impulse/tauoff);
figure
plot(x_impulse,irf)

pulseu=zeros(418,1);
pulsev=zeros(418,1);
pulseb=zeros(418,1);
pulser=zeros(418,1);

t0u=[50 170 290]
t0v=[80 200 320]
t0b=[110 230 350]
t0r=[140 260 380]

pulseu(t0u)=1;
pulsev(t0v)=1;
pulseb(t0b)=1;
pulser(t0r)=1;

CIRFu=conv(pulseu,irf);
CIRFv=conv(pulsev,irf);
CIRFb=conv(pulseb,irf);
CIRFr=conv(pulser,irf);

t0up=t0u-10;
t0vp=t0v-10;
t0bp=t0b-10;
t0rp=t0r-10;

G(:,1)=CIRFu;
G(:,2)=CIRFv;
G(:,3)=CIRFb;
G(:,4)=CIRFr;
G(419:end,:)=[];
G(1:10,:)=[];
z=1;
```

```
G=Gram_Schmidt_Process(G); %orthonormalization of regressors


%%
%Opens each folder and reads the image stack to generate MIP and segmentation

for k=1:nf
    folder=char(strcat(mainfolder,'\',folders(k+2)))
    cd(folder);
    strfiles=dir(folder);
nomifiles=extractfield(strfiles,'name');
fr=transpose(1:418);

for i=3:420
    A=imread(nomifiles{i});
    B(:,:,i-2)=A(:,:);
end

% removes frames with light flashes, identifying them based on background
% increase
TL=B(1:10,1:10,:);
TR=B(791:800,1:10,:);
BL=B(1:10,1015:1024,:);
BR=B(791:800,1015:1024,:);

TL=mean(TL(:));
TR=mean(TR(:));
BL=mean(BL(:));
BR=mean(BR(:));
COR=(TL+TR+BL+BR)/4;
Discarded=zeros(1,30);
d=1;

for i=2:418
    TL=B(1:10,1:10,i);
    TR=B(791:800,1:10,i);
    BL=B(1:10,1015:1024,i);
    BR=B(791:800,1015:1024,i);
    TL=mean(TL(:));
    TR=mean(TR(:));
    BL=mean(BL(:));
    BR=mean(BR(:));
    CORi=max([TL TR BL BR]);

    if CORi>2*COR
        B(:,:,i)=B(:,:,i-1);
        Discarded(d)=i;
        d=d+1;
    end
end
xlswrite(strcat(outdir,'\','Frame_scartati_',char(folders(k+2)),'.xls'),Discarded);
MIP=max(B,[],3);

% segmentation parameters
```

```
br_threshold=200;
cont_threshold=30;
cell_rad=2;


%%  set filters and matrices for detecting cells; (Modified from Kawashima et al.↙
2014)

num_images = 1;
dim=[800 1024 1];
f=[800 1024];

ave_rad=round(cell_rad/2)+1;
[avedisk,  ave_se, r1, c1, maskinds]=make_recog_disk(ave_rad,dim);
[maxdisk,  max_se, r2, c2, maxinds]=make_recog_disk(round(cell_rad*1.5),dim);
onedisk=makeDisk(ave_rad,ave_rad*2+1);
one_se=strel(onedisk);

r=cell_rad*2;
dimp=[dim(1)+r*2 dim(2)+r*2];
oop=zeros(dimp);
oop(r+1:end-r,r+1:end-r)=1;
one_inds=find(oop);

[mdisk,  ~, ~, ~, rankinds]=make_recog_disk(r,dimp);
rank_ones=double(maskones2D_mex(int32([dim(1) dim(2)]),int32(mdisk),int32(size↙
(mdisk))))';

%%  detect cells

cell_info=struct;
cell_color=zeros([dim(1) dim(2)*2+1 dim(3) 3],'uint8');
cellnum=0;
allmask=zeros(dim(1),dim(2));
imlen=dim(1)*dim(2);



    im=MIP;
    allmask(:)=0;
    contimage = local_contrast_mex(single(im),int32(32),single(cont_threshold));
    contimage = imdilate(imerode(contimage,one_se),one_se);
    contimage = contimage.*uint8((im>br_threshold));

    candidates=find(contimage);

    if ~isempty(candidates)
        %% recognizing cells in the first round

        imrank = calc_local_rank(im,rank_ones,cell_rad*2,oop,one_inds,rankinds,↙
candidates);
        aveimg = double(local_average_mex(single(imrank),int32(c1),int32(r1),int32↙
(candidates)));
        maximg = double(local_max_mex(single(aveimg),int32(c2),int32(r2),int32↙
```

```
(candidates)));

        inds=find(maximg(candidates)>0 & aveimg(candidates) >0.4);
        mask2=zeros(dim(1),dim(2));

        for i=1:length(inds)
            cinds=candidates(inds(i))+maskinds;
            cinds(cinds > imlen | cinds<1)=[];
            mask2(cinds)=1;
        end

        allmask=mask2;

        %% recognizing cells in the second round

        mask3=ones(size(im),'uint8')-imdilate(uint8(allmask),max_se);
        mask3 = imdilate(imerode(mask3,one_se),one_se);
        candidates2=candidates(mask3(candidates)>0);

        imrank2 = calc_local_rank(im,rank_ones,cell_rad*2,oop,one_inds,rankinds,↙
candidates2);
        aveimg2 = double(local_average_mex(single(imrank2),int32(c1),int32(r1),int
(candidates2)));
        maximg2 = double(local_max_mex(single(aveimg2),int32(c1),int32(r1),int32↙
(candidates2)));

        inds=find(maximg2(candidates2)>0 & aveimg2(candidates2) >0.4);
        mask2=zeros(dim(1),dim(2));

        for i=1:length(inds)
            cinds=candidates2(inds(i))+maskinds;
            cinds(cinds > imlen | cinds<1)=[];
            mask2(cinds)=1;
        end

        %generates kernel for deconvolution, identification of cell centers
        %and numbering confluent ROIs as separate cells
        allmask=allmask+mask2;
        cellkernel=[0 0 1 0 0;0 1 1 1 0;1 1 1 1 1;0 1 1 1 0;0 0 1 0 0];
        FVCell=deconvlucy(allmask,cellkernel);
        FVCell=ceil(FVCell.*(FVCell>0.8));

        %% create each cell ROIs
        [celllabel, totcell]=bwlabel(FVCell);
        celllabel=conv2(celllabel,cellkernel);
        celllabel=celllabel(3:802,3:1026);
               if totcell>0

        end
    else

        totcell=0;
        celllabel=zeros(size(im));
    end
```

```
    cell_color(:,:,z,:)=reshape(make2DMask(im,celllabel,candidates),[dim(1) dim
*2+1 1 3]);
    cellnum=cellnum+totcell;
    disp(num2str(z));

%% saves segmentation data
write_colortiff_mex(fullfile(outdir,strcat('cellmask_',char(folders(k+2)),'.tif'
cell_color, int32(size(cell_color)));
save(fullfile(outdir,strcat('cell_info_',char(folders(k+2)),'.mat')),'cell_info'
imwrite(MIP,strcat(outdir,'\MIP_',char(folders(k+2)),'.tif'));

%setup variables for linear regression
cellTuv=zeros([800 1024]);
cellTv=zeros([800 1024]);
cellTb=zeros([800 1024]);
cellTr=zeros([800 1024]);
celllaguv=zeros([800 1024]);
celllagv=zeros([800 1024]);
celllagb=zeros([800 1024]);
celllagr=zeros([800 1024]);

%skips analysis if no cells are found in this plane
if totcell==0
    continue
end

totcell

%extracts DF/F for each cell
for cn=1:totcell
    [x,y]=ind2sub(f,find(celllabel==cn));
    SInt=double(0);
    for coordpair=1:length(x)
        SInt=double(double(SInt)+double(B(x(coordpair),y(coordpair),:)));
    end
  trt(:,cn)=squeeze(SInt);
  if cn==1
      tr=double(trt(:,cn));
    else
  tr=[tr double(trt(:,cn))];
  end
        DF(:,cn)=msbackadj(fr,trt(:,cn),'WindowSize',50,'StepSize',↙
2,'SmoothMethod','lowess','QuantileValue',0.5);
        F0(:,cn)=trt(:,cn)-DF(:,cn);
        MF0=min(F0(:,cn));
        if MF0>15
          DF_F_temp=DF(:,cn)./F0(:,cn);
        else DF_F_temp(fr)=0;
        end

        DF_F_temp=smooth(DF_F_temp);
        DF_F_temp(1:10)=[];
        DF_F(:,cn)=DF_F_temp;
```

```
if (max(DF_F(:,cn))~=0)

 [cr1,l1]=xcorr(G(:,1),DF_F(:,cn),3);
 cr1=cr1(1:4);
 l1=l1(1:4);
 [cr2,l2]=xcorr(G(:,2),DF_F(:,cn),3);
 cr2=cr2(1:4);
 l2=l2(1:4);
 [cr3,l3]=xcorr(G(:,3),DF_F(:,cn),3);
 cr3=cr3(1:4);
 l3=l3(1:4);
 [cr4,l4]=xcorr(G(:,4),DF_F(:,cn),3);
 cr4=cr4(1:4);
 l4=l4(1:4);

 cc(cn,1)=max(cr1);
 cc(cn,2)=max(cr2);
 cc(cn,3)=max(cr3);
 cc(cn,4)=max(cr4);
 lag(cn,1)=l1(find(cr1==max(cr1)));
 lag(cn,2)=l2(find(cr2==max(cr2)));
 lag(cn,3)=l3(find(cr3==max(cr3)));
 lag(cn,4)=l4(find(cr4==max(cr4)));

 calcu1=G(:,1)*transpose(cc(cn,1));
 calcu2=G(:,2)*transpose(cc(cn,2));
 calcu3=G(:,3)*transpose(cc(cn,3));
 calcu4=G(:,4)*transpose(cc(cn,4));

 minlag=-min(lag(cn,:))+1;
 if minlag<1
     minlag=1;
 end
 t0uf=t0up-(minlag-1);
 t0uf(find(t0uf<=0))=[];
 t0vf=t0vp-(minlag-1);
 t0bf=t0bp-(minlag-1);
 t0rf=t0rp-(minlag-1);

 pu=zeros(length(DF_F(:,cn)),1);
 pv=pu;
 pb=pu;
 pr=pu;
 pu(t0uf)=1;
 pv(t0vf)=1;
 pb(t0bf)=1;
 pr(t0rf)=1;

 calcu1=calcu1(minlag+lag(cn,1):length(calcu1));
 calcu2=calcu2(minlag+lag(cn,2):length(calcu2));
 calcu3=calcu3(minlag+lag(cn,3):length(calcu3));
```

```
          calcu4=calcu4(minlag+lag(cn,4):length(calcu4));
          DF_F_sh=DF_F(minlag:length(DF_F(:,cn)),cn);

          minlength=min([length(calcu1) length(calcu2) length(calcu3) length(calcu
length(DF_F_sh)]);
          fr_sh=transpose(1:minlength);
          calcu1_sh=calcu1(1:minlength);
          calcu2_sh=calcu2(1:minlength);
          calcu3_sh=calcu3(1:minlength);
          calcu4_sh=calcu4(1:minlength);
          DF_F_sh=DF_F_sh(1:minlength);
          pu=pu(1:minlength);
          pv=pv(1:minlength);
          pb=pb(1:minlength);
          pr=pr(1:minlength);
          pc{cn}=[pu pv pb pr];

          calcu_all=calcu1_sh+calcu2_sh+calcu3_sh+calcu4_sh;

          % calculation of residuals between fitted and measured data
          e=transpose(DF_F_sh-calcu_all);

          DF_F_shplot{cn}=DF_F_sh;
          calcu_plot{cn}=calcu_all;

         % calculation of T values (cn is the cell number, tghe second index
         % is 1=uv, 2=violet, 3=blul, 4=red)
          Tv(cn,1)=cc(cn,1)/sqrt((e*transpose(e)/length(e)));
          Tv(cn,2)=cc(cn,2)/sqrt((e*transpose(e)/length(e)));
          Tv(cn,3)=cc(cn,3)/sqrt((e*transpose(e)/length(e)));
          Tv(cn,4)=cc(cn,4)/sqrt((e*transpose(e)/length(e)));

         else
          Tv(cn,1)=0;
          Tv(cn,2)=0;
          Tv(cn,3)=0;
          Tv(cn,4)=0;
          lag(cn,1)=NaN;
          lag(cn,2)=NaN;
          lag(cn,3)=NaN;
          lag(cn,4)=NaN;
         end
  end

xlswrite(strcat(outdir,'\','Matrice_Tv_',char(folders(k+2)),'.xls'),Tv);
xlswrite(strcat(outdir,'\','Matrice_lag_',char(folders(k+2)),'.xls'),lag);
xlswrite(strcat(outdir,'\','Matrice_DF_F_',char(folders(k+2)),'.xls'),DF_F);

cd(outdir);
dlmwrite(strcat(char(folders(k+2)),'cellule.txt'),celllabel);
save(strcat(char(folders(k+2))));


clear DF_F b T cellTuv cellTv cellTb cellTr
```

```
clear trt DF F0 DF_F cc lag pc DF_F_shplot calcu_plot Tv cellTuv cellTv cellTb↙
cellTr celllaguv celllagv celllagb celllagr PR Mcsort
close all
end
```

Matlab script for automatic neuron segmentation and regression analysis.

8. ACKNOWLEDGEMENTS

Primo fra tutti vorrei ringraziare Francesco Vanzi, per avermi trasmesso in questi anni la passione, l'entusiasmo e la curiosità nel fare ricerca. Grazie per avermi dato fiducia, per gli innumerevoli insegnamenti e consigli che mi hanno permesso di crescere da un punto di vista scientifico e professionale; e grazie per avermi fatto scoprire e appassionare al fantastico mondo di zebrafish e delle neuroscienze.

Grazie a Francesco Pavone per avermi dato questa opportunità.

Grazie alla Cate, la mia fedelissima compagna in questi anni di dottorato, per le risate, gli sfoghi, gli ape e le lunghe chiacchierate davanti a un Gin tonic e un Moscow mule. Ape con Cate, un appuntamento fisso.

Grazie a Sara, Leo, Fede, Ire, Cecca e Agne per essere stati come una seconda famiglia e per aver tentato, con scarso successo, di insegnarmi a parlare toscano. Ma soprattutto grazie per le settimane trascorse a fissare uscite per poi rimandarle all'ultimo momento. Un ringraziamento particolare va a Sara per la sua immensa disponibilità e per tutti i passaggi in macchina e in motorino che prima o poi ricambierò.

Grazie a Claudia e Maria, "le ciose", per essere state sempre presenti nonostante la lontananza e per le lunghe chiacchierate di aggiornamento davanti a un caffè tra parole in dialetto, finto milanese e c aspirate male.

Grazie a Santina per essere stata per me come una sorella. Grazie per i consigli mai banali, per aver condiviso con me gioie e pianti, e grazie per avermi viziata con un sacco di ricette free from lactose.

Grazie a Angelo, il mio fratellone, per aver creduto in me e avermi messo sempre al primo posto. Grazie per essere stato sempre al mio fianco e per non avermi mai fatto sentire sola. Grazie per questo legame bellissimo che ci tiene uniti e vicini nonostante la distanza.

Un ringraziamento speciale va alla mia mamma, il mio punto di riferimento, per avermi sempre sostenuta e aver supportato ogni mia scelta. Grazie per tutti i sacrifici di questi anni perchè se sono arrivata fino a qui lo devo esclusivamente a lei. Grazie per essermi stata sempre accanto e per

avermi insegnato che con forza e sorriso si superano anche i momenti più difficili.

Grazie poi alla mia nonna, che nonostante ormai non mi riconosca più, sono sicura sarà orgogliosa del traguardo che la sua nipotina sta per raggiungere.